

Institut für Chemie – Arbeitsgruppe Saalfrank

**Quantum Mechanical Study of Molecular Switches:
Electronic Structure, Kinetics and Dynamical Aspects**

Dissertation

zur Erlangung des akademischen Grades

“doctor rerum naturalium”

(Dr. rer. nat.)

in der Wissenschaftsdisziplin Theoretische Chemie

eingereicht an der

Mathematisch-Naturwissenschaftlichen Fakultät

der Universität Potsdam



vorgelegt von

Jadranka Dokić

aus Pančevo, Serbien

Potsdam, 2009

This work is licensed under a Creative Commons License:
Attribution - Noncommercial - Share Alike 3.0 Germany
To view a copy of this license visit
<http://creativecommons.org/licenses/by-nc-sa/3.0/de/deed.en>

1. Gutachter: Prof. Dr. P. Saalfrank
2. Gutachter: Prof. Dr. B. Hartke
3. Gutachter: Prof. Dr. G. Stock

Tag der Disputation: 29. Januar 2010

Published online at the
Institutional Repository of the University of Potsdam:
URL <http://opus.kobv.de/ubp/volltexte/2010/4179/>
URN <urn:nbn:de:kobv:517-opus-41796>
<http://nbn-resolving.org/urn:nbn:de:kobv:517-opus-41796>

Publications

1. F. Leyssner, S. Hagen, L. Óvári, J. Dokić, P. Saalfrank, M.V. Peters, S. Hecht, M. Wolf, T. Klamroth, P. Tegeder, *Photoisomerization Ability of Molecular Switches Adsorbed on Au(111): Comparison Between an Azobenzene and Stilbene Derivative*, J. Phys. Chem. C **114**, 1231-1239 (2010)
2. C. Nacci, S. Fölsch, K. Zenichowski, J. Dokić, T. Klamroth, P. Saalfrank, *Current versus Temperature-Induced Switching in a Single-Molecule Tunnel Junction: 1,5-cyclooctadiene on Si(001)*, Nano Lett. **9**, 2996-3000 (2009)
3. J. Dokić, M. Gothe, J. Wirth, M. V. Peters, J. Schwarz, S. Hecht, P. Saalfrank, *Quantum Chemical Investigations of Thermal Cis-to-Trans Isomerization of Azobenzene Derivatives: Substituent Effects, Solvent Effects, and Comparison to Experimental Data*, J. Phys. Chem. A **113**, 6763-6773 (2009)
4. N. Henningsen, K. J. Franke, I. F. Torrente, G. Schulze, B. Priewisch, K. Rück-Braun, J. Dokić, T. Klamroth, P. Saalfrank, J. I. Pascual, *Inducing the Rotation of a Single Phenyl Ring with Tunneling Electrons*, J. Phys. Chem. C **111**, 14843-14848 (2007).
5. G. Füchsel, T. Klamroth, J. Dokić, P. Saalfrank, *On the Electronic Structure of Neutral and Ionic Azobenzenes and Their Possible Role as Surface Mounted Molecular Switches*, J. Phys. Chem. B **110**, 16337-16345 (2006).

Abstract

Molecular photoswitches are attracting much attention lately mostly because of their possible applications in nano technology, and their role in biology.

One of the widely studied representatives of photochromic molecules is azobenzene (AB). With light, by a static electric field, or with tunneling electrons this specie can be “switched” from the flat and energetically more stable *trans* form, into the compact *cis* form. The back reaction can be induced optically or thermally. Quantum chemical calculations, mostly based on density functional theory, on the AB molecule, AB derivatives and related systems are presented. All the calculations were done for isolated species, however, with implications for latest experimental results aiming at the switching of surface mounted ABs. In some of these experiments, it is assumed that the switching process is substrate mediated, by attaching an electron or a hole to the adsorbate forming short-lived anion or cation resonances. Therefore, we calculated also cationic and anionic ABs in this work. An influence of external electric fields on the potential energy surfaces, was also studied.

Further, by the type, number and positioning of various substituent groups, systematic changes on activation energies and rates for the thermal *cis-to-trans* isomerization can be enforced. The nature of the transition state for ground state isomerization was investigated. Applying Eyring’s transition state theory, trends in activation energies and rates were predicted and are, where a comparison was possible, in good agreement with experimental data. Further, thermal isomerization was studied in solution, for which a polarizable continuum model was employed. The influence of substitution and an environment leaves its traces on structural properties of molecules and quantitative appearance of calculated UV/Vis spectra, as well.

Finally, an explicit treatment of a solid substrate was demonstrated for the conformational switching, by scanning tunneling microscope, of a 1,5-cyclooctadiene (COD) molecule at a Si(001) surface, treated by a cluster model. At first, we studied energetics and potential energy surfaces along relevant switching coordinates by quantum chemical calculations, followed by the switching dynamics using wave packet methods. We show that, in spite the simplicity of the model, our calculations support the switching of adsorbed COD, by inelastic electron tunneling at low temperatures.

Contents

1	Introduction	1
1.1	Molecular Switches at Surfaces	1
1.2	Outline of this Work	5
2	Theoretical Concepts	7
2.1	Quantum Chemistry	7
2.1.1	Born-Oppenheimer Approximation	7
2.1.2	Hartree-Fock Theory	9
2.1.3	Basis Sets	12
2.1.4	Density Functional Theory	13
2.1.5	Polarizable Continuum Model	18
2.1.6	Transition State Theory	22
2.2	Time-dependent Schrödinger Equation	26
2.2.1	Propagation Methods	26
2.2.2	The Gadzuk Jumping Wave Packet Scheme	28
3	Azobenzenes	31
3.1	General Properties	31
3.2	Method Testing	34
3.2.1	Structures	34

3.2.2	Excitation Energies	35
3.3	Ground State Potential Energy Surfaces	36
3.4	Anionic and Cationic Azobenzenes	38
3.4.1	Experimental Observations	38
3.4.2	Anionic Species	39
3.4.3	Cationic Species	43
4	Azobenzenes in External Electric Fields	47
4.1	Experimental Observations	47
4.2	Field Effects on TBA	48
4.3	Field Effects on DMC	52
5	Substitution Effects: Azobenzenes and Related Compounds	57
5.1	Experimental Observations	57
5.2	Computational Analysis	58
5.3	Thermal Ground State Isomerization	61
5.3.1	Electronically "Inactive" Substituents	61
5.3.2	Substitution with Electronically "Active" Groups	62
5.3.3	Isomerization of TBA-like Species	75
5.4	UV/Vis Absorption Spectra	78
5.4.1	Influence of Donors and Acceptors	78
5.4.2	Influence of Solvent	80
5.5	Bisazobenzenes	83
5.5.1	General	83
5.5.2	UV/Vis Spectra and Photoreactivity of TT-BABs	84
5.5.3	Thermal Ground State Isomerization	87
5.6	Isomerization of Imines	91

5.6.1	N-benzylideneaniline	91
5.6.2	Thermal Isomerization of Imines	92
5.7	Summary	94
6	1,5-Cyclooctadiene@Si(001)	95
6.1	General and Experimental Findings	95
6.2	Quantum Chemical Calculations	98
6.2.1	The Free COD Molecule	98
6.2.2	Adsorption of COD on Si Dimer(s)	100
6.2.3	Two- and One-Dimensional Potential Energy Surfaces	102
6.2.4	Thermal Isomerization of COD@Si(001)	104
6.2.5	New Coordinates	105
6.2.6	Anionic and Cationic Surfaces	105
6.3	Switching Dynamics	108
6.3.1	Switching Hamiltonians for 2D and 1D Models	108
6.3.2	Vibrational Wave Functions	110
6.3.3	Wave Packet Propagation: 1D Case	111
6.3.4	Wave Packet Propagation: 2D Case	115
6.4	Summary	116
7	Conclusion and Outlook	119
	Appendices	131
A	DFT Functional Test	133
B	Transition Dipole Moments and Absorption Spectra	139
C	Thermal M-TBA Isomerization	143

D COD Geometries	147
E Normal Mode Analysis for COD@Si(001)	151
F Hamiltonian Derivation for COD@Si(001)	153
G Fourier Grid Hamiltonian	155

Abbreviations

AB	azobenzene
AO	atomic orbitals
BOA	Born-Oppenheimer approximation
CI	conical intersection
CMA	3,5'-dicarboxyazobenzene
CGTOs	contracted Gaussian type orbitals
1D	one-dimensional
2D	two-dimensional
DBDCA	3,5-di- <i>tert</i> -butyl-3',5'-dicarboxyl-azobenzene
diM-TBA	4,4'-dimethoxy-3,3',5,5'-tetra- <i>tert</i> -butyl-azobenzene
DMC	di-meta-cyanoazobenzene (3,3'-dicyanoazobenzene)
DO3	disperse orange 3
e ⁻	electron
EA	electron affinity
E _F	Fermi level
fs	femtosecond
FT	Fourier transformation
GS	ground state
GTO	Gaussian type orbitals
h ⁺	hole
HF	Hartree-Fock
HOMO	highest occupied molecular orbital
ICS	image charge stabilization
IET	inelastic electron tunneling
IP	ionization potential
LCAO	linear combination of atomic orbitals
LUMO	lowest unoccupied molecular orbital
M-TBA	4-methoxy-3,3',5,5'-tetra- <i>tert</i> -butyl-azobenzene
NBA	N-benzylideneaniline
PGTO	primitive Gaussian type orbitals
PCM	polarizable continuum model
PCMA	<i>para</i> -CMA (4,4'-dicarboxyazobenzene)
PES	potential energy surface
2PPE	two-photon photoemission spectroscopy
ps	picosecond

RC	reaction coordinate
SCF	self consisted field
SD	Slater determinant
SP	single point
STO	Slater type orbitals
STM	Scanning Tunneling Microscopy
(TD)-DFT	(time-dependent)-density functional theory
TDSE	time-dependent Schrödinger equation
TISE	time-independent Schrödinger equation
TBA	3,3',5,5'-tetra- <i>tert</i> -butyl-azobenzene
TBA'	2,2',5,5'-tetra- <i>tert</i> -butyl-azobenzene
TBI	3,3',5,5'-N-benzylideneaniline
TS(T)	transition state (theory)
QST	quadratic synchronous transit
UV/Vis	ultraviolet/visual
WF	wave function
WP	wave packet

Chapter 1

Introduction

1.1 Molecular Switches at Surfaces

The outstanding development of technology has been leading to progressive miniaturization of components trying to scale them onto molecular size [1]. After exceeding progress of silicon nanoprocessing, molecular electronics may emerge. The challenge of making small devices out of molecular assemblies mutually communicating is still enormous. Putting molecules like pieces of a puzzle onto a surface in order to induce their cooperative response, that is supposed to be reversibly controlled and stable at the same time, is certainly not an easy task. For that matter one has to carefully think about possible varieties of building blocks that have the ability to fulfill such constraints. Applying concepts inspired from nature to synthetic systems can be a way of constructing devices at the nanoscale [2]. This idea has been introduced for the first time in the fifties by Hirshberg who was working on photochemical memory models based on spiropyrans [3]. The idea to induce a driven switch process via an external stimulus comes from the most astonishing example of that kind in nature: The *cis-to-trans* isomerization of the 11-*cis*-retinal Schiff base to the all-*trans* form in the photosensitive protein rhodopsin during the visual perception in the retina [4, 5, 6]. Proteins do not absorb visible light and it is clear that an organic chromophore, a photochromic system, has to be involved.

Photochromic molecules can absorb UV/Vis light due to which, for instance, conformational changes of the chromophore are induced. Through these conformational rearrangements, which strongly influence functionalities of molecules in complex systems, many processes can be controlled. Photochromic systems can perform an electronic transition of two chemical forms, with distinct absorption or emission spectra, induced by electromagnetic radiation. After light exposure, the chromophore finds itself in one of the higher excited states which is often followed by fast decay into the ground state. In the process most photochromic systems exhibit bond-cleavage (diarylethenes, dithienylethenes, fulgides, spiropyrans), $Z \rightarrow E$ isomerization (azobenzenes, stilbenes, indigoids), or oxidation-reduction reactions (cell chlorophyll).

Certain properties make photochromic systems interesting for the possible practical application, in particular for future devices [7]:

- a) Structural changes are reversible. The light induces a transition from a thermodynamically stable compound into metastable ones, and vice versa. The lifetime of the metastable form is decisive for technological applications.
- b) The isomerization induces changes of physical and chemical properties.
- c) Forward and backward reactions *may* proceed through an electronically excited singlet or triplet state.
- d) The back reaction can also be often induced thermally.
- e) Theoretically, forward and backward reactions can be repeated infinitely, but most systems experience a so-called “aging” processes. In practice a number of cycles ranging between $1-10^8$ is achieved. The loss of reversibility appears mostly upon photodegradation, photobleaching and photooxidation. This can represent the bottleneck for such systems, expressing a major limitation for practical use. The bacteriorhodopsin molecule is proven to have an extremely favorable fatigue resistance, managing to accomplish excellent reversibility [8].

In this work, we will mostly concentrate on molecules which experience conformational modifications upon some external stimulation. Azobenzene (AB) molecules fulfill most of the given terms (a-e) and represent an important class of molecules that are extensively incorporated as molecular switches [9], Fig. 1.1. They show pronounced photochromism and undergo a *cis*→*trans* isomerization (also $Z \rightarrow E$), where the two phenyls are on the same and opposite sides of the N=N group, respec-

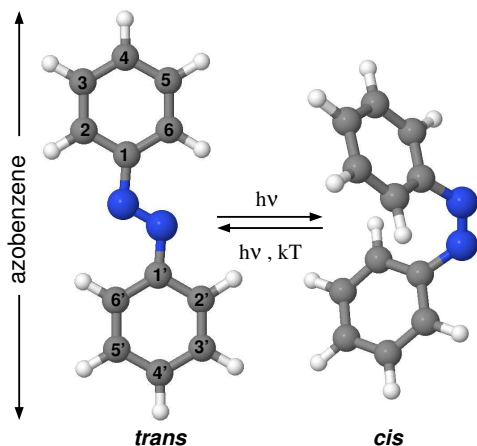


Figure 1.1: The *trans* and *cis* conformations of an azobenzene molecule, illustrated with the help of a ball-and-stick model. The molecule consists of two benzene rings (in grey) connected with an N=N double bond (in blue). The chemical formula is $C_{12}H_{10}N_2$. In the switching process, in the gas phase and in solution, photoisomerization operates by going from *trans*-to-*cis* molecules; the back reaction can be light or temperature induced.

tively (see Fig. 1.1). Changes induced by light often result in substantial molecular restructuring, for instance, AB changes from the quite “flat” and energetically more stable *trans* to the rather compact and three-dimensional *cis* form. Photochromic and temperature dependent behavior of AB molecules has been studied mostly in solution [7, 10]. More recently, these systems were also deposited on metal surfaces, and their response after interaction with a static electric field [11, 12], light [13, 14] or tunneling electrons [15] from a *Scanning Tunneling Microscope* (STM), has been studied. All these processes usually lead to the formation of a mixture of two states at a particular ratio, called, in the photochemical case, the *photostationary state*. Mounting the switches on surfaces is considered as one possible route towards practical molecular devices.

One of the very important features of the AB molecule is that it is suitable for substitution. Substituents can, depending on their electronic nature, size and position at the phenyl ring(s), influence among the electronic structure of AB itself, interactions between the molecules and the substrate, and the interactions between individual molecules in the assembly. Both of the interactions are of essential importance for the successful switching at a surface.

Recently, one of the most exploited systems for molecular switches, in solution and at surfaces [16, 17, 18], was the TBA molecule (see Fig. 1.2). The molecule contains four bulky *tert*-butyl groups which lift the NN moiety away from the surface. It is assumed that in this way the interaction of the “reactive part” with a metal substrate is reduced, since so far non-substituted AB has not been isomerized at

such a surface. Hence, this very strong interaction with the substrate changes to weak physisorption. For manipulation of TBA molecules at surfaces, scanning tunneling microscopy was quite successful. Generally, the STM represents a powerful tool for manipulating single molecules at surfaces, whether they are metals or semiconductors. The controlled positioning of an atom/molecule on a surface, the induction of a conformational change of a molecule [19, 20], the inducement of molecular motions [21] and the construction of nanostructures are just some applications

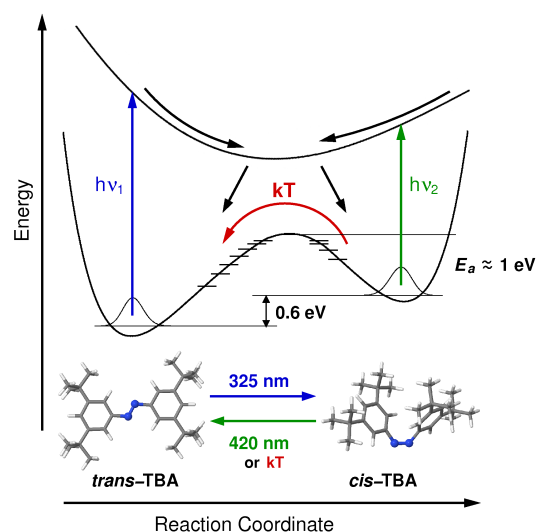


Figure 1.2: Sketch for optical or thermal isomerization of the TBA molecule.

of an STM. The TBA molecule has been successfully *trans*→*cis* isomerized at the Au(111) surface [11, 14]. The switch is, however, suppressed on Cu(111) and Au(100) [22], and on Ag(111) [23]. It turned out that the role of the substrate is more important than previously thought and that changes induced at the metal surface cannot be easily explained from a mechanistic point of view. The *cis*→*trans* isomerization is also not a well controlled process at the surface [11, 13], and this back reaction is usually induced thermally [17].

Theoretical analysis is necessary to understand the behavior of photochromic molecules, with and without the environment. It is of great importance to estimate the energy levels of the ground and excited electronic states, the corresponding geometry parameters, the activation energies of the switching systems together with the associated thermodynamical data, to describe mechanisms that lead to geometry changes in various environments, as well as to tune the isomerization barriers depending on the substituent and, in that way, control the kinetics. Only then one can understand the behavior of these systems better, influence their properties and model a successful molecular switch. For that purpose, *Density Functional Theory* offers a good compromise between accuracy and computational cost, especially for large molecules. It will be shown that isomerization kinetics can be treated on this level even in solution [24]. This is valid for covalently bonded systems on semiconductors, too [25].

1.2 Outline of this Work

This work is outlined as follows. In Chapter 2, theoretical concepts and models to study isomerization processes will be outlined. In Chapter 3, we will mostly focus on the most important features of AB molecules. This includes comments on the structure (mostly in the gas phase) and common features of the molecules, their absorption spectra, the calculation of potential energy surfaces (PESs) along the coordinates responsible for the ground state thermal isomerization, and calculation of anionic and cationic species which may be involved in isomerization processes at surfaces. Moreover, following STM experiments on DMC and TBA molecules, the effect of an external electric field on PESs of neutral and charged species will be studied in Chapter 4. In Chapter 5 thermal ground state isomerization of ABs and related molecules will be discussed, including their kinetics and the effect of (polar) environments. An extensive study of AB derivatives will be presented with the goal of systematically classifying the effects of substituents. Substitution will be extended further on to conjugated ABs - bisazobenzenes. Explicit treatment of a surface by a cluster model and the dynamics of the STM-induced switching process will be presented in Chapter 6 for the case of isomerization of COD@Si(001). Finally, we will conclude and give a short outlook in Chapter 7.

This research was made within the framework of the *Collaborative Research Center* Sfb 658, funded by the German Research Foundation (DFG). The concept of the project allowed direct cooperation with experimental researchers from the Free University Berlin (FUB), Humboldt University Berlin (HUB), Technical University Berlin (TUB), and Paul Drude Institute Berlin (PDI). Many of the explored molecules were synthesized in the groups of K. Rück-Braun from TUB [19], S. Hecht (HUB) [24] and R. Haag (FUB). Experimental insight in STM experiments was gained by work of J.I. Pascual, K. Franke and N. Henningsen (FUB), L. Grill (FUB) for ABs, and S. Fölsch and C. Nacci at the PDI for COD@Si(001) [25]. Calculations for systems explored with 2PPE methods and driven by light (TBA on Au(111) and Ag(111) [23]), were done due to collaboration with P. Tegeder, S. Hagen and M. Wolf (FUB).

Chapter 2

Theoretical Concepts

All the research presented in this work is based on quantum chemistry and quantum dynamics. In this Chapter the most important details about the methods will be introduced. In Section 2.1, quantum chemical concepts are discussed, as mostly incorporated in the Gaussian03 program package [26]. This program is used to calculate the spatial and electronic structure of molecules, normal modes, their thermochemical data, (transition) dipole moments, and absorption spectra. The calculations presented here are exclusively based on DFT methods, which provide a good balance between accuracy and computational effort. We also calculated PESs which were, further on, used for quantum dynamical treatment using wave packet methods, or detailed analysis of reaction paths and transition states.

2.1 Quantum Chemistry

2.1.1 Born-Oppenheimer Approximation

Solving the *Time-independent Schrödinger Equation* (TISE) of a molecule, gives the total energy of a system, E_{tot} , and its wave function (WF), Ψ :

$$\hat{H}_{mol}|\Psi\rangle = E_{tot}|\Psi\rangle. \quad (2.1)$$

Here, \hat{H}_{mol} is the molecular Hamilton operator describing the motion of electrons and all interactions between the electrons and nuclei of a particular system. Assuming that the molecule consists of N_A nuclei with masses M_A and nuclear charges $Z_A e$ at Cartesian coordinates \vec{R}_A surrounded by N electrons with mass m_e and charge $-e$ at coordinates \vec{r}_i , the molecular Hamiltonian is given as¹:

$$\begin{aligned}
\hat{H}_{mol} &= \hat{T}_{el} + \hat{T}_{nuc} + \hat{V}_{el,nuc} + \hat{V}_{el,el} + \hat{V}_{nuc,nuc} \\
&= \underbrace{-\frac{\hbar^2}{2m_e} \sum_{i=1}^N \nabla_i^2}_{\hat{T}_{el}} - \underbrace{\frac{\hbar^2}{2} \sum_{A=1}^{N_A} \frac{1}{M_A} \nabla_A^2}_{\hat{T}_{nuc}} - \underbrace{\frac{1}{4\pi\epsilon_0} \sum_{i=1}^N \sum_{A=1}^{N_A} \frac{Z_A e^2}{|\vec{r}_i - \vec{R}_A|}}_{\hat{V}_{el,nuc}} \\
&\quad + \underbrace{\frac{1}{4\pi\epsilon_0} \sum_{i=1}^N \sum_{j>i}^N \frac{e^2}{|\vec{r}_i - \vec{r}_j|}}_{\hat{V}_{el,el}} + \underbrace{\frac{1}{4\pi\epsilon_0} \sum_{A=1}^{N_A} \sum_{B>A}^{N_A} \frac{Z_A Z_B e^2}{|\vec{R}_A - \vec{R}_B|}}_{\hat{V}_{nuc,nuc}}.
\end{aligned} \tag{2.2}$$

In the atomic unit system one sets: $4\pi\epsilon_0 = \hbar = m_e = e = 1$. As a consequence, all energies are measured in units of E_h (Hartree), $1E_h = 4.3597 \times 10^{-18}$ J and all lengths are measured in units of a_0 (Bohr), $1a_0 = 0.52918 \text{ \AA}$. Eq.(2.2) becomes in atomic units:

$$\hat{H}_{mol} = - \sum_{i=1}^N \frac{\nabla_i^2}{2} - \sum_{A=1}^{N_A} \frac{\nabla_A^2}{2M_A} - \sum_{i=1}^N \sum_{A=1}^{N_A} \frac{Z_A}{|\vec{r}_i - \vec{R}_A|} + \sum_{i=1}^N \sum_{j>i}^N \frac{1}{|\vec{r}_i - \vec{r}_j|} + \sum_{A=1}^{N_A} \sum_{B>A}^{N_A} \frac{Z_A Z_B}{|\vec{R}_A - \vec{R}_B|}. \tag{2.3}$$

Since the mass of a nucleus is much larger than the mass of an electron, nuclear motion is assumed to be much slower compared to the motion of electrons. Based on this fact the *Born-Oppenheimer Approximation* [27] assumes movement of electrons in an electrostatic field of fixed nuclei. Hence, it is possible to separate electron and nuclear motions. This separation simplifies the TISE (2.1) because the total WF $|\Psi\rangle$ can be written as a product of a nuclear WF, $|\Psi_{nuc}\rangle$ and an electronic WF, $|\Psi_{el}\rangle$, *i.e.*:

$$|\Psi\rangle = |\Psi(\{\vec{r}_i\}, \{\vec{R}_A\})\rangle \approx |\Psi_{nuc}(\{\vec{R}_A\})\rangle \times |\Psi_{el}(\{\vec{r}_i\}; \{\vec{R}_A\})\rangle. \tag{2.4}$$

¹Nabla operator: $\vec{\nabla} = \frac{\partial}{\partial x} \vec{i} + \frac{\partial}{\partial y} \vec{j} + \frac{\partial}{\partial z} \vec{k}$.

This means that the nuclear WF $|\Psi_{nuc}\rangle$ depends only on coordinates of the nuclei while $|\Psi_{el}\rangle$ depends on coordinates of electrons and *parametrically* on coordinates of the nuclei. According to this, only those terms of the molecular Hamiltonian depending on electronic coordinates act on $|\Psi_{el}\rangle$. One thus obtains an electronic Schrödinger equation:

$$\hat{H}_{el}|\Psi_{el}\rangle = (\hat{T}_{el} + \hat{V}_{el,el} + \hat{V}_{el,nuc})|\Psi_{el}\rangle = E_{el}|\Psi_{el}\rangle. \quad (2.5)$$

Like $|\Psi_{el}\rangle$, also the electronic energy E_{el} depends parametrically on the coordinates of the nuclei. The solution of Eq.(2.5) provides the electronic energy, E_{el} , and WF $|\Psi_{el}\rangle$ at a particular molecular geometry.

E_{el} together with the nuclear repulsion term, $\hat{V}_{nuc,nuc}$, gives the potential energy surface as a function of nuclear coordinates:

$$\hat{V}_{PES}(\{\vec{R}_A\}) = \underbrace{\langle\Psi_{el}|\hat{H}_{el}|\Psi_{el}\rangle}_{E_{el}} + \hat{V}_{nuc,nuc}. \quad (2.6)$$

In general, Eq.(2.5) has different solutions E_{el}^i , $|\Psi_{el}^i\rangle$, each giving rise to its own PES,

$$\hat{V}_{PES}^i = E_{el}^i + \hat{V}_{nuc,nuc}. \quad (2.7)$$

PES of electronic states that are "energetically well separated" are being well described within the Born-Oppenheimer approximation. For each electronic state, i , a different nuclear Schrödinger equation can then be solved,

$$\hat{H}_{nuc}|\Psi_{nuc}^{i,n}\rangle = (\hat{T}_{nuc} + \hat{V}_i^{PES})|\Psi_{nuc}^{i,n}\rangle = E^{i,n}|\Psi_{nuc}^{i,n}\rangle, \quad (2.8)$$

where $E^{i,n}$ is the total energy corresponding to nuclear level n (translation, vibration, rotation) on the PES i .

2.1.2 Hartree-Fock Theory

The electronic Schrödinger equation (2.5), represents a multi-particle problem which means that some approximations need to be made in order to obtain its solutions. *Hartree-Fock theory* (HF) generates these solutions where the electron-electron in-

teraction is replaced by an average interaction. For the N -particle WF $|\Psi_{el}\rangle$, an antisymmetric product is made consisting of N single particle functions $\chi_j(\vec{x}_i)$, giving a so-called *Slater determinant* (SD):

$$|\Psi_{el}\rangle = \frac{1}{\sqrt{N!}} \begin{vmatrix} \chi_1(\vec{x}_1) & \chi_2(\vec{x}_1) & \cdots & \chi_N(\vec{x}_1) \\ \chi_1(\vec{x}_2) & \chi_2(\vec{x}_2) & \cdots & \chi_N(\vec{x}_2) \\ \cdots & \cdots & \cdots & \cdots \\ \chi_1(\vec{x}_N) & \chi_2(\vec{x}_N) & \cdots & \chi_N(\vec{x}_N) \end{vmatrix}. \quad (2.9)$$

$\chi_j(\vec{x}_i)$ is called the *spin-orbital*, defined as a product of *spatial orbital*, $\psi_j(\vec{r}_i)$, which depends only on Cartesian coordinates of an electron, and a *spin orbital*, $\alpha(\omega_i)$ or $\beta(\omega_i)$, that depends only on its spin coordinate:

$$\chi_j(\vec{x}_i) = \chi_j(\vec{r}_i, \omega_i) = \psi_j(\vec{r}_i) \cdot \begin{cases} \alpha(\omega_i) \\ \beta(\omega_i) \end{cases} \quad (2.10)$$

In HF we assume that the trial WF consists of a *single* SD. Choosing the single determinant as a trial function, the variational principle can be used to derive the HF equations, by minimizing the energy

$$\langle \Psi_{el} | \hat{H}_{el} | \Psi_{el} \rangle = \min, \quad (2.11)$$

subject to the boundary condition, that the χ_j are orthonormal. This gives the HF equations, which, when considering the closed-shell case (2 electrons per spatial orbital) and after eliminating the spin coordinate read

$$\hat{f}(\vec{r}_1)\psi_j(\vec{r}_1) = \varepsilon_j\psi_j(\vec{r}_1), \quad (2.12)$$

where ε_j are the orbital energies. The Fock operator \hat{f} is given as

$$\hat{f}(\vec{r}_1) = \hat{h}(\vec{r}_1) + \hat{V}^{HF} = \hat{h}(\vec{r}_1) + \sum_{j=1}^{N/2} \left(2\hat{J}_j(\vec{r}_1) - \hat{K}_j(\vec{r}_1) \right), \quad (2.13)$$

where

$$\hat{h}(\vec{r}_1) = -\frac{1}{2}\nabla_1^2 - \sum_{A=1}^{N_A} \frac{Z_A}{|\vec{r}_1 - \vec{R}_A|} \quad (2.14)$$

is a single particle operator describing the motion of a single electron in a field of all nuclei. \hat{V}^{HF} is the Fock potential which describes the interaction of an electron with an average field of other electrons. It consists of \hat{J}_j , the Coulomb operator, and \hat{K}_j , the exchange operator, *i.e.*:

$$\hat{J}_j(\vec{r}_1)\psi_i(\vec{r}_1) = \left[\int d\vec{r}_2 \psi_j^*(\vec{r}_2) \frac{1}{|\vec{r}_1 - \vec{r}_2|} \psi_j(\vec{r}_2) \right] \psi_i(\vec{r}_1) \quad (2.15)$$

$$\hat{K}_j(\vec{r}_1)\psi_i(\vec{r}_1) = \left[\int d\vec{r}_2 \psi_j^*(\vec{r}_2) \frac{1}{|\vec{r}_1 - \vec{r}_2|} \psi_i(\vec{r}_2) \right] \psi_j(\vec{r}_1). \quad (2.16)$$

The method used to solve Eq.(2.12) is called the *Self Consisted Field* (SCF) method [28]. This means that an initial guess needs to be made for orbitals ψ_j which are then used to calculate the \hat{J}_j and \hat{K}_j , and eventually the Fock operator \hat{f} . Solving the HF equations yields a new set of $\{\psi_j\}$ which are then employed to solve a new set of HF equations. This iterative procedure is repeated until convergence is reached.

Eq.(2.12) is integro-differential in 3D, which has to be solved numerically. An alternative was proposed by Roothaan [29] and Hall [30], who suggested to expand the HF orbitals into a set of atom centered orbitals, to transform Eq.(2.12) into a linear algebra problem. Specifically, the spatial orbitals ψ_j are expanded as a set of M known functions ϕ_ν called "basis functions" or "atomic orbitals" (AO)

$$\psi_j(\vec{r}) = \sum_{\nu=1}^M c_{j\nu} \phi_\nu(\vec{r}). \quad (2.17)$$

Eq.(2.17) is also referred to as the LCAO (linear combination of atomic orbitals) method used to calculate molecular orbitals. Now, the coefficients $c_{j\nu}$ need to be calculated. After using the variational principle again and vary the expectation value of the energy with respect to these coefficients, we get a matrix eigenvalue equation of the form:

$$\sum_{\nu}^M F_{\mu\nu} c_{j\nu} = \varepsilon_j \sum_{\nu}^M S_{\mu\nu} c_{j\nu}, \quad \forall \mu = 1, \dots, M \quad (2.18)$$

$$F_{\mu\nu} = \langle \phi_\mu | \hat{f} | \phi_\nu \rangle$$

$$S_{\mu\nu} = \langle \phi_\mu | \phi_\nu \rangle,$$

or in a matrix notation

$$\mathbf{FC} = \mathbf{SC}\varepsilon \quad (2.19)$$

where \mathbf{F} and \mathbf{S} are the Fock and overlap matrices, respectively. The matrix \mathbf{C} contains coefficients $c_{j\nu}$ of basis functions $\phi_\nu(\vec{r})$. Even if a large basis set is employed, the HF method yields only an approximation to the exact solution of the electronic Schrödinger equation (2.5). For highly accurate results, one has to go beyond the HF method. *Post*-HF methods provide effects denoted as "correlation" effects. The correlation energy is the difference between the "exact" energy eigenvalue of the N -electron Hamiltonian, and the SCF energy:

$$E_{corr} = E^{exact} - E^{SCF}. \quad (2.20)$$

As we shall see, in DFT methods, the correlation energy is automatically included through applied functionals.

2.1.3 Basis Sets

There are two commonly used types of functions to build the atomic orbitals $\phi_\nu(\vec{r})$: *Slater Type Orbitals* (STO)² and *Gaussian Type Orbitals* (GTO). The latter will be discussed in more detail. A Cartesian *Primitive Gaussian Type Orbital* (PGTO) is defined as

$$g(x, y, z) = N \cdot x^{l_x} \cdot y^{l_y} \cdot z^{l_z} \cdot e^{-\alpha(x^2+y^2+z^2)}. \quad (2.21)$$

Here, N is a normalization constant and the sum of l_x , l_y and l_z , *i.e.*, $l = l_x + l_y + l_z$, determines the type of orbital, having $l = 0$ for *s*-type, $l = 1$ for *p*-type, $l = 2$ for *d*-type orbitals, etc. However, because of the r^2 dependence, GTOs are describing rather poor the area near to the nucleus as well as parts far away from it, *i.e.*, in the tail ($r \rightarrow \infty$). GTOs are usually optimized for atoms, not being able to provide an adequate description of chemical bonds. In practice, one uses a linear combination of PGTOs, so-called "contracted" GTOs (CGTOs):

$$\phi_\nu(\vec{r}) = \sum_p d_{p\nu} g_p(\vec{r}). \quad (2.22)$$

²STOs are primarily used for atomic and diatomic systems where high accuracy is required.

The coefficients $d_{p\nu}$ are chosen such that the contractions describe electronic orbitals in most realistic way. In this work, *Pople style basis sets* are primarily used:

a) *STO- n G basis sets*. These mimic STOs by using n PGTOs. The exponents of PGTOs are determined by *fitting*, rather than optimizing them in a variational procedure. STO-3G is a widely used minimal basis.

b) *Split valence basis sets*. These basis sets have a general form given as k - nlm G. k represents how many PGTOs are used to represent the core orbitals. The nlm (after the dash) give the number of functions (PGTOs) taken to represent the valence orbitals as well as their splitting scheme. Two values (nl) indicate a split valence, while three values (nlm) represent a triple split valence. For instance, the 3-21G basis set has the core described with three PGTOs; valence orbitals are a contraction of two PGTOs plus one additional PGTO. Similarly, 6-311G is a triple split valence basis set; the core is a contraction of six PGTOs and valence orbitals are represented by three functions, consisting of three, one and one PGTOs, respectively [31].

To each of this basis sets extra diffuse [32] and/or polarization [33] functions can be added. Diffuse functions are s - and p -functions denoted as + or ++ before the G. The first plus indicates that extra functions have been added to heavy atoms; the second one means that diffuse functions are used for hydrogens, too. Polarization functions are denoted after the G with separated notation for heavy atoms and hydrogen. For instance, 6-31G(d) (identical to 6-31G*) is a split valence basis set with a single d -type polarization function on heavy atoms. In general, the quality of a basis set depends on numbers of contractions used per valence orbital as well as the number of PGTOs for each contraction. An increasing number of basis functions arises the computational cost, but the calculations become more accurate. For further information on commonly used basis sets in quantum chemistry, the reader is referred to Refs. [34, 35]

2.1.4 Density Functional Theory

2.1.4.1 Stationary Density Functional Theory

The size of the system of interest can become a problem for wave function based methods. As an alternative, Hohenberg and Kohn founded modern density func-

tional theory by proving that the electron density ρ contains enough information to calculate molecular energies [36]. The density is a function of spatial coordinates $\rho = \rho(\vec{r})$, while the energy is a function of the density $E[\rho]$, a so-called functional.

The whole theory is based on two major statements. The first Hohenberg-Kohn theorem says that the electron density uniquely determines the properties of the ground state, particularly the ground state energy, which can be expressed as

$$E_0[\rho] = E_0^{HK}[\rho] = T[\rho] + V[\rho] + J[\rho] + E_{xc}[\rho]. \quad (2.23)$$

Here, the kinetic energy of electrons is $T[\rho]$, their interaction with the nuclei $V[\rho]$, the electron-electron repulsion $J[\rho]$ and finally, the exchange-correlation energy for the electrons $E_{xc}[\rho]$. The $V[\rho]$ term is usually expressed as

$$V[\rho] = \int \rho(\vec{r})v(\vec{r})d\vec{r}, \quad (2.24)$$

where $v(\vec{r})$ is defined as an external static potential acting on the system. Basically, $v(\vec{r})$ doesn't need to be restricted to Coulomb potentials only.

The second Hohenberg-Kohn theorem states that varying the trial density $\rho(\vec{r})^3$ will give, by a variational principle, an energy greater than or equal to the true ground state energy

$$E_0^{HK} \geq E_0^{exact} \quad (2.25)$$

where E_0^{HK} is the energy functional of (2.23).

In Eq.(2.23), the kinetic energy is introduced also as a functional. Kohn and Sham showed a practical method to compute $T[\rho]$ using *Kohn-Sham orbitals* ψ_i [37, 38]:

$$T[\rho] = -\frac{1}{2} \sum_i^N \langle \psi_i(\vec{r}) | \nabla^2 | \psi_i(\vec{r}) \rangle \quad (2.26)$$

so that the ground state energy of an N -electron system can be written, in analogy

³The trial density needs to fulfill two additional constrains: (i) $\rho(\vec{r}) \geq 0$ and (ii) $\int \rho(\vec{r})d\vec{r} = N$, where N is the number of electrons.

to Eq.(2.23), as

$$E_0[\rho] = -\frac{1}{2} \sum_{i=1}^N \int \psi_i^*(\vec{r}) \nabla^2 \psi_i(\vec{r}) d\vec{r} - \int \rho(\vec{r}) v(\vec{r}) d\vec{r} + J[\rho] + E_{xc}[\rho]. \quad (2.27)$$

The electron density is expressed by

$$\rho(\vec{r}) = \sum_{i=1}^N |\psi_i(\vec{r})|^2. \quad (2.28)$$

Varying the total energy expression (2.27) with respect a set of orbitals (2.28), we obtain the Kohn-Sham equations (KS):

$$\left[-\frac{1}{2} \nabla^2 + v_{eff}(\vec{r}) \right] \psi_i(\vec{r}) = \varepsilon_i \psi_i(\vec{r}) \quad (2.29)$$

with ε_i as eigenenergies of KS orbitals. The KS equations represent Schrödinger equations for a fictitious system of non-interacting electrons. These generate the same density as the system of interacting particles. In analogy to the HF equations, the KS equations are solved iteratively. In Eq.(2.29), $v_{eff}(\vec{r})$ is an "effective potential" (also known as KS potential), defined as:

$$v_{eff}(\vec{r}) = v(\vec{r}) + \int \frac{\rho(\vec{r}')}{|\vec{r} - \vec{r}'|} d\vec{r}' + \underbrace{\frac{\delta E_{xc}[\rho]}{\delta \rho(\vec{r})}}_{v_{xc}(\vec{r})}. \quad (2.30)$$

The last term of Eq.(2.30) is the exchange-correlation potential (a functional derivative of E_{xc}). The corresponding energy term E_{xc} is not generally known in the KS approach to DFT.

To search for an accurate $E_{xc}[\rho]$ is one of the greatest challenges in density functional theory. One of the simplest solutions for this problem was proposed, the *Local Density Approximation* (LDA) for the exchange and correlation energy

$$E_{xc}^{LDA}[\rho] = \int \rho(\vec{r}) \varepsilon_{xc}(\rho) d\vec{r}. \quad (2.31)$$

Here, ε_{xc} represents the exchange and correlation energy per electron. The corre-

sponding exchange-correlation potential, to be used in Eq.(2.30), becomes

$$v_{xc}^{LDA}(\vec{r}) = \frac{\delta E_{xc}^{LDA}}{\delta \rho(\vec{r})} = \varepsilon_{xc}(\rho(\vec{r})) + \rho(\vec{r}) \frac{\partial \varepsilon_{xc}(\rho)}{\partial \rho}. \quad (2.32)$$

For open shell-systems, the *Local Spin Density Approximation* (LSDA) is applied. Usually, fitting schemes are developed in order to connect the local density values with global properties. One of the widely used L(S)DA schemes is containing the Slater exchange combined with the VWN (Vosko, Wilk and Nusair) correlation energy expression; this is also called the SVWN method. The L(S)DA schemes are based on a uniform electron gas model. In reality, a molecular system is far from spatially uniform which makes the LDA solution limited. A way of improving the exchange-correlation functional is to introduce the *Generalized Gradient Approximation* (GGA) in which the LDA is corrected by an simple additional term which contains the gradient of the density [39]

$$\varepsilon_{x/c}^{GGA}[\rho(\vec{r})] = \varepsilon_{x/c}^{LDA}(\vec{r}) + \Delta \varepsilon_{x/c} \left[\frac{|\nabla \rho(\vec{r})|}{\rho^{4/3}(\vec{r})} \right]. \quad (2.33)$$

where the subscript x/c indicates that the same functional form is valid for either exchange or correlation. Most of the GGA functionals are constructed following the Eq.(2.33), containing just a correction to the exchange/correlation energy. Concerning correlation functionals, those that follow Eq.(2.33) are P86 (Perdew), PW91 (Perdew and Wang), B95 (Becke). Concerning GGA exchange functionals, the most popular is the one of Becke, denoted as "B" (also B88), which contains a single empirical parameter and appropriate asymptotic behavior of the energy density. Alternatively, other exchange functionals are available as well, *e.g.* those that contain no empirically optimized parameters, like B86 (Becke), P (Perdew and Wang), and PBE (Perdew, Burke, and Ernzerhof). Usually, one combines the exchange and correlation functionals as in an example of BLYP which contains the exchange functional of Becke (also B88) and the GGA correlation functional of Lee, Yang and Parr (LYP). The LYP correlation functional does not just correct the LDA expression but computes the full correlation energy. In our calculations, the B3LYP functional [39, 40] was mostly applied:

$$E_{xc}^{B3LYP} = (1 - a)E_x^{LSDA} + aE_x^{HF} + b\Delta E_x^{B88} + (1 - c)E_c^{VWN} + cE_c^{LYP}. \quad (2.34)$$

This functional is a hybrid of "exact", HF-like, exchange which is mixed with local and gradient corrected exchange and correlation terms. Becke suggested parameters $a = 0.20$, $b = 0.72$ and $c = 0.81$ based on fitting to heats of formation of small molecules [39, 40]. The OLYP and O3LYP are functionals similar to BLYP and B3LYP, respectively, but use the exchange functional OPTX (Handy and Cohen) [41], in place of the standard B88 exchange. PBE1PBE is another hybrid functional (also called PBE0), which contains 25% contribution of the HF exchange and was not empirically optimized, thus there are "zero" parameters.

One has to notice that one of the positive properties of DFT is that at relatively low computational cost, one gets already correlated molecular energies. Nevertheless, one of the major drawbacks is that calculated energies depend very much on the chosen functional E_{xc} which is not known exactly, except for model systems.

2.1.4.2 Time-dependent Density Functional Theory

All electronic excited states and UV/Vis absorption spectra in this work, are calculated using the *Time-dependent Density Functional Theory* (TD-DFT) [42]. The Hohenberg-Kohn-Sham formulation of DFT is time-independent and thus, it does not cover problems involving time-dependent fields, which are present in molecular optics and spectroscopy. This requires a generalization of the basic formalism of DFT to the time-dependent case. Accordingly we solve KS equations of the form

$$\left[-\frac{1}{2}\nabla^2 + v(\vec{r}, t) + \int \frac{\rho(\vec{r}', t)}{|\vec{r} - \vec{r}'|} d\vec{r}' + v_{xc}(\vec{r}, t) \right] \psi_i(\vec{r}, t) = i \frac{\partial}{\partial t} \psi_i(\vec{r}, t) \quad (2.35)$$

with

$$\rho(\vec{r}, t) = \sum_i^N |\psi_i(\vec{r}, t)|^2. \quad (2.36)$$

Here, $v(\vec{r}, t)$ is defined, like before, as an external potential having the role of an external perturbation to the system, *i.e.*, the nuclear potential plus a time-dependent electric field, for example. The electron density, KS orbitals and the exchange-correlation potential are now time-dependent. Under the so-called *adiabatic approximation* the time-dependence is simplified. This approximation leads to the application of exchange-correlation functionals which happen to be the same as in

the time-independent theory but using the electron density at a particular time t , $\rho^t(\vec{r})$:

$$v_{xc}(\vec{r}, t) = \frac{\delta E_{xc}[\rho]}{\delta \rho(\vec{r}, t)} \cong \frac{\delta E_{xc}[\rho]}{\delta \rho^t(\vec{r})}. \quad (2.37)$$

In linear-response theory, the response of the system to an external field is characterized by the dynamic polarizability. The dynamic polarizability, $\alpha(\omega)$, is frequency dependent and describes the response of a dipole moment to a time-dependent electric field which oscillates with the corresponding frequency ω . It can be calculated from the response of an electron density obtained from TD-DFT. The polarizability $\alpha(\omega)$ is related to the oscillator strength f_i and the electronic excitation $\omega_i = E_i - E_0$ by the sum-over-states expression

$$\alpha(\omega) = \frac{1}{3} \text{Tr}(\underline{\underline{\alpha}}(\omega)) = \sum_i \frac{f_i}{\omega_i^2 - \omega^2}. \quad (2.38)$$

Here, $\underline{\underline{\alpha}}(\omega)$ is the (dynamic) polarizability tensor. $\alpha(\omega)$ has poles appearing at $\omega_i = E_i - E_0$ corresponding to the excitation energies, and the residues

$$f_i = \frac{2}{3} (E_i - E_0) (|\langle \psi_0 | \vec{r} | \psi_i \rangle|^2) \quad (2.39)$$

are the oscillator strengths.

In practice, excitation energies for continuous-wave excitation can be determined as solutions of a time-independent eigenvalue problem [42, 43]. TD-DFT is often able to produce good results for low energy excitations. Higher excitation energies are often overestimated, sometimes by more than 1 eV [42]. Bad performance of TD-DFT was also found for excitations of the charge transfer type [44].

2.1.5 Polarizable Continuum Model

Within the presented DFT methods, the *Polarizable Continuum Model* (PCM) was sometimes employed, to mimic the presence of a solvent environment. Experimentally, most of the results concerning rate constants and absorption spectra are from measurements in solvents. Solution environments have an influence on measured rates and spectra, as well as on structures of molecules. From a computational per-

spective, however, it is not simple to treat solvent effects in an exact way. Namely, including explicitly a sufficient number of solvent molecules into calculations is unpractical and expensive. An alternative is a *continuum model*. Here, the environment is represented as a uniform polarizable medium with the solute placed in a suitably shaped cavity in this environment [35, 45].

If the molecule is placed in a solvent described as a polarizable continuum medium it will experience: (i) Energy stabilization and (ii) an increased dipole moment, depending on its polarizability. Quantitatively, this is described within the Onsager

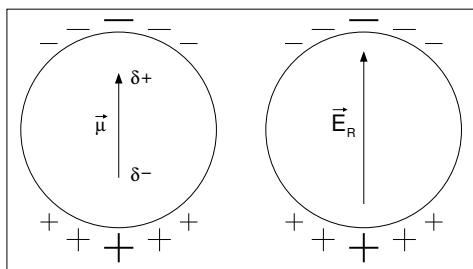


Figure 2.1: The dipole moment $\vec{\mu}$ associated with two point charges inside a spherical cavity. The induced polarization of the solvent is represented with + and -. The resulting field is denoted as \vec{E}_R .

model [46]. The permanent dipole moment of the isolated molecule $\vec{\mu}$ is associated with n point charges by

$$\vec{\mu} = \sum_{i=1}^n q_i \vec{r}_i \quad (2.40)$$

where q_i and \vec{r}_i are the charge and the position vector of the i -th point charge, respectively.

Let us first assume that the molecule fills a spherical cavity of radius a , which reflects the size of a molecule, surrounded by solvent described as a continuous medium with dielectric constant ϵ . The electric field associated with the molecular dipole $\vec{\mu}$ polarizes the solvent. This polarization of the solvent will give rise to an additional electric field, \vec{E}_R , at the molecular dipole. This field is called the *reaction field*, see Fig. 2.1. The reaction field is proportional to the dipole moment through (we use atomic units)

$$\vec{E}_R = f \vec{\mu} = \frac{2(\epsilon - 1)}{2\epsilon + 1} \frac{\vec{\mu}}{a^3} \quad (2.41)$$

where the proportionality factor f depends on the dielectric constant ϵ and the cavity radius a . The interaction energy between the dipole and the reaction field is given by a reaction potential

$$V_R = -\vec{\mu} \cdot \vec{E}_R. \quad (2.42)$$

In a quantum mechanical version of the method, the solute molecule is described

by a Schrödinger equation and the interaction with the solvent is included through a reaction potential ($\hat{V}_R = V_R$) given in Eq.(2.42) that acts as perturbation to the solute Hamiltonian \hat{H}_0 . That is, for the gas phase (vacuum) case we have

$$\hat{H}_0\Psi_0 = E_0\Psi_0, \quad (2.43)$$

and in the solution

$$\left[\hat{H}_0 + \frac{1}{2}\hat{V}_R \right] \Psi = E\Psi, \quad (2.44)$$

where $\Psi_0(E_0)$ and $\Psi(E)$ are solute WF(energy) in vacuum and solution, respectively. Calculated electric dipole moments of the solute molecule induce charges in the dielectric medium, which in return acts back on the solute influencing its wave function and hence its energy and dipole moment. The interaction of the solute molecule with an environment needs to be calculated in an iterative procedure, within the so-called *Self-Consistent Reaction Field* (SCRF) methods. When the back-polarization of the molecule is taken into account, the dipole moment of the solute changes to:

$$\vec{\mu}^* = \vec{\mu} + \alpha\vec{E}_R^* \quad (2.45)$$

where α is the polarizability of the solute molecule and \vec{E}_R^* the reaction field of the polarizable dipole⁴. Equation (2.41) becomes

$$\vec{E}_R^* = f\vec{\mu}^* = f(1 - f\alpha)^{-1}\vec{\mu} = \frac{2(\varepsilon - 1)}{2\varepsilon + 1} \left(1 - \frac{2(\varepsilon - 1)\alpha}{2\varepsilon + 1} \frac{1}{a^3} \right) \frac{\vec{\mu}}{a^3}. \quad (2.46)$$

In general, the molecule is not spherical. The choice of the shape and the size of the cavity is one of the most delicate steps of the continuum solvation models. Ideally, the cavity should have the “molecular shape” but in practice, it is constructed out of interlocking spheres, centered on atoms or atomic groups. Typically used spheres have atomic radii according to the van der Waals values, giving a so-called “van der Waals surface”. This is at the same time the *Solvent Excluded Surface* (SES). Here, spheres are forming small “pockets” making the area, denoted with a thick blue line in Fig. 2.2, solvent inaccessible with $\varepsilon = 1$. The part which surrounds the SES is called *Solvent Accessible Surface* (SAS) with $\varepsilon \neq 1$.

⁴Here, the tensor character of the polarizability has been neglected.

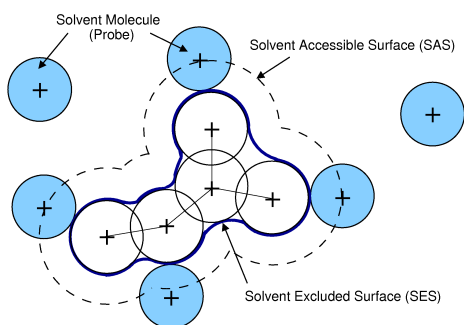


Figure 2.2: Schematic representation of the SAS, described as the traced out area around the solute molecule. SES is the direct boundary to the solute molecule not coming in contact with the probe, *i.e.*, solvent molecules.

The PCM is one of the oldest *Apparent Surface Charge* (ACS) approaches in which a charge distribution $\sigma(\vec{r})$ is spread on the cavity surface, position dependent and calculated as

$$\sigma(\vec{r}) = \frac{\varepsilon - 1}{4\pi\varepsilon} \vec{E}_{in}(\vec{r}) \cdot \vec{n}(\vec{r}) \quad (2.47)$$

using the electric field inside the cavity $\vec{E}_{in}(\vec{r})$ and a vector $\vec{n}(\vec{r})$ normal to the SES. The potential \hat{V}_R is composed out of two contributions, the one which comes from the solute molecule M (dependent on the solute charge distribution [47]) and the one coming from the charge distribution σ , *i.e.*⁵:

$$\hat{V}_R = \hat{V}_M + \hat{V}_\sigma \quad (2.48)$$

If we denote the cavity surface as Σ and \vec{s} as a vector which defines a point on Σ , the contribution to the potential \hat{V}_R can be defined as

$$\hat{V}_\sigma(\vec{r}) = \int_{\Sigma} \frac{\sigma(\vec{s})}{|\vec{r} - \vec{s}|} d^2\vec{s}. \quad (2.49)$$

The advantage of the ACS formulation is that the electrostatic problem is derivable from the Gauss theorem [48]

$$\int_{\Sigma} \sigma(\vec{s}) d^2\vec{s} = -\frac{\varepsilon - 1}{\varepsilon} Q_M \quad (2.50)$$

where Q_M is the total charge of M . A violation of this condition is often the case in quantum mechanical calculations leading to significant numerical errors. The surface Σ is then approximated in terms of finite elements, *tesserae*, small enough to consider $\sigma(\vec{s}_k)$ constant within each tessera. Then it is possible to define a set of point charges q_k placed at the center of the tessera covering the cavity of surface

⁵If the solute charge distribution is not affected by the presence of a dielectric $\hat{H} = \hat{H}_0 + \hat{V}_\sigma$.

ΔA_k in which the solute molecule is embedded. The integral in Eq.(2.49) becomes:

$$\hat{V}_\sigma(\vec{r}) \cong \sum_k \frac{\sigma(\vec{s}_k)\Delta A_k}{|\vec{r} - \vec{s}_k|} = \sum_k \frac{q_k}{|\vec{r} - \vec{s}_k|}. \quad (2.51)$$

The first version of PCM was renamed to DPCM (D stands for dielectric) while the PCM name has been adopted for the entire family of models available at the time. The *Integral Equation Formalism* (IEF), originally formulated by Cancès and Mennucci [49, 50] and based on standard ACS formulation, is a member of the PCM suite of solvation codes implemented in Gaussian program packages. IEF is the default method for the keyword "PCM" in the Gaussian03 version [26], see Refs. [45, 49, 50, 51].

2.1.6 Transition State Theory

In this part we consider an approximate approach to calculate the rate constants of chemical reactions, the Eyring *transition state theory* (TST). It is assumed that the progress of a reaction is direct. In the first approximation it is assumed that the reaction proceeds along the minimum energy path. The reaction runs through a saddle point which separates reactants from products, representing the bottleneck of a reaction. This intermediate configuration is the *transition state* (TS), with the corresponding geometrical structure, the *transition structure*. In the second approximation the TS is considered as a point of no return; if the saddle-point is reached the reaction proceeds directly to the products. During the reaction the TS, or activated complex, is considered to be in thermal equilibrium with the reactants and products. The symbol ‡ is used to represent the activated complex.

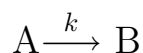
TST is essentially a semi-classical theory where the dynamics along the *reaction coordinate* (RC) are treated classically, while the "perpendicular directions" (Fig. 2.3, left) take into account the quantization of, for instance, vibrational energy. Minima of a PES are characterized by the fact that all normal modes and corresponding force constants are positive. The TS is a stationary point on a multi-dimensional PES. It is a stable point in all dimensions except one, where the second-order derivative of the potential is negative. This degree of freedom is the reaction coordinate.

Along the RC the surface slopes downward, thus, the force constant of this mode is negative. The TS of the first order has one and only one negative force constant (imaginary frequency).

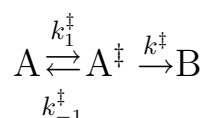
The TS of a unimolecular chemical reaction, isomerization and desorption for instance, is defined as the configuration with the highest energy along the RC. The energy relative to the reactant is the activation energy and its value, among other parameters, determines the reaction rate constant k (see below). In order to find appropriate TSs, a number of methods is available and we will present some of them in Section 2.1.6.2.

2.1.6.1 The Eyring Equation

Transition state theory, introduced in the 1930s by Eyring [52] and Evans and Polanyi [53], provided the one of the first attempts to determine absolute reaction rates. Here, a simplified derivation, which leads to the Eyring expression, for unimolecular reactions is used



where we assume that the reaction is irreversible. At any given time, only a subset of molecules A will have sufficient energy to undergo a conversion to B. Further, the reactive molecules are in equilibrium with the unreactive species, we can relate the relative populations by an equilibrium constant K^\ddagger :



$$[A^\ddagger] = (k_1^\ddagger/k_{-1}^\ddagger) \cdot [A] = K^\ddagger[A] \quad (2.52)$$

Since we assumed that only reactive molecules, A^\ddagger , undergo a transformation to B, we can write

$$k[A] = k^\ddagger[A^\ddagger] \quad (2.53)$$

and the rate constant is

$$k = k^\ddagger \frac{[A^\ddagger]}{[A]} = k^\ddagger K^\ddagger. \quad (2.54)$$

If we use $k(T) = (k_B T/h) \cdot K^\ddagger$ [54], from Eyring, and the van't Hoff relation $\Delta G^\ddagger(T) = -RT \ln K^\ddagger$, we arrive to the Eyring equation

$$k(T) = \frac{k_B T}{h} e^{-\frac{\Delta G^\ddagger(T)}{RT}} \quad (2.55)$$

where ΔG^\ddagger is the activation free energy at a particular temperature, calculated as

$$\Delta G^\ddagger = G^\ddagger - G(R). \quad (2.56)$$

Here, G^\ddagger is the free energy of the TS and $G(R)$ the free energy of the reactant. Expression (2.55) will be applied in Chapter 5 for calculating thermal isomerization rates of azobenzenes.

2.1.6.2 Transition State Search

Practically, locating minima on the PES is fairly simple [34]. Finding first-order saddle points is much more difficult. There is still no general method guaranteeing success in locating TSs, but there are different strategies, which can be roughly divided into two subgroups: (i) Those based on interpolation between two minima [55] and (ii) those that use only local parameters [56]. Former ones require knowledge about reactants and products of the reaction because the TS is assumed to be somewhere between these two structures. Worth noticing is that these methods usually don't locate the exact TS but a point close to it. In practice, this "located" structure needs to be further optimized until the TS is reached. Local methods, on contrary, require no previous information about reactants and products but a good estimate of the TS structure in order to converge. Once a TS has been found, the whole reaction path can be determined by tracing the *Intrinsic Reaction Coordinate* (IRC) [57]. The IRC is determined by a steepest descent based algorithm [58] which, using small steps along the negative gradient in a mass-weighted coordinate system, describes a molecular reaction from the TS towards the reactant and product (see Fig. 2.3, right). The IRC is often defined as the "real" reaction path.

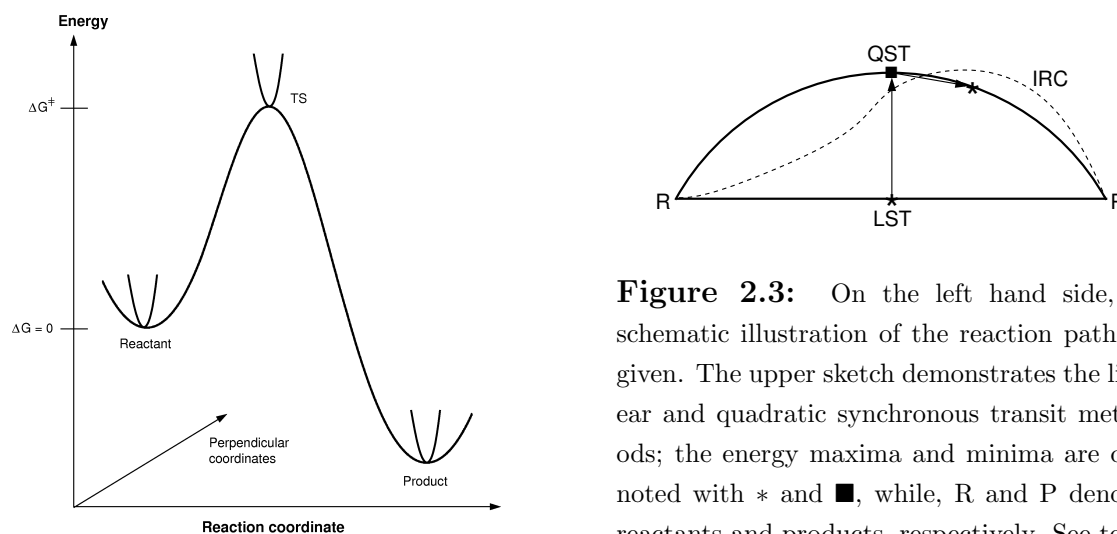


Figure 2.3: On the left hand side, a schematic illustration of the reaction path is given. The upper sketch demonstrates the linear and quadratic synchronous transit methods; the energy maxima and minima are denoted with * and ■, while, R and P denote reactants and products, respectively. See text for explanation.

The crucial step in locating a TS is to select one or a few internal "reaction" coordinates which describe most important differences between the reactant and product(s). Following conformational changes, for instance, such a coordinate is usually a torsional angle. Selected coordinates are often kept fixed while others are optimized. Such methods are called *coordinate driving* [34]. *Linear Synchronous Transit* (LST) is a coordinate driving method where all the coordinates are interpolated linearly between the reactant and the product geometries, as indicated in Fig. 2.3, right. After interpolation no optimization is performed and the TS is, in this case, the highest energy structure along the interpolation line. This approximate method works well for "simple" systems only.

If we approximate the reaction path as a parabola, instead of a straight line, we are speaking of the *Quadratic Synchronous Transit* (QST) method. Once a maximum is found, using the LST method, the QST is generated by minimizing the energy perpendicular to the LST path. In Fig. 2.3, a direct comparison between the LST, QST and IRC methods is given.

In our calculations, usually QST2 or QST3 methods were applied. Both methods are versions of *synchronous transit-guided quasi-Newton* methods (STQN) developed by H.B. Schlegel and coworkers [59, 60, 61]. The method uses a circle arc, instead of a parabola, for interpolation. Further, the tangent to the circle is used to guide the search toward the TS which is, when located, further optimized on a quasi-Newton-

Raphson level [34] (NR). Using NR we are generating the search toward a first-order saddle point, *i.e.* optimizing in the uphill direction on a PES. Further, the difference among QST2 and QST3 methods needs to be clarified. If a TS structure cannot be guessed, QST2 needs structures of both, reactant and product(s). QST3 requires specification of the previously defined TS in addition, which simplifies the search of a structure in particular for systems which possess more than one TS on the reaction path. Often, this method converges easily reducing computational effort which is important, especially, for large systems.

2.2 Time-dependent Schrödinger Equation

We have already seen that the solution of the time-independent nuclear Schrödinger equation (2.1) yields rovibrational eigenstates and eigenenergies of the molecular system. In order to observe the time evolution of a reaction of interest, as in our case the dynamics of the COD@Si(001) switching (see Chapter 6), we have to solve the time-dependent nuclear Schrödinger equation (TDSE) instead, which generally reads

$$i\hbar \frac{\partial}{\partial t} |\psi(t)\rangle = \hat{H} |\psi(t)\rangle. \quad (2.57)$$

The Hamiltonian \hat{H} will be defined later. The general solution of Eq.(2.57) can be expressed as

$$|\psi(t)\rangle = \hat{U}(t; t_0) |\psi(t_0)\rangle \quad (2.58)$$

where $\hat{U}(t; t_0)$ is called *time evolution operator*, or shortly *propagator*. It propagates the WF $|\psi\rangle$ at time t_0 to some final time t and can be written for a time-independent Hamiltonian as

$$\hat{U}(t; t_0) = e^{-\frac{i}{\hbar} \hat{H}(t-t_0)} \quad , \quad \hat{H} \neq \hat{H}(t). \quad (2.59)$$

2.2.1 Propagation Methods

For a numerical solution of Eq.(2.57), $|\psi(t)\rangle$ is represented with a finite basis set consisting of N basis functions, in which \hat{H} becomes a $N \times N$ hermitian matrix \mathbf{H} ,

and the WF, a vector $|\vec{\psi}\rangle$. Therefore, expression (2.58) is calculated as:

$$|\vec{\psi}(t)\rangle = \mathbf{U}(t; t_0)|\vec{\psi}(t_0)\rangle = e^{-\frac{i}{\hbar}\mathbf{H}(t-t_0)}|\vec{\psi}(t_0)\rangle. \quad (2.60)$$

The term $\mathbf{U}(t; t_0)$ is an exponential function that can be rewritten as a Taylor expansion:

$$e^{-\frac{i}{\hbar}\mathbf{H}(t-t_0)} = \mathbf{1} - \frac{i(t-t_0)}{\hbar}\mathbf{H} - \frac{1}{2}\left(\frac{(t-t_0)}{\hbar}\right)^2\mathbf{H}^2 + \dots \quad (2.61)$$

2.2.1.1 Propagation in Eigenfunction Space -"Exact" Propagation

If one expands WF $|\psi(t_0)\rangle$ in the basis of eigenfunctions ψ_i of \mathbf{H} , *i.e.*,

$$\begin{aligned} \hat{H}\psi_i &= \varepsilon_i\psi_i \\ |\psi(t_0)\rangle &= \sum_i^N c_i(t_0)|\psi_i\rangle \\ c_i(t_0) &= \langle\psi_i|\psi(t_0)\rangle \end{aligned} \quad (2.62)$$

then \mathbf{H} is diagonal with elements H_{ii} given by the corresponding eigenvalues ε_i . Using Eq.(2.61) we can write the Taylor expansion of every element separately since:

$$(\mathbf{H}^n)_{ij} = \varepsilon_i^n \delta_{ij}. \quad (2.63)$$

This leads to a rather trivial solution of TDSE (2.57) in the eigenfunction basis:

$$|\psi(t)\rangle = \sum_i^N c_i(t_0)e^{-\frac{i}{\hbar}\varepsilon_i(t-t_0)}\psi_i. \quad (2.64)$$

However, in order to achieve this one needs eigenfunctions of \mathbf{H} , which we can obtain by numerical diagonalization of the matrix. This requires numerical effort proportional to N^3 and memory proportional to N^2 . Because of this, it is very hard to apply this propagation scheme for multidimensional problems with a large number of states N .

2.2.1.2 Time Discretization

The numerical propagation of the TDSE is often done on an *equidistant time grid*. The solution of the TDSE (2.57) can be written as a product of “partial” evolution operators $\hat{U}(t_i; t_{i-1})$, each of them propagating the WF on small time steps Δt :

$$|\psi(t)\rangle = \hat{U}(t; t_n)\hat{U}(t_n; t_{n-1})\dots\hat{U}(t_1; t_0)|\psi(t_0)\rangle. \quad (2.65)$$

In agreement with Eq.(2.59), each partial propagator is given as:

$$\hat{U}(t_i; t_{i-1}) = e^{-\frac{i}{\hbar}\hat{H}(t_i-t_{i-1})} = e^{-\frac{i}{\hbar}\hat{H}\Delta t} \quad , \quad t_i - t_{i-1} = \Delta t. \quad (2.66)$$

2.2.2 The Gadzuk Jumping Wave Packet Scheme

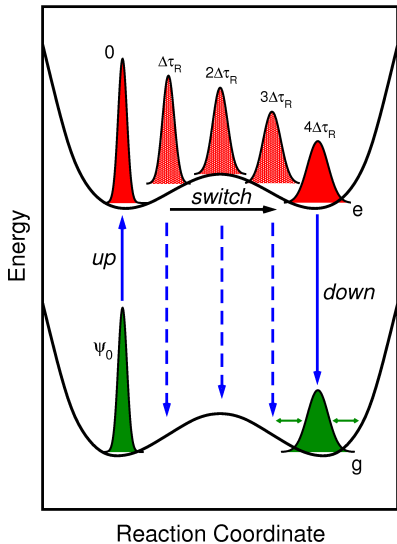


Figure 2.4: Illustration of Gadzuk’s jumping wave packet scheme for a two-state double-minimum problem applicable to a switching process (SIET), see text.

Below we will describe the isomerization dynamics of COD@Si(001) by a two-state model, with a ground state (g) and an excited state (e), where the excited state has a finite (ultrashort) lifetime τ_{el} . The excitation process $g \rightarrow e$ will be modeled as a sudden initial transition. Gadzuk’s *jumping wave packet* model was one of the first attempts to treat dissipative problems of this kind using stochastic methods, first applied for laser-induced desorption of NO from Pt(111) [62, 63]. Within this approach we will study *Switching Induced by Electronic Transitions* (SIET) which is analogous to *Desorption Induced by Electronic Transitions* (DIET) [64, 65, 66]. The method implies running numerous “excitation-deexcitation quantum trajec-

“tories”, with different *residence times* τ_R on the excited state potential. The equation governing the time-evolution of the wave function is given, for a chosen residence

time τ_R , by:

$$|\psi(t; \tau_R)\rangle = e^{-\frac{i}{\hbar}\hat{H}_g(t-\tau_R)}|g\rangle\langle e|e^{-\frac{i}{\hbar}\hat{H}_e\tau_R}|e\rangle\langle g|\psi_0\rangle. \quad (2.67)$$

The whole scheme, as pictured in Fig. 2.4, runs over two steps. In this equation, the ground state WF $|\psi_0\rangle$ is projected on the excited state $|e\rangle$, propagated for some residence time τ_R on the excited electronic state, dumped back to the ground state $|g\rangle$ and then propagated until the final time t . The $|\psi(t_0)\rangle$ is the initial wave function at $t = 0$ and $T = 0$ K and \hat{H}_g and \hat{H}_e are the ground and excited state Hamiltonians of the system, respectively. Operator expectation values for single trajectories are calculated as:

$$A(t; \tau_R) = \langle \psi(t; \tau_R) | \hat{A} | \psi(t; \tau_R) \rangle. \quad (2.68)$$

Final observables are computed applying incoherent averaging of all trajectories. Assuming a coordinate-independent electronic lifetime, τ_{el} of the excited state, we finally have:

$$\langle \hat{A} \rangle(t) = \frac{\int_0^{\infty} e^{-\tau_R/\tau_{el}} A(t; \tau_R) d\tau_R}{\int_0^{\infty} e^{-\tau_R/\tau_{el}} d\tau_R} \quad (2.69)$$

where $e^{-\tau_R/\tau_{el}} d\tau_R / \int_0^{\infty} e^{-\tau_R/\tau_{el}} d\tau_R$ is the probability that the excited state decays between τ_R and $\tau_R + \Delta\tau_R$. Residence times are usually calculated with constant spacing, *i.e.*, on a discrete time grid so that the integrals simplify to

$$\langle \hat{A} \rangle(t) = \frac{\sum_{n=0}^{N-1} e^{-\tau_{Rn}/\tau_{el}} A(t; \tau_{Rn})}{\sum_{n=0}^{N-1} e^{-\tau_{Rn}/\tau_{el}}}, \quad \tau_{Rn} = \tau_{R0} + n\Delta\tau_R. \quad (2.70)$$

In Ref. [67] has been shown that, for photodesorption problems, Gadzuk's "jumping wave packet and weighted average scheme" is equivalent to the exact solution of a two-state Liouville-von Neumann equation with coordinate independent quenching.

Chapter 3

Azobenzenes

3.1 General Properties

Azobenzenes (ABs) are a family of organic compounds consisting of two phenyl rings connected with a N=N double bond, the azo-group. The molecule occurs as *trans* and *cis* conformer (as shown in Fig. 1.1), where the former is energetically more stable than the latter.

Non-substituted *trans*-AB possesses no permanent dipole moment. A finite dipole moment can arise as a consequence of non-symmetric substitution. The *trans* conformer is planar (neglecting the geometry changes that occur due to steric hindrances caused by substitution), even in polar solvents [68]. This isomer has C_{2h} symmetry, see page 141. Contrary to this, the *cis* species are more compact, and three-dimensional, possessing C_2 symmetry. The *cis*-AB has a finite dipole moment $|\mu_{tot}| \approx 3.2$ D [69], oriented perpendicular to the NN moiety.

The coordinates of importance for this work are defined in Fig. 3.1. The dihedral angle connecting the $C_1NNC_{1'}$ atoms, in the central part, is called ω and the angles connecting the NNC_1 and $C_{1'}NN$ atoms, are named α and α' , respectively. Another important degree of freedom is the dihedral angle β , which describes the rotation of the phenyl ring. AB has four such angles, *i.e.*, NNC_1C_2 , NNC_1C_6 , $NNC_{1'}C_{2'}$, and $NNC_{1'}C_{6'}$. In Fig. 3.1, atoms of both benzene rings are numbered as possible

positions for substituents (R).

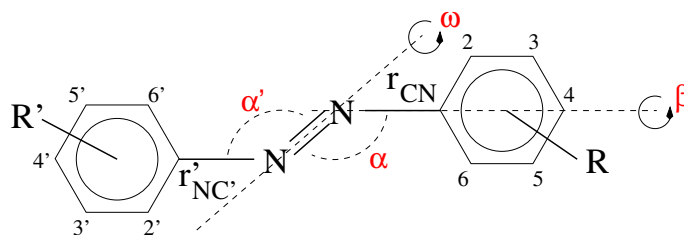


Figure 3.1: Coordinates, bond distances, angles and atom numbering of AB molecules used in this work.

Azo-molecules are usually yellow to red having very characteristic absorption spectra common for all ABs, see Fig. 3.2. Often, photoisomerization processes involve several excited states for the reaction to proceed [70, 71]. In solution, the photoisomerization

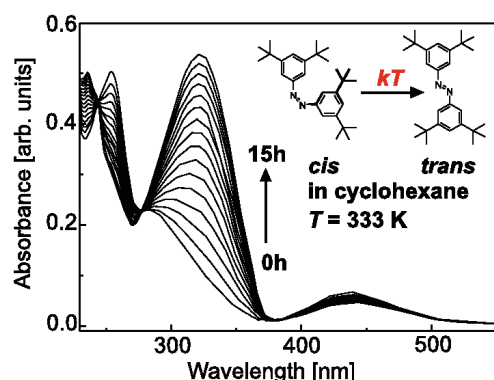


Figure 3.2: UV/Vis spectra of the TBA molecule during thermal *cis*→*trans* isomerization in cyclohexane at 60°C (source: Ref. [18]). The peak at ≈ 320 nm denotes the $\pi \rightarrow \pi^*$ transition in *trans*-TBA; the peak at ≈ 440 nm is the $n \rightarrow \pi^*$ transition in the *cis*-TBA. Their relative weight changes during the isomerization process.

of AB can be explained in a simplified way, involving direct electronic excitation for *trans*→*cis* isomerization at ≈ 320 nm (3.87 eV) and ≈ 440 nm (2.82 eV) for the reverse process, see Figs. 1.1 and 3.2. The former is attributed to the S_2 state ($\pi \rightarrow \pi^*$ excitation), and the latter one to the S_1 state ($n \rightarrow \pi^*$). For ABs in general, these transitions can be found in a wider range which depends on the nature of the substituents in the aromatic residue (Section 5.4). It has been reported [7, 72], that these excitations are rather insensitive to solvent polarity giving spectra which are showing characteristic structure of the absorption bands, accounting only minor shifts of band maxima.

Whether a transition is allowed or forbidden can be easily concluded from values of oscillator strengths given in Table 3.1. Also, electronic transitions are symmetry

dependent which we show in more detail in Appendix B. Because of symmetry, $n \rightarrow \pi^*$ is forbidden for the *trans* isomer¹ but the $\pi \rightarrow \pi^*$ transition is strongly allowed. The latter appears in *cis* spectra too, albeit with weaker intensity. In principle, the *cis* conformer can be reached from two distinct directions: (i) By a rotation path along the dihedral angle ω and (ii) by an inversion path along angle α , see Fig. 3.3, left. These correspond to $S_0 \rightarrow S_2$ ($\pi \rightarrow \pi^*$) and $S_0 \rightarrow S_1$ ($n \rightarrow \pi^*$) transitions, respectively.

That $S_0 \rightarrow S_1/S_2$ excitations can be classified as transitions from one orbital to another, is of course only an idealization. On the B3LYP/6-311G** level of theory, the HOMO of *trans*-AB consists prevalently of the nitrogen lone pairs, while the LUMO is a π^* orbital localized at the azo-moiety with minor contributions from the p_z orbitals in *ortho* and *para* positions. The HOMO-1 is a π orbital. Thus, the $S_0 \rightarrow S_1$ transition can be understood as a HOMO \rightarrow LUMO transition, while the $S_0 \rightarrow S_2$ absorption is basically a HOMO-1 \rightarrow LUMO transition. The corresponding orbital pictures are shown in Fig. 3.3.

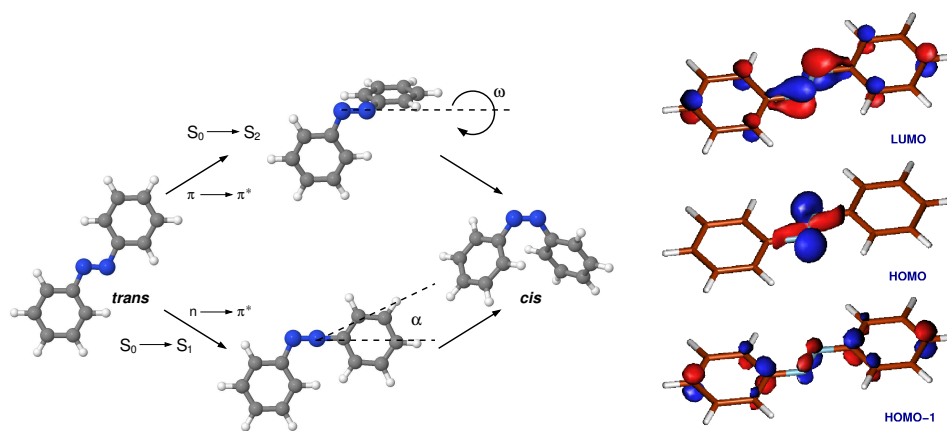


Figure 3.3: On the left panel, the classical view of the AB photoisomerization with two isomerization pathways is given. On the right, the Kohn-Sham B3LYP/6-311G** frontier orbitals of *trans*-AB involved in the photoisomerization are shown: $\pi = \text{HOMO-1}$, $n = \text{HOMO}$ and $\pi^* = \text{LUMO}$.

In reality, selective switching of ABs seems to work in a somewhat more complicated way. In Ref. [70] it has been stressed that interconversional processes like $S_2 \rightarrow S_1$ and $S_1 \rightarrow S_0$ proceed on a sub-ps scale and that some other states, like S_3 and

¹This transition starts to be weakly allowed for molecules with broken symmetry.

S_4 and triplet states, may be involved, too. The S_2 is usually interpreted as an intermediate state, relaxing to the S_1 surface from which the reaction proceeds towards *trans* or *cis* isomers. New mechanisms have been proposed [73] involving simultaneous change of different degrees of freedom. In this way, rotation or inversion as exclusive isomerization pathways for selective excitation are still a matter of debate [73, 74, 75, 76].

3.2 Method Testing

3.2.1 Structures

In Table 3.1, comparisons of geometries and excitation energies obtained with different computational methods or experiments for *cis*- and *trans*-AB are given.

	ω [°]	α [°]	r_{NN} (Å)	r_{CN} (Å)	S_1 (eV)(f)	S_2 (eV)(f)
			<i>cis</i>			
(TD)-B3LYP ^a	9.3	124.2	1.243	1.436	2.55(0.036)	4.14(0.066)
MP2/CCSD [77]	7.3	120.8	1.261	1.432	3.17	4.67
exp.	8.0 ^b	121.9 ^b	1.253 ^b	1.449 ^b	2.92 ^c	4.4 ^d
			<i>trans</i>			
(TD)-B3LYP ^a	180	115.2	1.253	1.418	2.54(0.000)	3.76(0.771)
MP2/CCSD [77]	180	113.7	1.268	1.417	2.95	4.36
CASSCF [70]					3.11	5.56
exp.	180 ^b	113.6 ^b	1.247 ^b	1.428 ^b	2.82 ^c	4.12 ^c

Table 3.1: ^aGeometrical parameters of *cis*- and *trans*-AB are given together with excited state energies at the (TD)-B3LYP/6-311G** level of theory: α and ω are optimized angles, r_{NN} is the NN bond length and r_{CN} is the CN bond length, see Fig. 3.1. The oscillator strengths (f) are given in parentheses. Values are compared to *ab initio* calculations at the MP2/cc-pVTZ level of theory for the ground state geometries [77] and CCSD for excited states [77]. Additionally, CASSCF calculations are reported for the *trans* form in [70]. Experimental values are given for comparison: ^bX-ray measurements [78, 79], ^cgas phase spectroscopy [80] and ^dspectroscopical data in ethanol [81].

Comparing the values of NN and CN bond lengths and α and ω , one can see that they are well reproduced by the B3LYP/6-311G** calculations when compared to WF-based *ab initio* theory and experimental data. In Fig. 3.4, structural parameters of

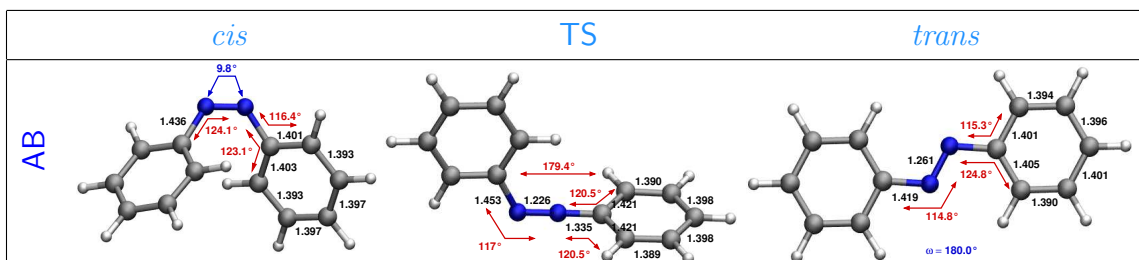


Figure 3.4: Geometries of the AB molecule for stationary points being discussed in this work. The *cis* form isomerizes thermally over the TS to the energetically more stable product, the *trans* isomer. Here, geometry parameters are presented: (i) In blue, ω values, and (ii) in red, angles α . Angles are given in degrees ($^\circ$) and bond distances in \AA . All the presented data are obtained with the B3LYP/6-31G* method and differ slightly from those presented in Ref. [69] and Table 3.1.

stationary points of AB are pictorially given, as obtained on a B3LYP/6-31G* level of theory. For every optimized structure a normal mode analysis was done, which gave only real frequencies for *cis*- and *trans*-AB, and a single imaginary frequency for the transition state (TS) for thermal isomerization (see below).

3.2.2 Excitation Energies

In Table 3.1, excitation energies from S_0 to S_1 and S_2 for AB molecule are also given. In agreement with earlier studies, these are underestimated to about 10% using TD-B3LYP/6-311G** [70, 77]. In the Table we give CCSD and CASSCF excitation energies for comparison. The former were calculated as vertical excitation energies in a small atomic natural orbital (ANO) basis set, at the optimized MP2/cc-pVTZ equilibrium structures [77]. Excitation energies denoted with CASSCF refer to state averaged (SA)(five states) complete active space (CAS) with 10 active electrons in 10 orbitals at the SA-1-CAS(10/10)/6-31G optimized minimum² [70]. It is seen that the CCSD results are slightly more, the SA-CASSCF results clearly less accurate than the B3LYP ones.

In Appendix A (page 133), details about calculated UV/Vis spectra, using different DFT methods and basis sets, of *cis*- and *trans*-TBA molecule are presented. We obtained basis set differences in the order of a few percent. Concerning DFT calcu-

²SA- N -CAS(n/m) refers to a state averaged CASSCF with n electrons and m active orbitals, equally weighting N lowest electronic states.

lations, we were varying either the exchange or the correlation part of a functional or both. Again, the B3LYP functional turned out the most appropriate for absorption spectra calculations. Pure density functionals, like PBE/PBE, appeared to be much too inaccurate for excitation energy calculations.

In Ref. [69], a detailed study of the excited PES, calculated on the TD-B3LYP/6-311G** level, is given (for an AB derivative, di-meta-cyanoazobenzene (DMC)). It has been concluded that the excitation to S_1 can lead to an isomerization for both isomers in a combined motion over α and ω . This state can be reached optically only from the *cis* conformation, but keeping in mind that the PES can distort under the influence of substrate or an STM tip, a non-optical excitation from the *trans* species can also be possible. The topology of S_0 and S_1 surfaces is similar to those computed with CASSCF [82], but some differences occur for S_2 . It may well be that TD-DFT has difficulties to represent this state correctly [76, 83].

3.3 Ground State Potential Energy Surfaces

For studying thermal isomerization process of AB derivatives at surfaces and in solution, the ground state (GS) potential is important and requires detailed discussion. Again, the two degrees of freedom, *rotation* along dihedral angle ω and *inversion* along angle α should be most important for the isomerization process. For all AB-type molecules, the GS PESs have a very similar topology [69]. Possible differences occur in the rotation and/or inversion barrier(s), usually as a consequence of substitution. Here, as an example, the PES of the TBA molecule will be shown, as obtained with B3LYP/6-31G*.

The “relaxed surface” $V(\omega, \alpha)$ of TBA is calculated with a 10° step for ω and a 5° step for α , see Fig. 3.5. For the ground state S_0 , we note minima corresponding to the *cis* ($\omega \approx 10^\circ/170^\circ$ and $\alpha \approx 125^\circ/235^\circ$), and the *trans* isomer ($\omega \approx 180^\circ/0^\circ$ and $\alpha \approx 115^\circ/245^\circ$). “Relaxed surface“ means that all other degrees of freedom were optimized.

In Fig. 3.5 one can see that isomerization in the GS may take place over different paths. These paths were introduced “by hand”. Path **1** describes simply the change

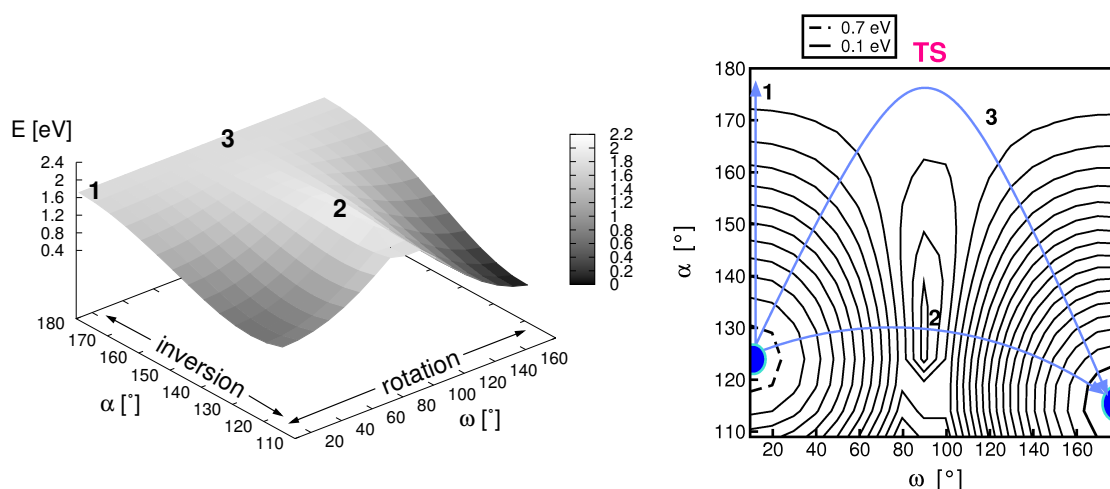


Figure 3.5: On the left hand side, the calculated fully relaxed PES of the TBA molecule obtained with B3LYP/6-31G* is shown. The rotational path, over ω , was calculated with a 10° step while a 5° step was chosen to cover the inversion path over angle α ; 270 points were calculated in total. On the right, contour plots with a 0.10 eV separation and possible isomerization paths in the GS are presented. The energies are given relative to the *trans* minimum, which is located at $\omega = 180^\circ$ and $\alpha \approx 115^\circ$. "TS" indicates the transition state for thermal isomerization.

of angle α , *i.e.*, the *inversion* process, with the following values for the barriers: 1.11 eV for the *cis*→*trans* reaction, and nearly 1.76 eV for the back reaction. In path **2**, a change of dihedral angle ω over the maximum on the PES takes place, which gives *rotation* barriers of around 1.40 eV for the *cis*→*trans* reaction and 2.06 eV in the opposite direction, *i.e.*, much higher when compared to inversion. If one assumes that the relative barrier heights are correct, this result obviously favors the inversion process. Also, in path **2** a slight change of angle α needs to be stressed because its equilibrium value differs for two conformers, *cis* and *trans*. In fact, this process can be classified as concerted because of simultaneous change of the two angles α (α').

Similarly, path **3** supports a concerted mechanism, running through a barrier of about 1.11 eV for the *cis*→*trans* switch. In pathways **1** and **3**, we can see that at one point the angle α becomes almost linear. Note that the energy does not change at $\alpha = 180^\circ$ if one varies the dihedral angle ω . Concerning the barriers alone, one can conclude that paths **1** and **3** are favored for the GS thermal isomerization, compared to **2** for which only rotation of the molecule is taken into account. According to a well established model by Talaty and Fargo [84], the TS reaches a *linear* geometry before becoming a *trans* conformer, which fits to the description of path **3**. In Chapter 5,

TSs will be optimized with the finding that they lie at the position where the α angle reaches the value of $\approx 180^\circ$, and $\omega \approx 90^\circ$, as shown in the central part of Fig. 3.4. We will see that the precise geometry of the TS varies somewhat from molecule to molecule. In Section 5.5 it will be also shown that isomerization over α is not always equivalent to the reaction over α' in the case of non-symmetric PESs due to substitution.

According to Ref. [70], a conical intersection (CI) to the S_1 state exists at $\omega \approx 90^\circ$, leaving traces on the S_0 surface, too. On S_0 , the barrier in the region of $\omega \approx 90^\circ$ and $\alpha \approx 120^\circ$ has a value of ≈ 1.80 eV starting from *trans*. This area looks rather non-smooth. We attribute this to the single determinant treatment, which fails in the region of the barrier for the purely rotational path, along ω . Therefore, barriers calculated along path **2** are highly questionable, but the statement that this path is energetically demanding remains true.

3.4 Anionic and Cationic Azobenzenes

3.4.1 Experimental Observations

As we just saw in Section 3.3, that the ground state is important for studying thermal isomerization dynamics of AB and its derivatives. For exploring photochemical behavior of these species in gas phase or in a solution, excited singlet or even triplet states are important, see Section 3.2. In the experiments performed at surfaces, studying *trans* \rightarrow *cis* isomerization, the situation can be different due to the fact that the processes at surfaces are usually substrate mediated, and hot electrons or holes can attach to the adsorbate forming short-lived anion or cation resonances.

In STM experiments, there are various mechanisms which can enforce reaction: (*i*) By “above threshold excitation” of an adsorbate with single electrons or holes, (*ii*) by inelastic electron tunneling (IET), or (*iii*) by field effects. The first two are resonant processes, with reaction yields that depend linearly or non-linearly on the tunneling current, respectively. The latter process is also operative in the zero-current limit and will be the matter of topic in Chapter 4. In resonant cases, for example, anions

and cations can be used as intermediate species depending on whether the bias voltage is positive or negative.

Ionic resonances can also play a role in photon-induced reactions at metal surfaces. For example, for the switching of *trans*-TBA on Au(111) [14, 17, 85, 86], a new mechanism was proposed explaining the isomerization process as a hole-induced (positive ion resonance) mechanism. During the experiment, different photon energies were applied, providing the access to the LUMO of both, *trans* and *cis* isomers. In general, 2PPE is a powerful tool for investigation of both occupied and unoccupied electronic states of adsorbed molecules. Hot hole induced processes are well-known from the photochemistry of adsorbates at semiconductor surfaces, see Ref. [14] and references therein.

As a consequence of these experimental findings we will study anionic and cationic species of AB and its derivatives, as possible intermediate states at surfaces. Here, we also note that the back reaction, *cis*→*trans*, of TBA on gold is thermally induced at the surface. There is only one example where this reaction was successfully photo-induced [13].

3.4.2 Anionic Species

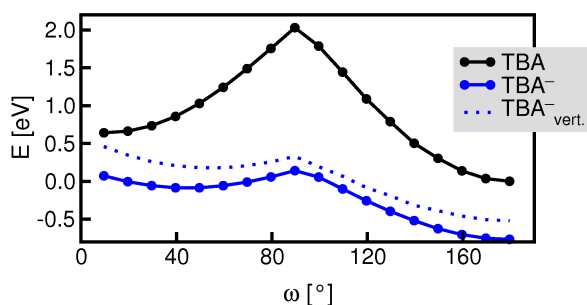


Figure 3.6: Potential energy curves of TBA and TBA^- along ω , calculated using B3LYP/6-31G*. Solid lines represent fully relaxed paths for given species, while the dotted lines, correspond to vertical excitations describing sudden attachment/detachment processes.

To investigate the role of ionic species as possible intermediates, we calculated relaxed potential energy curves along ω for the neutral and negatively charged TBA molecule, see Fig. 3.6. The black curve is for the neutral TBA, while two anion paths are given in blue. Relative to the energy of *trans*-TBA, the solid blue line shows a *relaxed* path, where all the points along the neutral curve were reoptimized for the anion, TBA^- . If, instead, the energy of the anion is cal-

culated in the geometry of the neutral molecule, we have a *vertical* path ($\text{TBA}_{\text{vert.}}^-$), given as a dotted blue line in Fig. 3.6. The latter one is important for sudden attachment/detachment processes.

We first of all note that the neutral $V(\omega)$ curve roughly resembles the reaction path **2** in Fig. 3.5, with a high (and probably due to neglected multi-determinant effects somewhat unreliable) barrier around $\omega \approx 90^\circ$. Secondly, we see that due to the positive electron affinity (EA) of TBA the anions are lower in energy. However, this order can change at a surface because one needs to add the work function of the surface or the tip, Φ , and correct for image charge stabilization (ICS) of the anion, Δ_{im} , one roughly has [69]:

$$V_{A^-}(\omega) - V_A(\omega) = -\text{EA}(\omega) + \Phi + \Delta_{im}. \quad (3.1)$$

The ICS is calculated as

$$\Delta_{im} \approx -\frac{e^2}{4Z} \quad (3.2)$$

with e , the electron charge, and Z , the distance between anion and the image plane. Using the ΔSCF (ΔDFT) method, the electron affinity can be calculated as

$$\text{EA} = E(A) - E(A^-) \quad (3.3)$$

where $E(A)$ is the total energy of the neutral molecule, and $E(A^-)$ that of the anion. Neglecting the orbital relaxation, EA can also be calculated using Koopmans' theorem

$$\text{EA} = -\varepsilon_{LUMO} \quad (3.4)$$

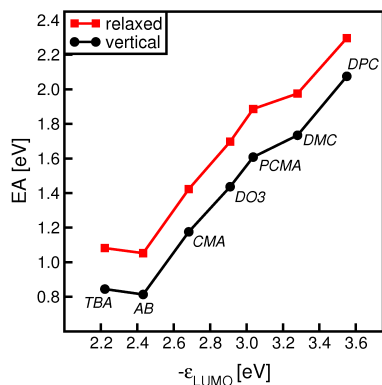


Figure 3.7: Presented are the computed vertical and relaxed electron affinities (EA) for various *trans*-ABs, given in Table 3.2, in correlation with ε_{LUMO} . All values are calculated with the B3LYP/6-311G** method.

i.e., from the LUMO orbital energy. Even though Koopmans' theorem is not strictly valid for Kohn-Sham orbitals [87], we plot EA as calculated from Eq.(3.3) vs. $-\varepsilon_{LUMO}$ in Fig. 3.7 for various *trans*-ABs given in Table 3.2. All values are calculated on the B3LYP/6-311G** level of theory.

Fig. 3.7 shows that indeed a quasi-linear relation exists between (3.3) and (3.4). The two curves in the graph refer to ΔDFT values calculated for relaxed and vertical anion geometries, respectively. As expected, the lowest values for EA are found for alkyl substituted molecules, like TBA, and the highest for electron acceptor substitution. The position of an extra group plays an important role (see the comparisons between DMC and DPC, and CMA and PCMA), leading to affinities which are 0.50 eV higher in *para* than those in *meta* position.

molecule		$ \mu $ [D]	$-\varepsilon_{LUMO}$ [eV]	EA [eV]	EA _v [eV]
TBA	cis	3.600			
	trans	0.001	2.22	1.08	0.84
AB	cis	3.211			
	trans	0.000	2.43	1.05	0.81
CMA	cis	3.210			
	trans(-c)	3.009	2.68	1.42	1.18
DO3	cis	7.541			
	trans	9.870	2.91	1.70	1.44
PCMA	cis	3.240			
	trans	0.000	3.04	1.89	1.61
DMC	cis	6.983			
	trans(-t)	0.000	3.28	1.98	1.73

Table 3.2: AB derivatives investigated in this work and in Ref. [69]. Shown are optimized geometries for *trans* species, permanent dipole moments and the computed electron affinities (see text), using B3LYP/6-311G**. The DPC molecule is not shown here.

This can be explained by the fact that the LUMO has a nonvanishing contribution in *para* and a node in *meta* positions, see Fig 3.3. In this way, level tuning is possible via substitution, which is most efficient with electron acceptors in *ortho* and *para*

positions. Further effects induced by substitution will be discussed in Chapter 5.

Considering the STM experiments, at a positive sample bias, where the switching (and desorption) of the DMC and CMA molecules on Au(111) were observed [19, 88], we will interpret the results with the help of Eq.(3.1). The switching was induced, presumably from *trans*, at a voltage threshold of 1.7 eV for DMC, and around 2.3 eV for the CMA molecule, over the "negative ion resonance".

At first we make an estimate for Φ , taking the work function of gold of ≈ 4.6 eV. The value of Δ_{im} (Eq.(3.2)) is ≈ 1.2 eV if the anion-image plane distance, Z , is 3 Å (this distance is not precisely known). Taking the values for vertical excitation energies (EA) we obtain, for DMC/Au, an excitation energy at the surface of $V_{A^-}(\omega) - V_A(\omega) \approx (-1.7 + 4.6 - 1.2)$ eV ≈ 1.7 eV. Similar, for CMA/Au, the excitation energy is estimated by the same token as $(-1.2 + 4.6 - 1.2)$ eV ≈ 2.2 eV. All these values correspond nicely to the threshold voltages found in experiments. Most importantly, the threshold difference between DMC and CMA of ≈ 0.6 eV can be traced back to the difference in EA of the two molecules, supporting the hypothesis of a negative ion intermediate.

However, one should note that for the case of DMC molecule, there are indications that another degree of freedom can be important for conformational changes at the surface, namely, the rotation of the phenyl ring. This will be studied in more detail in Chapter 4.

Finally, a few words need to be said about geometries and reaction barriers of anionic ABs. The optimized anion molecules show noticeable structural changes. The NN bond appears to be elongated for anions by ≈ 0.07 Å for *trans*-AB and ≈ 0.09 Å for *cis*. The reason is that the LUMO of the neutral AB, being NN antibonding, is occupied in the anion, see Fig. 3.3. The dihedral angle ω changes as well, from $\approx 9^\circ$ to $\approx 46^\circ$ in the *cis* form, while angle α remains almost unaffected. The strong geometry change in ω is also visible from Fig. 3.6. The CN bond shortens by ≈ 0.05 Å for the *trans* and ≈ 0.07 Å for the *cis*-AB, since the LUMO of the neutral molecule is CN bonding.

Due to an electron attachment the molecule would tend to rotate far more easily over ω which is also seen in Fig. 3.6. The rotation paths, drawn in full lines, are

connecting completely reoptimized points for a given specie. Neutral TBA has a barrier of 2.03 eV, starting from *trans*, or 1.39 eV from *cis*. For the anion path, the *trans* species are most stable at $\approx 180^\circ$ but the minimum *cis* geometry changes to $\approx 40^\circ$. The barrier is at 90° and, for the relaxed case, 0.91 eV going from *trans*, and reducing to only 0.29 eV from the *cis* direction. For the vertical case, the barriers are even lower. Thus, even if the reaction may proceed along other pathways and even if the anionic state may be short-lived at the surface, this analysis shows that a combination of structural distortions and barrier reduction upon electron attachment will likely increase the switching probability of ABs.

3.4.3 Cationic Species

Similar to the anionic ABs, excitation energies for "positive ion resonances" can be estimated from the following expression

$$V_{A^+}(\omega) - V_A(\omega) = \text{IP}(\omega) - \Phi + \Delta_{im}. \quad (3.5)$$

Here, IP is the *ionization potential* of the molecule, which can be calculated from the ΔSCF (ΔDFT) method as

$$\text{IP} = E(A^+) - E(A) \quad (3.6)$$

with $E(A^+)$ as the total energy of the cation. Applying Koopmans' theorem the ionization potential can be alternatively calculated as

$$\text{IP}_n = -\varepsilon_n \quad (3.7)$$

where ε_n is the energy of n -th occupied orbital, and IP_n is the n -th ionization potential. The lowest IP is for the ionization of the HOMO. The ΔSCF method (Eq.(3.6)) gives always the lowest cation.

First, we discuss the rotation paths given in Fig. 3.8 (left), where Eq.(3.6) has been used. For the relaxed cation curve (solid red line) we see minima at $\approx 150^\circ$ (*trans*), and at $\approx 40^\circ$ (*cis*). In comparison to anionic curves, here we find changes in dihedral angle ω for both *cis* and *trans*. For the relaxed cation case, the barrier height reduces to 0.53 eV from the *trans* direction and to 0.18 eV from the *cis*. For the vertical

potential energy curve (dotted red line in Fig. 3.8, left), a very similar behavior is found, with barriers of 0.51 eV and 0.14 eV, respectively. We conclude that also a positive ion resonance can enhance the reactivity towards isomerization.

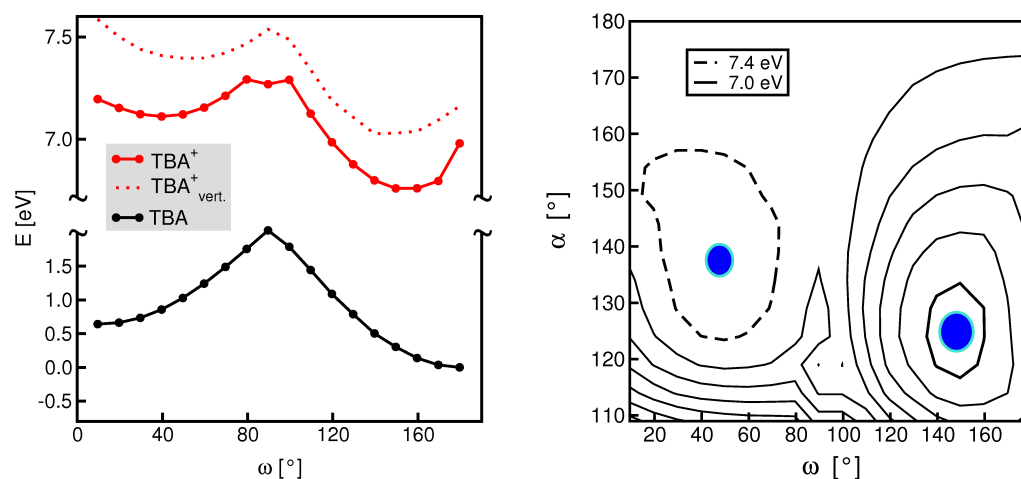


Figure 3.8: On the left, potential energy curves of TBA⁺ along ω are shown when calculated using B3LYP/6-31G*. Solid lines describe relaxed and dotted ones vertical potential curves. In black, the rotation in the ground state is shown for comparison. On the right, we show the vertically ionized cationic surface of TBA⁺_{vert.}, where we calculated 15 points in α in the range between [110°,179°] times 18 points in ω between [10°,180°]. The contours are separated by 0.10 eV and all energies are given relative to the fully optimized *trans*-TBA.

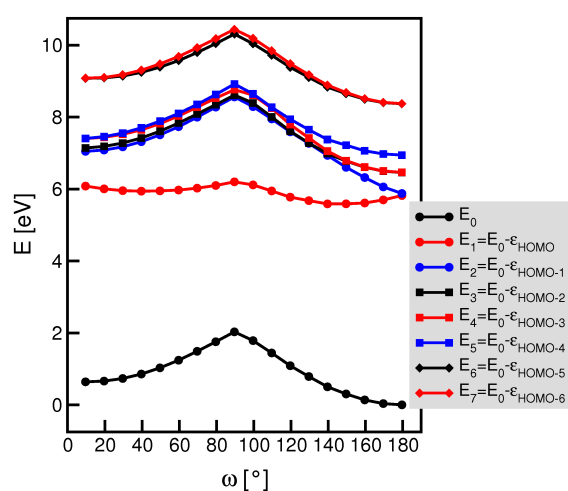


Figure 3.9: Koopmans' theorem is used to calculate various cationic potential energy curves for TBA, with E_0 denoting the neutral state.

In Fig. 3.8 (right), we show the vertical PES $V(\alpha, \omega)$ of TBA⁺_{vert.} which demonstrates that not only along the ω path the reaction is facilitated, but also along the inversion pathway. The figure also demonstrates that minima are shifted relative to the neutral case. The fully optimized *trans*-TBA⁺ has an $\approx 15^\circ$ larger α value than in the neutral molecule, and *cis*-TBA⁺ has an α which is $\approx 13^\circ$ larger.

In a second step Koopmans' theorem was applied, first to compare the lowest cation state with ΔSCF , but also to

get information for higher excited cation states, see Fig. 3.9. One can see that the ionization out of the HOMO gives a barrier from the *cis* side of ≈ 0.12 eV, which is similar to the $\text{TBA}_{\text{vert.}}^+$ case. For the *trans* \rightarrow *cis* transition, the molecule would need to overcome a barrier of ≈ 0.4 eV. Koopmans' theorem gives a good prediction of minima as well, which are located at $\approx 40^\circ$ and 140° , for *cis* and *trans*, respectively. Higher excited cation states, where electrons have been removed from the HOMO-1, HOMO-2, etc., seem to be not well suited for switching because the barriers are high and the shape of the potentials is close to the ground state one.

Chapter 4

Azobenzenes in External Electric Fields

4.1 Experimental Observations

Recent STM experiments on ABs at metal surfaces for which a possible role of static field effects has been proposed, will be discussed here. In a first experiment, using an STM and holding the tip high above the adsorbed islands of TBA molecules, some of the species were switched reversibly on Au(111) [11]. Positioning the tip at $\approx 5 \text{ \AA}$ or more above the sample and applying a bias voltage between the STM tip and the sample, a static electric field is formed which can be used to manipulate adsorbates at surfaces. In the following, the field is idealised as homogeneous, because of the unknown atomic structure of the tip itself. The fact that field effects may play a big role here, comes from the observation that this kind of manipulation is operative even in the limit of zero tunneling current [89]. In the case of TBA at Au(111), long ($t = 20 \text{ s}$) voltage pulses at a bias voltage of 2 V and a tip height of 6 \AA lead to the switching of molecules, from the *trans* to the *cis* form. After employing shorter pulses ($t = 5 \text{ s}$), on a single molecule though, and a bias voltage of 1.5 V for a tip height of 5 \AA , the conformation changed back to *trans*.

The second example is the investigation of 3,3'-dicyanoazobenzene (or shortly DMC) adsorbed at Au(111), where rotation of a single phenyl ring has been

achieved [19]. Since the rotation of the phenyl ring cannot be explained only through the formation of the “negative ion resonance“ (see below), probably also static field effects due to the STM tip need to be taken into account. The molecule itself has two cyano groups (CN) placed in *meta* positions of each phenyl rings (Fig. 4.1). Cyano groups are highly electrophilic, which may lead to the stabilization of the planar adsorption configuration of the molecule at the substrate. On the other hand, general properties of the AB molecule (structure and

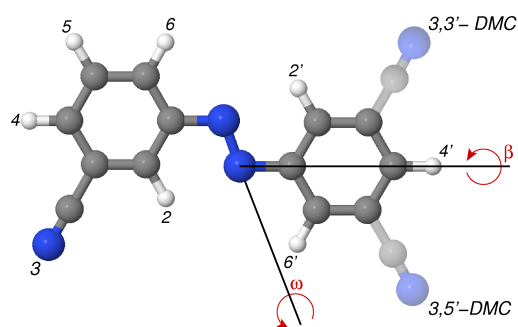


Figure 4.1: Pictorial representation and atom numbering of the DMC molecule is given together with the definition of the dihedral angles β and ω . The structural difference between 3,3'- and 3,5'-DMC is indicated, too.

electronic configuration) [69, 90, 91] do probably not significantly change upon adsorption. The functionalization with cyano groups allows also easier identification of distinct isomers on the surface. Specifically, the rotation around the dihedral angle β , which is defined between the two nitrogens and the two nearest carbon atoms of a phenyl ring, changes the isomer from the 3,3'- to the 3,5'-DMC form. As already said, four such angles can be defined, see Figs. 3.1 and 4.1. Experimentally, one cannot distinguish neither between 3,5' and 5,3', nor between 3,3' and 5,5' *trans* iso-

mers. This kind of rotational isomerization is usually ignored in the gas phase because of a very small energy barrier, but starts to be important when this sort of movement becomes frustrated, by adsorption at surfaces, for example. In contrast to rotation, the *trans*→*cis* switching for the DMC/Au(111) was not successful in Ref. [19].

4.2 Field Effects on TBA

If we start from the premise that the static field plays an important role in the STM switching of the TBA molecule, several assumptions have been made [69, 92]. First, we assume that TBA is only physisorbed and thus, the geometry and electronic structure of the gas phase molecule is only little affected. Second, the

field will distort the ground state potential leading to new reaction possibilities and changing the energy barriers, *e.g.*, for *trans*→*cis* isomerization in the ground state. Assuming that the external electric field F_z is homogeneous and oriented along the axis perpendicular to the surface, a molecule is then exposed to an effective potential, along a set of nuclear coordinates, Q :

$$V(Q) = V_0(Q) - \mu_z(Q)F_z - \frac{1}{2}\alpha_{zz}(Q)F_z^2. \quad (4.1)$$

V_0 is a field-free ground state potential, μ_z is the z component of the permanent dipole moment and α_{zz} the zz component of the polarizability tensor, which gives rise to an induced dipole moment.

First of all, some assumptions need to be made not knowing the relative orientation of the TBA molecule adsorbed at the surface towards the tip. It is reasonable to assume that the *trans*-TBA lies flat on the surface (NN axis and phenyls are parallel to it). The *trans*-TBA has no dipole moment (see Table 3.2), which we assume to be the case also in the adsorbed state. For the *cis*-TBA, we propose two models: (*i*) In model A, both permanent and induced dipole moments are oriented perpendicular to the surface, *i.e.*, aligned with the field (see inset of Fig. 4.2A), and (*ii*) model B, where we assume that the permanent dipole moment is parallel to the surface, while the induced one has a perpendicular component (see inset of Fig. 4.2B). Within both models, Eq.(4.1) gives energy shifts for *cis* and *trans* forms relative to the field-free case of

$$\Delta V(\text{cis}) = -\mu_c F_z - \frac{\alpha_c}{2} F_z^2 \quad (4.2)$$

$$\Delta V(\text{trans}) = -\frac{\alpha_t}{2} F_z^2. \quad (4.3)$$

In Eq.(4.2), μ_c is the permanent dipole moment perpendicular to the surface. The indices "c" and "t" denote the properties of the *cis* and *trans* forms.

In model A (for $F_z > 0$, *i.e.*, positive sample bias), the field is parallel to μ_c , thus stabilizing the *cis* isomer. Moreover, α_c is the relevant matrix element of the polarizability tensor, *i.e.*, $\alpha_c = \alpha_{\perp,c}$ ($\alpha_{\perp,c}$ is the zz -element of the diagonalized polarizability tensor, see below).

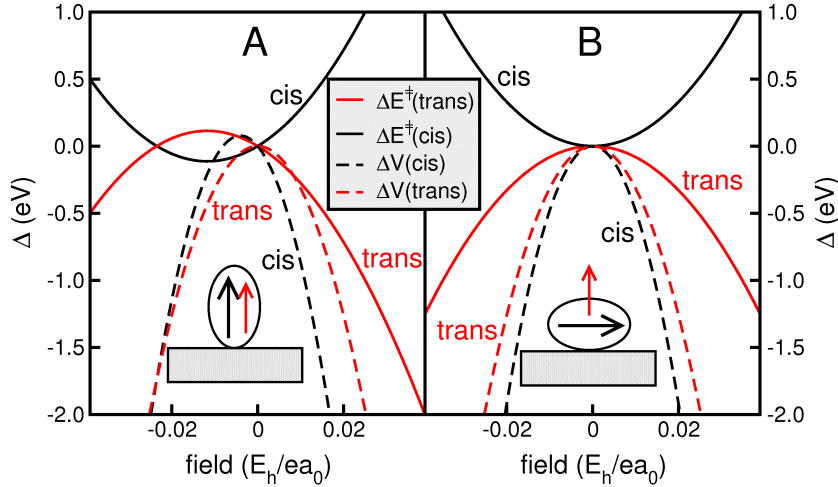


Figure 4.2: $\Delta V(\text{cis})$ and $\Delta V(\text{trans})$ (dashed lines) and $\Delta E^\ddagger(\text{cis})$ and $\Delta E^\ddagger(\text{trans})$ values (solid lines) calculated for the TBA molecule within models A and B. As an inset, for the *cis* form, the orientation of the permanent (thick arrow) and the induced dipole moment (thinner arrow) relative to the surface is given (see text). The energies are given in eV, and the field strength is given in atomic units ($0.01 E_h/ea_0$ corresponds to 0.51 V/\AA).

In model B, $\mu_c = 0$ and $\alpha_c = \alpha_{\parallel,c}$, with $\alpha_{\parallel,c}$ being the component of the polarizability tensor creating an induced dipole perpendicular to the surface but parallel to the NN axis. We estimate the value of $\alpha_{\parallel,c}$ by diagonalizing the polarizability tensor and defining

$$\alpha_{\parallel} = \frac{1}{2}(\alpha_{xx} + \alpha_{yy}). \quad (4.4)$$

trans		cis	
α_{\parallel}	α_{\perp}	α_{\parallel}	α_{\perp}
455.5	231.4	352.5	300.1
	$=\alpha_t$	$=\alpha_c$ in A	$=\alpha_c$ in B

Table 4.1: Polarizabilities of the TBA molecule perpendicular and parallel to the NN axis (defined in the text). Values are given in atomic units, calculated with B3LYP/6-31G*.

Finally, in Eq.(4.3), α_t is the zz -component of the polarizability tensor of the *trans* form which is assumed to be flat at the surface, *i.e.* $\alpha_t = \alpha_{\perp,t}$. Various contributions for the TBA, calculated using B3LYP/6-31G* for the gase phase molecule are given in Table 4.1.

The *trans*-TBA has a larger polarizability parallel to the NN axis and benzene rings, compared to the perpendicular component. Contrary, the *cis* isomer has α_{\parallel} and α_{\perp}

similar to each other, which is mostly a consequence of its more globular geometry. Both values are larger than α_{\perp} of the *trans* form, which implies that the *cis*-TBA can be stabilized by vertical polarization to a larger extent than the *trans* form, in both models. The *cis*-TBA can also be destabilized if in model A the μ_c is antiparallel to the external field. This is illustrated in Fig. 4.2, where $\Delta V(\text{cis})$ and $\Delta V(\text{trans})$ are shown, for various field strengths, as dashed lines.

For estimating activation energies in the presence of a field, we assume that μ_c and α_{zz} change linearly along a one-dimensional reaction path with a transition state that lies exactly halfway along this path. Then, the barrier shifts in energy by $[\Delta V(\text{trans}) - \Delta V(\text{cis})]/2$, and the barrier heights are determined according to

$$\Delta E^{\ddagger}(\text{cis}) = \frac{\Delta V(\text{trans}) - \Delta V(\text{cis})}{2} = -\Delta E^{\ddagger}(\text{trans}). \quad (4.5)$$

In Fig. 4.2, $\Delta E^{\ddagger}(\text{cis})$ and $\Delta E^{\ddagger}(\text{trans})$ are shown as solid lines. In model B, the barrier for the *trans*→*cis* process is always lowered, while the *cis*→*trans* isomerization requires more energy than in the field-free case. In contrast in model A, the *trans*→*cis* can also be hindered ($\Delta E^{\ddagger}(\text{trans}) > 0$) and the reverse one favored ($\Delta E^{\ddagger}(\text{cis}) < 0$), when the permanent dipole is antiparallel to the field ($F_z < 0$).

Finally, a connection to experiment should be made, where the isomerization of the TBA was observed at positive and negative bias [11]. For the *trans*→*cis* process some asymmetry has been observed, where one needs larger absolute voltages to switch the molecule at negative voltages than at positive ones. This is consistent with our model A, if the permanent dipole moment of the *cis* form is oriented such that it is destabilized. For the reverse *cis*→*trans* process such asymmetry is not observed (thus favoring model B), pointing to the fact that it is quite unlikely that a pure field effect is at work. The latter statement is supported by the fact that very large field strengths would be required according to theory. It was found that at field strengths around $0.5 \text{ V}/\text{\AA} \approx 0.01 E_h/ea_0$, the barrier would change by about 0.25 eV at most, which is much smaller than the field-free barrier of more than 1 eV (see Section 3.3). This implies that a field larger by a factor of 3 is needed to switch the molecule. On the other hand, both permanent dipole moment and the polarizability can be enhanced at the surface, and details of the molecular orientation as well as

the exact variation of these quantities along the (unknown) reaction path were not included in our model.

4.3 Field Effects on DMC

We will now study the role of field effects during the STM-induced β rotation of DMC on Au(111). Since here a clear positive voltage threshold exists (page 39), we assume that a negative-ion resonance mechanism is operative. We suggest, however, that the latter must be supported by an external electric field. For this purpose, DFT calculations on the B3LYP/6-31G* level of theory are carried out for the free molecule.

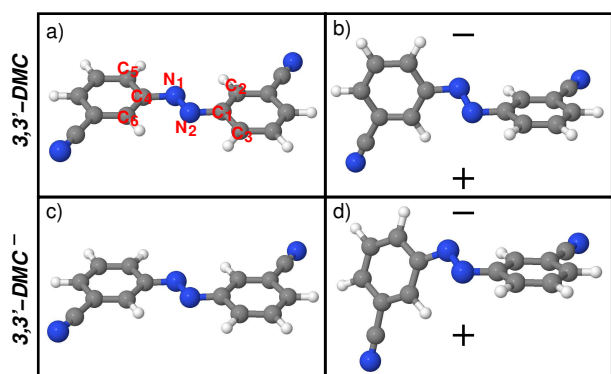


Figure 4.3: Optimized structures of the 3,3'-DMC molecule: upper part, neutral molecule without a) and with the field b), and lower part, anion without c) and with the field d). In (b,d), an electric field is oriented perpendicular to the right N-Ph-CN moiety (which is assumed to be parallel to the substrate's surface plane). The field is oriented from “+“, the surface, towards the “-“, the STM tip. In a) atoms are labeled in order to recognize the four different β angles for the “field on“ case; the angles are connecting N₁-N₂ with C₄-C₅ and C₄-C₆ on one, and with C₁-C₂ and C₁-C₃ on the other side.

In Fig. 4.1 one can see the change of the 3,3' arrangement of the DMC molecule to 3,5'. The former structure is energetically more favorable than the latter one, by ≈ 0.01 eV, because of the cyano groups on opposite sites. Assuming that the 3,3' \rightarrow 3,5' isomerization process at Au(111) surface runs due to sudden attachment/detachment of a single electron, *i.e.*, over vertical excitation from the ground to the anion state of DMC, we will concentrate the study on these two states. In the field-free case, fully optimized *trans*-3,3' structures of neutral and anionic species are, from the geometrical point of view, very similar (see Fig. 4.3, a) and c)). The largest difference, upon electron attachment, occurs in the central moiety. Namely, NN has a bond-

ing and NC an antibonding character in the LUMO (for neutral DMC, see also Fig. 3.3 (right)). In the anion DMC^- , the N=N bond is then elongated by $\approx 0.07 \text{ \AA}$, and the NC bond shrinks by about 0.05 \AA . None of these modes would rotate one of the phenyl rings, if excited.

As other possible reactive coordinates, we consider the β and ω dihedral angles as defined in Fig. 4.1. The process of sudden attachment/detachment of an electron is illustrated in Fig. 4.4, where calculated 2D potential energy surfaces $V(\beta, \omega)$, are shown. Specifically, assuming that all other degrees of freedom don't change much during the process or are dynamically inactive, the dihedral angles β , connecting $\text{N}_1\text{-N}_2\text{-C}_1\text{-C}_2$ and ω , connecting $\text{C}_4\text{-N}_1\text{-N}_2\text{-C}_1$ were considered (see Fig. 4.3 for atom numbering). For this two-dimensional model, β was varied in the interval of $[0^\circ, 360^\circ]$ and ω in the interval $[130^\circ, 230^\circ]$. All other coordinates were fixed at values obtained from the full geometry optimization of the neutral 3,3'-DMC. Precisely the same, restricted geometries were then used for three other PES, namely the anion DMC^- in absence of the field c), and DMC and DMC^- in an external electric field, b) and d), respectively (see Fig. 4.4). In the "field-on" cases, we suppose that the electric field is oriented perpendicular to one half of the molecule, namely, the right N-Ph-CN unit in Fig. 4.3. This part of the molecule was enforced to stay flat in a plane (assumed to be parallel to the substrate's surface), while the other half of the molecule was free to move along β and ω modes. We applied a field strength of $F = 0.4 \text{ V/\AA}$ (or $0.0078 E_h/ea_0$) directed from the surface (+) to the tip (-). The field orientation is consistent with experiment while its strength is probably somewhat too large.

From Fig. 4.4 a) for neutral DMC without an electric field, one finds minima at $\beta=0^\circ$, $\omega=180^\circ$ and at $\beta=180^\circ$, $\omega=180^\circ$ that correspond to the 3,3' and 3,5' conformations, respectively. The former minimum is slightly lower than the other one, because the CN groups are found on opposite sides. This finding agrees with the fully optimized geometries, see Fig. 4.3. The two structures are separated by a barrier of 0.3 eV at $\beta=90^\circ$, $\omega=180^\circ$. Due to symmetry, an equivalent barrier exists for $\beta=270^\circ$. We note that from a one-dimensional model, from $V(\beta)$ curve (not shown) with fully relaxed, other internal coordinates, a barrier of 0.27 eV is found, in reasonable agreement with the 2D model.

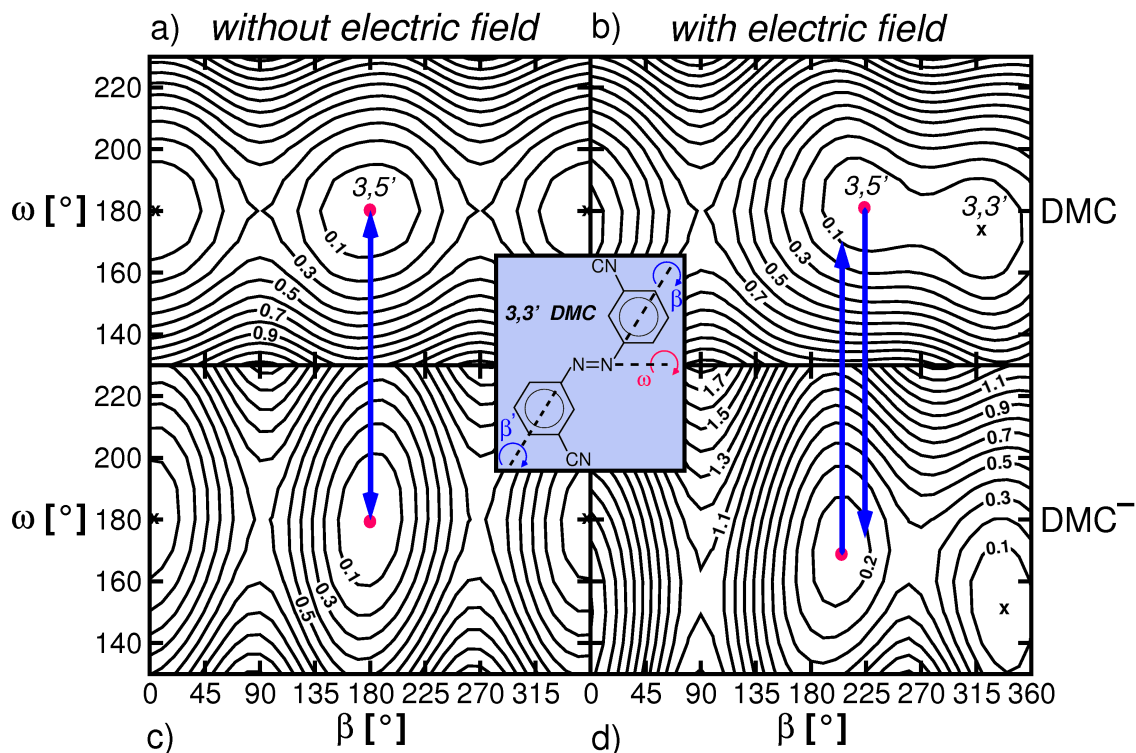


Figure 4.4: Contour plots of the PES $V(\beta, \alpha)$ for DMC a) without and b) with the field and for DMC⁻ c) without and d) with the field. Contours are separated by 0.10 eV, starting from the minima which are labeled with red dots. Moreover, some contours are additionally labeled for easier orientation. The inset, with the key coordinates, is shown again for clarity. The arrows connect minima and represent processes of sudden, vertical electron attachment/detachment. In the field free case, 3,5' minima, for the DMC and DMC⁻ are at the same positions, which means that almost no energy is gained due to the electron attachment (a→c), or detachment (c→a). In the field on case, by sudden attachment (b→d) or detachment (d→b), energy can be gained to overcome the barrier toward the 3,3' in b).

Looking at the field-free DMC⁻ surface c), the minima are at the same positions as for the neutral DMC, again in agreement with the fully relaxed species (Fig. 4.3). The major effect one can see is the increase of the barrier to 0.61 eV. The barrier in 1D is 0.57 eV and therefore similar to the 2D model. The increased barrier occurs because of the LUMO being bonding between the N and the C atom (both N₁-C₄ and N₂-C₁, see Fig. 3.3), *i.e.* attaching an electron to this orbital will hinder rotation. In the end one can see that the topography of both DMC and DMC⁻ surfaces without the field is very much the same, noticing that only a change in the barrier occurs. We can conclude that no torsion in β is created, and that due to the

electron attachment/detachment process, the molecule will not rotate and remain ideally flat, as seen from the geometries of DMC and DMC^- in Fig. 4.3.

The situation changes completely in the presence of the external electric field, which is expected to distort the potentials. To demonstrate the effect, $V(\beta, \omega)$ is calculated for DMC and DMC^- molecules in the presence of a field (Fig. 4.4, b) and d)). Describing the neutral DMC first, the 3,3' minimum shifts by $\sim -40^\circ$ in β and $\sim -10^\circ$ in ω , giving new equilibrium values of $\beta=320^\circ$, $\omega=170^\circ$. Likewise, the 3,5' minimum shifts by $\sim +40^\circ$ along β and is now placed at $\beta=220^\circ$, $\omega=175^\circ$. In the fully optimized case, Fig. 4.3 b), where one N-Ph-CN unit was forced to remain flat and parallel to the substrate, DMC has a more compact shape, orienting the phenyl ring with the CN group towards the "surface" (away from the "tip") in order to minimize the energy of the system. In that way, the Coulomb interaction between the ring and the "positive surface" is maximized. From Fig. 4.4 b), one can see that the two transition states, at $\beta \approx 90^\circ$ and $\beta \approx 270^\circ$ become inequivalent. The barrier at $\beta \approx 90^\circ$ is about 0.7 eV and hence higher than for the field free case. The other barrier, at $\beta \approx 270^\circ$ lowers to less than 0.1 eV. This is due, as explained in the case of fully optimized species in an electric field, to the rotation of the phenyl ring in the direction of the "tip" in the former case, and for the latter case, to the ring movement to the "positive surface". This situation has been also found in 1D where the lower barrier was 0.15 eV and the higher one 0.8 eV.

In panel d) of Fig. 4.4, we see the PES of DMC^- in the electric field. When compared to the PES of DMC^- without field, the topography is now very different, and there are differences compared to the neutral DMC in the electric field as well. The two minima are located at $\beta=340^\circ$, $\omega=150^\circ$ and $\beta=200^\circ$, $\omega=170^\circ$. A larger barrier of 1.1 eV is, as formerly seen at $\beta \approx 90^\circ$ and a lower one of 0.37 eV at $\beta \approx 260^\circ$. Due to the fact that the minima are shifted compared to the minima of the neutral DMC in the electric field, an electron attachment can induce a coupled motion along β and ω . In particular, the ω shift is much larger for the anion state, making the anion DMC more "three-dimensional" than the neutral form. Detachment of an electron (the blue arrows indicate vertical attachments/detachments in Fig. 4.4), will bring the system back to the neutral DMC, where additional kinetic energy can be gained.

The upper bound of the energy gain by attachment and subsequent detachment can

be estimated with the help of the following expression:

$$\delta E = [E_{DMC^-(Q_{DMC})} - E_{DMC^-(Q_{DMC^-})}] + [E_{DMC(Q_{DMC^-})} - E_{DMC(Q_{DMC})}]. \quad (4.6)$$

First, one calculates the geometry of DMC and of DMC^- , giving optimized structures with a set of coordinates Q_{DMC} and Q_{DMC^-} and the corresponding energies $E_{DMC}(Q_{DMC})$ and $E_{DMC^-(Q_{DMC^-})}$. One can then calculate the anion energy at the geometry of the neutral molecule Q_{DMC} , having $E_{DMC^-(Q_{DMC})}$, and other way around, calculate the energy of the neutral DMC in the anion geometry Q_{DMC^-} and getting $E_{DMC}(Q_{DMC^-})$. The maximal energy one can get out of the sudden electron attachment/detachment process is a sum of two terms, the energy difference between the neutral DMC and suddenly attached electron plus the energy difference of the detachment process.

According to Eq.(4.6), δE is 0.45 eV for the field-off, and around 2.1 eV for the field-on case. The latter value shows that a substantial amount of energy can be gained due to vertical electron attachment/detachment processes, potentially allowing to overcome the typical β rotational barrier. This is thought to remain true even if changes due to the surface are taken into account. Nevertheless, multidimensional dynamics as well as explicit treatment of the surface are necessary to prove whether the energy is being channeled into the right direction, verifying in that way the relevance of the proposed mechanism.

Chapter 5

Substitution Effects: Azobenzenes and Related Compounds

5.1 Experimental Observations

Thermal *cis*→*trans* isomerization of ABs has been a topic of interest for many years [93, 94, 95], with doubts remaining on the true nature of the reaction path (rotation or inversion) as well as the structure of the corresponding TS. This reaction is assumed to happen in the ground state of the molecule, see Section 3.3. The switching of adsorbed AB derivatives enforced by light or the STM, with either tunneling electrons and/or electric field, has been successful [11, 16, 17, 18]. The backreaction, *cis*→*trans*, is often induced thermally, by annealing the system [18]. In Ref. [18], it was demonstrated that for the thermal reaction the activation energies and kinetic rates give completely different results, compared to kinetics for molecules at surfaces, when measured in solution.

The mechanism of thermal isomerization of ABs was investigated for quite some time experimentally [94, 96, 97, 98]. In the literature, there are very few theoretical studies on this topic [93]. In this work, switching kinetics will be studied with respect to substitution, observing changes on the isomerization rates with the type, positioning and number of functional groups.

It was assumed that the ground state kinetics run over a linear TS (from now on

called *inversion* TS), a model proposed first by Talaty and Fargo in the sixties [84]. Transition structures of AB molecules have been studied by Kucharski and coworkers [99], where it was assumed that the reaction runs over the energetically most favorable path, *i.e.*, the inversion in α , see Fig 3.1, for which the angle approaches 180° , leaving the double N=N bond intact. In Section 3.3, we saw that the reaction path is neither pure *inversion* in α nor pure *rotation* over ω but some kind of concerted motion (the TS reaches, in most cases, $\alpha \approx 180^\circ$ and $\omega \approx 90^\circ$, see Table 3.4 and Fig. 3.5).

Push-pull molecules (an acceptor group is placed on one, and a donor group on the second phenyl ring of AB) seem to change the isomerization path, to rotation, particularly in polar solvents [100]. For these molecules the optimization of species in various environments is necessary in order to observe possible structural changes and formation of a dipolar TS (N=N bond having some single-bond character) influencing the reaction kinetics (see below).

Returning to general trends for kinetics of AB, Nishimura *et al.* [97, 100] suggested that the acceleration of rates comes from substituents being in the *para* position of the ring, irrespective of the substituent type. The rate should depend on the number of substituents, too, noticing that pronounced additive features appear when substitution takes place on a single phenyl ring. One should not forget that, no matter how large the influence on the activation barrier a substituent has, steric hindrances especially in *ortho* positions may cause significant changes on thermal isomerization rates.

5.2 Computational Analysis

Quantum chemical calculations on AB derivatives employing the B3LYP functional [101] and, if not otherwise specified, the 6-31G* basis set [102, 103, 104] will be reported. A significant number of AB type molecules (more than 90 in total) have been studied. Processes at surfaces are still not well understood. As a prerequisite the thorough systematic analysis of pure thermal isomerization (for the gas phase and in solution) depending on various substitution effects is essential. Ideally, one would be able to predict the isomerization behavior of any AB derivative at

least in the gas phase. Solvents, on the other hand, certainly influence kinetic rates, which provides reason to repeat the calculations in a “solution like environment” by introducing the polarizable continuum model (PCM) [47], given in Section 2.1.5. The effects of substitution and an environment will be tested for UV/Vis absorption spectra, as well, albeit not immediately relevant for thermal kinetics. At last, some of the latest switching candidates will be introduced: (i) ABs with an extra azo-phenyl group, so called bisazobenzenes, and (ii) systems which have an azomethine (-CN=N-) group, instead of an azo-moiety, the so-called imines [105].

The minimum energy path for thermal *cis*→*trans* isomerization for TBA is given in Fig. 5.1. Starting from the reactant, *cis*, the isomerization proceeds through the TS and continues to products, *trans* molecules. For *cis* and *trans* species, minima are determined by geometry optimizations. Transition states (TSs) have been found using the synchronous transit-guided quasi-Newton method, STQN (QST2 and QST3), see page 24. For ABs, normal mode analysis

of the linear TSs (angle of the NNC unit reaches $\approx 180^\circ$) delivered a single imaginary frequency (usually around $i400\text{ cm}^{-1}$) in the characteristic switching mode of the AB molecule. For TBA, values for angles α and ω , for all stationary structures are given in Fig. 5.1, too.

Once we found minima and the corresponding TS, normal mode analysis delivers thermodynamical data. For example, the Gibbs free energy is given as

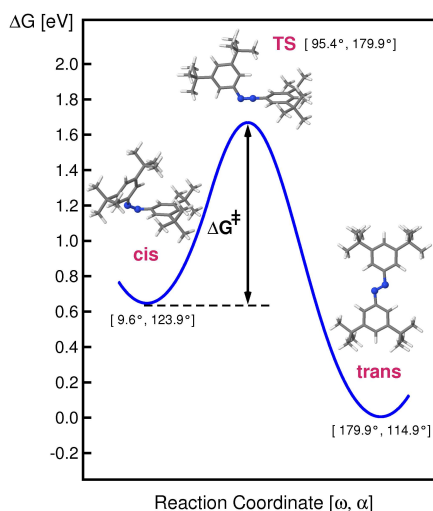


Figure 5.1: Thermal isomerization path for TBA containing optimized stationary structures for describing the reaction process. On the top, the optimized TS, with an activation free energy, ΔG^\ddagger of 1.03 eV, relative to the *cis* form, is shown.

$$G = H - TS \quad (5.1)$$

where H is the enthalpy for ideal gas conditions:

$$\begin{aligned} H &= U_{el} + U_{vib} + U_{rot} + U_{trans} + pV \\ &= E_{el} + E_{ZPE} + \Delta E_{vib}(T) + 4RT. \end{aligned} \quad (5.2)$$

Here $U_{el} = E_{el}$ is the electronic energy calculated from B3LYP, $U_{vib} = E_{ZPE} + \Delta E_{vib}(T)$, where E_{ZPE} and $\Delta E_{vib}(T)$ stand for the zero point and thermal vibrational contributions to the energy, respectively. $U_{rot} = \frac{3}{2}RT$ and $U_{trans} = \frac{3}{2}RT$ are rotational and translational contributions to U . Further, we have $pV = nRT$ for an ideal gas. In harmonic approximation, we have $E_{ZPE} = L \sum_i \frac{1}{2} h\nu_i$ (i labels normal modes with frequencies ν_i , L is Avogadro's number), and $\Delta E_{vib}(T) = L \sum_i h\nu_i (\exp(h\nu_i/k_B T) - 1)^{-1}$. The heat capacity at constant volume is given by

$$C_V = \left(\frac{\partial U}{\partial T} \right)_V = 3R + \frac{\partial \Delta E_{vib}(T)}{\partial T} \quad (5.3)$$

which is temperature dependent. Neglecting the *weak* temperature dependence and setting $C_V = C_V(T_0)$, the temperature dependent term for U becomes $U(T) = U(0) + C_V(T_0) \cdot T$ (T_0 is a reference temperature). $U(0) = H(0) = E_{el} + E_{ZPE}$ is the enthalpy at 0 K. If the entropy term in Eq.(5.1) is also considered T -independent, we can approximate the *activation free energy* term as

$$\Delta G^\ddagger(T) = \Delta H^\ddagger(0) + \Delta C_V^\ddagger(T_0) \cdot T - \Delta S^\ddagger(T_0) \cdot T, \quad (5.4)$$

with $\Delta B^\ddagger = B^\ddagger - B(R)$, where B^\ddagger is a property of the TS and $B(R)$ a property of the reactant. The advantage of Eq.(5.4) is that one can get ΔG^\ddagger for all T without recalculation of thermodynamical properties at every temperature. In our case, we were using the reference temperature $T_0 = 298.15$ K in most cases. This approximation has proven to be good, even for other systems [106]. From Eq.(5.4), the isomerization rate $k_{c \rightarrow t}$, is calculated as a function of the temperature with help of Eyring transition state theory [52], see Section 2.1.6.1, page 23:

$$k_{c \rightarrow t}(T) = \frac{k_B \cdot T}{h} \cdot e^{-\frac{\Delta G^\ddagger}{RT}} \quad (5.5)$$

$$= \frac{k_B \cdot T}{h} \cdot e^{-\frac{\Delta C_V^\ddagger}{R}} \cdot e^{\frac{\Delta S^\ddagger}{R}} \cdot e^{-\frac{\Delta H^\ddagger}{RT}}. \quad (5.6)$$

From an Arrhenius plot of $\ln(k_{c \rightarrow t}(T))$ vs. $1/T$, an activation energy E_a can be obtained from the slope and a prefactor A as the intercept of the curve with the ordinate according to the Arrhenius expression:

$$k_{c \rightarrow t}(T) = A e^{-\frac{E_a}{RT}}. \quad (5.7)$$

In the following we distinguish between four different "activation energies". The classical barrier is ΔE_{el}^\ddagger , the zero-point corrected barrier at 0 K is $\Delta H^\ddagger(0) = \Delta E_{el}^\ddagger + \Delta E_{ZPE}^\ddagger$, the Gibbs free activation energy is ΔG^\ddagger , and E_a is an activation energy from the Arrhenius plot. An example of the determination of A and E_a is given in Appendix C, see Table C.3 and Fig. C.2, for the M-TBA molecule.

5.3 Thermal Ground State Isomerization

We will consider whether and how electronically active and inactive substituents influence the energetics and kinetics of ABs. Dependence on the substituent type (electronically inactive, donors and acceptors) will be studied. Not only single, but also double and even triple substituted AB placed in *ortho*, *meta* and/or *para* positions of the molecule will be studied.

5.3.1 Electronically "Inactive" Substituents

Frontier molecular orbitals of AB, see Fig. 3.3 (right), have nodes in *meta* positions. In contrast, *ortho* and *para* positions can be classified as *active sites*. Substitution at active sites should influence the kinetics strongly. Placing a group, no matter of its nature, in *meta* positions is expected to have little or no influence on isomerization rates of AB-type molecules. It is also possible to have substituents which are generally weakly/not electronically active, leaving conjugated π system unaffected. Among electronically inactive substituents are bulky alkyl groups, such as the *tert*-butyl group of TBA, or an adamantyl group, which may be used as "spacers" for molecular switching at surfaces [107]. Structural parameters for ABs carrying the mentioned groups as well as kinetic data for thermal *cis*→*trans* isomerization are given in Table 5.1.

Concerning geometrical parameters and energy barriers, no major differences to non-substituted AB occur for molecules with these inactive functional groups (see Table 5.1). Hence, they all have similar values for rates and theoretical Arrhenius prefactors which are in the range of 10^{13} s^{-1} (see Table 5.2 below). The classical

molecule	ω	α	α'	r_{NN}	r_{CN}	$r'_{C'N}$	ΔE_{el}^\ddagger	ΔE_{ct}
<i>cis</i> -AB	9.8	124.1	124.1	1.250	1.436	1.436	–	
AB [‡]	90.0	179.4	117.0	1.226	1.335	1.453	1.10	0.66
<i>cis</i> -TBA	9.5	124.1	124.1	1.261	1.437	1.437	–	
TBA [‡]	87.7	179.9	117.1	1.227	1.336	1.453	1.11	0.65
<i>cis</i> -4-adam-AB	10.0	124.1	124.1	1.250	1.436	1.436	–	
4-adam-AB [‡]	90.0	179.1	117.2	1.227	1.334	1.448	1.11	0.66

Table 5.1: Selected geometry parameters of AB, TBA and 4-adamantyl-AB for the *cis* and TS configurations. All angles are given in degrees ($^\circ$), all distances in Å. The last two columns contain the classical barrier for *cis*→*trans* isomerization, ΔE_{el}^\ddagger , and the reaction energy $\Delta E_{ct} = E_{cis} - E_{trans}$ in eV.

activation energies are around 1.1 eV.

5.3.2 Substitution with Electronically “Active“ Groups

In the following, -NH₂, and methoxy groups, -OMe, are chosen as representatives of electron donor groups, possessing a +M effect (stabilizing positive charges). Mono-substitution, as well as di-substitution (on a single phenyl ring, or on both phenyls) was examined. Similarly, also electron withdrawing groups with a -M effect were considered, namely -NO₂ and -CN groups. Finally, the case of *push-pull* molecules will be studied, with a donor on one, and an acceptor on the other ring.

5.3.2.1 Single Substitution with Donors and Acceptors

The case of a single substitution (one group in either *meta* or *para* positions of a phenyl ring) is studied in Table 5.2. Here, thermodynamical parameters are calculated for the thermal isomerization as described in Section 5.2. One can notice that zero-point corrections to the classical activation barrier are in the range of 0.07 eV (an exception is 4-NH₂-AB, where it is much smaller), increasing the classical barrier. The fitted Arrhenius activation energy, E_a is in most cases identical to $\Delta H^\ddagger(0)$.

Some first conclusions can be drawn from Table 5.2:

molecule	ΔE_{el}^\ddagger	$\Delta H^\ddagger(0)$	ΔS^\ddagger	$\Delta G_{298.15K}^\ddagger$	$k_{c \rightarrow t, 298.15K}$	$A \times 10^{-12}$	E_a	σ
AB	1.10	1.17	+13.91	1.11	8.19×10^{-5}	23.3	1.17	0.00
4-CN-AB	0.91	0.97	+4.22	0.95	2.52×10^{-2}	7.93	0.97	+0.86
4-NO ₂ -AB	0.83	0.89	-0.64	0.88	2.70×10^{-1}	4.57	0.89	+1.25
4-ada-AB	1.11	1.15	+14.21	0.98	1.39×10^{-4}	34.6	1.03	–
4-OMe-AB	1.07	1.14	+5.78	1.11	8.52×10^{-5}	8.84	1.14	-0.27
4-NH ₂ -AB	1.03	1.04	+7.86	1.06	5.05×10^{-4}	10.9	1.09	-0.66
3-CN-AB	1.02	1.09	+6.08	1.06	5.26×10^{-4}	7.93	1.09	0.56
5-NO ₂ -AB	1.01	1.08	+6.13	1.05	7.54×10^{-4}	9.57	1.08	+0.71
5-NH ₂ -AB	1.08	1.14	+8.29	1.11	9.71×10^{-5}	11.9	1.14	-0.16

Table 5.2: Activation parameters, as well as calculated rates and prefactors in s^{-1} for various mono-substituted ABs. Energies in eV, entropies in J/K·mol. The last column gives the Hammett substituent constants σ , taken from Ref. [108].

(1) One finds significant changes for ABs which have extra functional groups in *para* and *ortho* positions. Acceptors are very efficient in reducing the isomerization barrier, by about 0.30 eV in the case of the strongest acceptor, -NO₂. Donors (-OMe and -NH₂) are less efficient, having barriers that are similar to the one of AB. The lowering of activation barriers can be explained with the help of mesomeric structures (see Fig. 5.2). Accordingly, a linear TS is stabilized by an acceptor in *para* or *ortho* position. In contrast, donors don't lead to the stabilization of the linear TS, irrespective of their position, as far as mesomeric structures are concerned. Nevertheless, *para* substitutions with donors show a slight lowering (less than 0.10 eV) of the activation barrier, confirming the statement that no matter of the functional group type, *para* substitution accelerates the kinetics of the system [97].

(2) On the contrary, by *meta* substitutions only small changes in activation energies and moderate enhancements of isomerization reactions are found. For substitution in *meta*, no large stabilization of the linear TS is expected because resonance structures as in Fig. 5.2 are unlikely. Further, this inactivity is due to the fact that the frontier orbitals have nodes in *meta* positions, as stated above. Substitution does not only affect the rates and properties of molecules but it can influence the structure of a TS, as well [95]. Molecules carrying acceptors are found to isomerize on the substituted side, while they isomerize on the opposite ring for donor-substituted molecules. This is demonstrated in Fig 5.3, where -NO₂ is an example acceptor and -NH₂ the example donor group. These findings were explained by Nishimura [100],

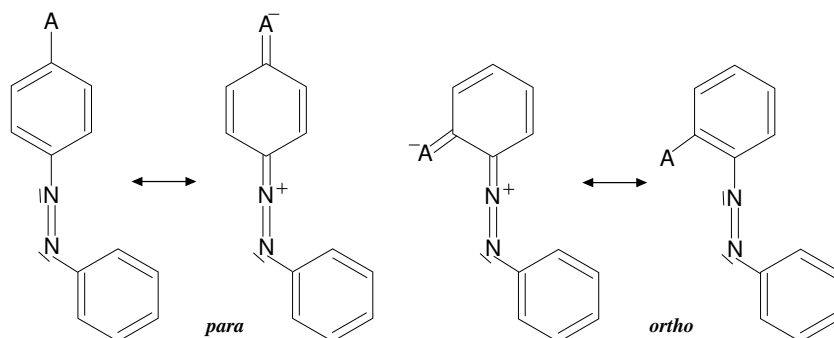


Figure 5.2: Mesomeric structures of an AB with a linear NNC unit and an acceptor in a *para* or in *ortho* position.

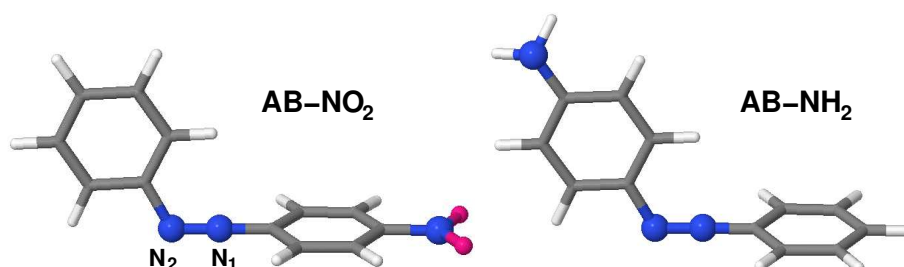


Figure 5.3: Computed TS geometries for mono-substituted ABs: On the left hand side, AB substituted with an electron acceptor ($-\text{NO}_2$) allows linearization on the substituted phenyl side. On the right side, AB with a donor ($-\text{NH}_2$) isomerizes on the opposite side instead.

coming to the conclusion that, if the AB has an electron accepting group at the ring close to N_1 as in Fig 5.3 (left), a repulsive force between the substituent and the lone electron pair on N_1 atom will be lowered, increasing the s character of the CN_1 bond. This leads to an increased α angle, causing the inversion to take place at N_1 far more easily than at N_2 . The situation is completely different if AB carries an electron donor group. For the case of multiple substitutions, the TS structure depends on the nature and position of extra groups.

5.3.2.2 Double Substitution with Donors

As representatives of electron donor groups, $-\text{NH}_2$ and $-\text{OMe}$ were chosen. Di-substitution took place on a single phenyl ring, or on both phenyls. In Table 5.3, we give activation and reaction energies for diamino-ABs (left: single ring, right:

double-ring substitution). From the Table, the following conclusions can be drawn:

(1) If substituents are at one ring, classical activation energies ΔE_{el}^\ddagger are in the range from 0.90-1.15 eV. We found that they depend very little on the substituent position, even if they are placed at the active centers of the parent molecule. The lowest value of approximately 0.90 eV was found for 2,6-NH₂-AB (both groups in *ortho* positions) compared to that of pure AB of ≈ 1.10 eV. This is mostly due to the fact that the *cis* isomer is destabilized in this case. For comparison, in the case of mono-amino ABs, 4-NH₂-AB and 5-NH₂-AB, the activation energies were 1.03 eV and 1.08 eV, respectively.

(2) The energy differences, ΔE_{ct} , between the *cis* and *trans* isomers vary in the range from 0.60 to 0.90 eV with respect to both, single and double ring -NH₂ substitution (an exception is 6,6'-NH₂-AB where ΔE_{ct} is 1.02 eV). Large values of ΔE_{ct} are mostly associated with destabilized *cis* forms.

(3) Looking at the right half of Table 5.3 (double substitutions), we find ΔE_{el}^\ddagger values between 0.98 and 1.24 eV. Thus, activation energies can now be lower or higher when compared to AB (1.10 eV).

Generally, the permanent dipole moment experiences strong changes due to substitution as well. Specifically, the largest values occur in the case of *ortho* substitutions, keeping in mind that *cis* isomers typically have larger dipole moments than the *trans*. The highest value, of 6.64 D, was found for *cis*-4,6'-NH₂-AB.

Concerning the geometries of all the derivatives, dihedral angles ω and angles α and α' are found to have almost the same values as for non-substituted AB. Significant changes are noticed, though, considering bond lengths. There exists a weak trend for the NN bond, which is elongated in all the cases when the substituents are in *ortho* and *para* positions, labeled 2,3,5 and 2',3',5' in Fig. 3.1. An electron donor has an energetically high lying HOMO, which can populate the LUMO of AB. The LUMO is antibonding between the nitrogens, and has bonding character between the C and N atoms. When populated we should, therefore, expect a longer NN bond and a shorter CN distance, *i.e.*, NC' bond. The elongation of the NN distance is not very pronounced, contrary to CN' bond shortening, which can be strong, particularly in *trans* forms. The most extreme case was noticed for the substitution on a single

type	substituents	ΔE_{ct}	ΔE_{el}^\ddagger	substituents	ΔE_{ct}	ΔE_{el}^\ddagger
o,o				3,2'-NH ₂	0.60	1.22
o,m	2,3-NH ₂	0.70	1.05	2,3'-NH ₂	0.61	1.11
o,p	2,4-NH ₂	0.64	1.06	2,4'-NH ₂	0.67	1.21
o,m	2,5-NH ₂	0.64	1.02	2,5'-NH ₂	0.62	1.11
o,o	2,6-NH ₂	0.90	0.90	2,6'-NH ₂	0.79	1.16
m,m				3,3'-NH ₂	0.63	1.13
m,p	3,4-NH ₂	0.70	1.05	3,4'-NH ₂	0.67	1.08
m,m	3,5-NH ₂	0.64	1.15	3,5'-NH ₂	0.64	1.11
m,o	3,6-NH ₂	0.85	1.07	3,6'-NH ₂	0.89	0.98
p,p				4,4'-NH ₂	0.74	1.18
p,m	4,5-NH ₂	0.70	1.05	4,5'-NH ₂	0.69	1.22
p,o	4,6-NH ₂	0.78	1.02	4,6'-NH ₂	0.90	1.17
m,m				5,5'-NH ₂	0.66	1.24
m,o	5,6-NH ₂	0.74	1.05	5,6'-NH ₂	0.89	0.99
o,o				6,6'-NH ₂	1.07	1.02

Table 5.3: Results for classical activation barriers, ΔE_{el}^\ddagger and *cis-trans* energy differences, ΔE_{ct} of di-substituted amino-ABs. On the left, functional groups on a single ring and on the right side of the table, -NH₂ groups placed on both rings are shown. All energies are given in eV.

ring, with donors in 2,6 positions, where the NC' bond length is 1.38 Å compared to about 1.44 Å for the pure AB molecule.

We find the same trend concerning activation barriers and geometries, as for amines also, in the case of methoxy substituted azobenzenes (not shown). Activation barriers for all the derivatives are between 1.05 eV for 3,4'-OMe-AB and 1.17 eV for 4,4'-OMe-AB. Taking a look at ΔE_{ct} between the conformers, they seem to be lower than in the diamino case. The lowest is for 2,6-OMe-AB ($E_{ct}^\ddagger \approx 0.43$ eV) compared to 0.90 eV of 2,6-NH₂-AB, which is due to very strong steric hindrances initiated by the -OMe group positioned in *ortho* position, *i.e.*, near to the NN double bond.

5.3.2.3 Double and Triple Substitution with Acceptors

We will now consider doubly and triply substituted ABs with electron acceptors, the cyano -CN and the nitro -NO₂ groups. The acceptors stabilize the collinear TS structure, thus also reducing isomerization barriers. Further on, acceptors can

support the electron donor character of the NN double bond, implying that one of the ring loses its aromaticity, as predicted with the mesomeric structures (see Fig. 5.2). Classical activation barriers, ΔE_{el}^\ddagger , and reaction energies, ΔE_{ct} , for selected species are given in Table 5.4 (on the left: all acceptors are at the same ring and on the right: substitution on both phenyls takes place). From the Table, some conclusions can be drawn:

(1) The largest reduction of the inversion barrier is expected when AB carries acceptors in active centers (*ortho* and *para*), as indicated already for mono-substituted species in Table 5.2. This is even more obvious for multiple-substituted ABs, in particular when all acceptors are located at the same ring, Table 5.4 (left).

substituents	ΔE_{ct}	ΔE_{el}^\ddagger	substituents	ΔE_{ct}	ΔE_{el}^\ddagger
2,4-NO ₂	0.48	0.52	2,2'-NO ₂	0.37	0.87
2,5-NO ₂	0.51	0.65	2,3'-NO ₂	0.51	0.74
2,6-NO ₂	0.44	0.37	2,4'-NO ₂	0.48	0.77
3,5-NO ₂	0.68	0.94	2,5'-NO ₂	0.48	0.76
3,6-NO ₂	0.63	0.52	3,3'-NO ₂	0.70	1.05
2,4,6-NO ₂	0.43	0.20	3,4'-NO ₂	0.67	0.89
			4,4'-NO ₂	0.65	1.09
			4,5'-NO ₂	0.66	0.90

Table 5.4: Results for classical activation barriers, ΔE_{el}^\ddagger and *cis-to-trans* energy differences, ΔE_{ct} of double and triple substituted nitro-ABs. On the left, there are two and three functional groups on a single ring and on the right side of the table, -NO₂ groups are placed on both rings. All energies are given in eV.

The barrier for the nitro-ABs reduces significantly upon substitution on one ring when compared to the ones of donors or pure AB (around 1.10 eV). The lowest activation energies are found for molecules which have two or, in an extreme case, three acceptor groups at one ring, *e.g.*, 2,4-NO₂-AB, 2,5-NO₂-AB, 2,6-NO₂-AB and 2,4,6-NO₂-AB. The latter derivative has a barrier of only 0.20 eV. It is found that, every extra nitro group in *ortho* and/or *para* lowers the activation energy by about 0.30 eV.

The additivity rule for barriers naturally translates into an additivity rule for logarithmic rates. This kind of rule was proposed and observed experimentally by Nishimura [100]. If one assumes that for every extra nitro group *i* the activation

energy is lowered by an amount Δ_i , we can write $\Delta E_{el}^\ddagger \approx \Delta E_{el}^\ddagger(0) + \sum_i \Delta_i$ (where $\Delta E_{el}^\ddagger(0)$ is the barrier for the parent molecule). Assuming that the Arrhenius law is valid and setting $E_a \approx \Delta E_{el}^\ddagger$, we get

$$\ln(k_{c \rightarrow t}) = \ln(k_0) - \sum_i \frac{\Delta_i}{RT} \quad (5.8)$$

where k_0 is the rate constant for the non-substituted molecule.

(2) The barriers also lower significantly in the case where both acceptors are placed on two phenyl rings, which was not the case for electron donors. Here, however, the additivity rule for activation energies does not hold, in agreement with experimental observations [100]. In 4,4'-NO₂-AB, for example, the activation energy is 1.09 eV and thus higher than that of the singly, *para* substituted ring, 4-NO₂-AB, see Table 5.2. A simple explanation comes from mesomeric structures shown in Fig. 5.2. Only an acceptor on the ring, which is directly attached to the inverting N atom stabilizes a linear TS.

(3) Acceptors in *meta* positions are generally quite inefficient, as expected.

Nitro groups also affect the structural properties of molecules. The dihedral angle ω for *cis* isomers (value of around 10° for the AB) varies from 2.2° for 3,6-NO₂-AB up to 18° for 2,2'-NO₂-AB. Often, derivatives with acceptors in *ortho* and *meta* positions have, because of sterical hindrances, higher values for the ω angles. Bond lengths are not drastically changed. For *trans* conformers, values for the dipole moments are sometimes higher when compared to the ones in *cis*, mostly in the case of multiple substitutions on a single phenyl ring. The largest dipole moment of ≈ 8.07 D was found for *trans*-2,5'-NO₂-AB.

Fourteen different di- and tri-substituted cyano-azobenzenes were calculated as well (not shown). For these cases lowering of activation barriers is accounted as well, but the overall influence on the AB energetics is not as strong as for the nitro groups, because the -NO₂ group is a stronger electron acceptor than -CN. The lowest possible barrier was found for the 2, 4, 6-CN-AB having $\Delta E_{el}^\ddagger = 0.45$ eV. As in previous cases, substitutions on one ring lead to a more efficient lowering of the activation barrier compared to the two ring substitution case. The classical activation energy for 2,2'-

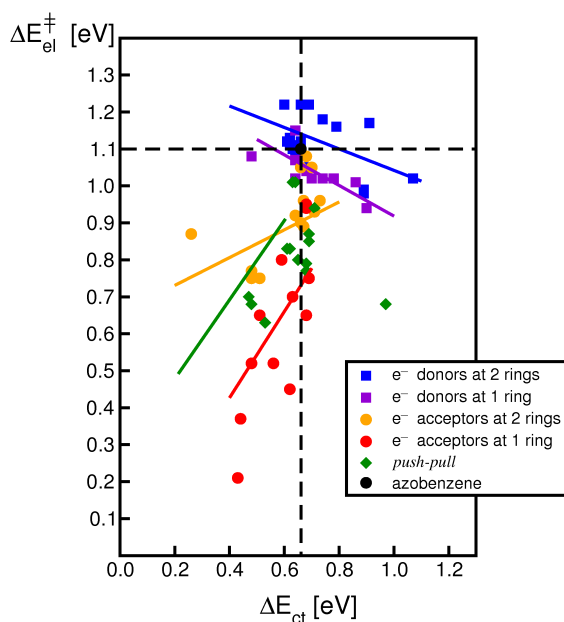


Figure 5.4: ΔE_{el}^{\ddagger} vs. ΔE_{ct} plot for different classes of di- and tri-substituted ABs: Acceptors on one ring, acceptors on two rings, donors on one ring, and donors at two rings; in green, the *push-pull* molecules. The vertical and horizontal dashed lines indicate reference values of the AB molecule, given as a black dot. Full lines serve as guides for the eye (obtained by linear regressions), for each of the five classes of substituted ABs.

CN-AB (*ortho* in both rings) is 0.96 eV and 0.70 eV for 2,6-CN-AB (*ortho* on the same phenyl). The additivity rule in case of one-ring substitutions is present here as well, for each *para/ortho* group the barrier lowers by ≈ 0.20 eV: ΔE_{el}^{\ddagger} is 0.91 eV, 0.65 eV and 0.45 eV for 4-CN-AB, 2,4-CN-AB and 2,4,6-CN-AB, respectively. Here, *meta* substitution is, as usual, less efficient. Compared to pure ABs no major geometry changes occur. The biggest dipole moment of 8.49 D was found for *trans*-2,5'-CN-AB.

The existence of some kind of correlation between activation and reaction energies, named *Linear Free Energy Relationship* (LFER) [100, 109], also for substituted ABs is supported by a plot of $\Delta E_{el}^{\ddagger} = f(\Delta E_{ct})$, as shown in Fig. 5.4, for different classes of substituted ABs.

From the graph one can see clearly that donors are found in the area of non-substituted AB, showing that donor groups have only a small influence on the energetics and kinetics. Contrary to this, acceptors on a single ring, have large ΔE_{ct} values which are usually associated with lower activation energies. In the case of acceptors the LFER was found with slopes that are large and positive, in contrast to donors, that have small and negative slopes. Generally, for the case of double substitutions on two rings, the additivity rule does not hold. Nevertheless, the LFER is valid here as well, ΔE_{el}^{\ddagger} correlates with the ΔE_{ct} .

5.3.2.4 Hammett Equation

A relation between the calculated isomerization rates obtained for single substituted ABs and substituent constants, is given through the Hammett formula [109, 108]

$$\log\left(\frac{k_X}{k_H}\right) = \rho \cdot \sigma_X \quad (5.9)$$

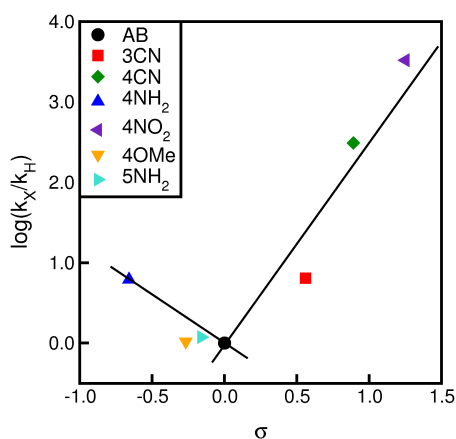


Figure 5.5: Hammett plot for mono-substituted ABs in *meta* and *para* positions of the molecule. σ values are presented in Table 5.2. The rates were calculated for $T = 298.15$ K, and refer to the *cis*→*trans* isomerization.

$f(\sigma)$ [109]. Here, k_X is the isomerization rate of the substituted AB molecule, k_H the rate of AB alone and σ are experimentally determined substituent constants which are, in this case, specially adapted for ABs [108]. The Hammett plot is shown in Fig. 5.5 where one can see that substituents with positive (3-CN, 4-CN and 4-NO₂) and negative (4-OMe, 5NH₂ and 4-NH₂) values of σ accelerate the reaction.

V-shaped Hammett plots have been found experimentally for substituted ABs [100]. Our plot is asymmetric with a linear dependence on the acceptor side (positive σ) and a positive slope of 2.14. The result confirms that a negative charge would develop at the reaction center in the transition state of the rate limiting step and the TS would be stabilized with the help of an acceptor functional group. The rate is then accelerated by electron withdrawing substituents, as presented in 5.3.2 and 5.3.2.2. Similar to Fig. 5.4, donor substituted ABs have negative slopes (negative LFER),

with reaction constant ρ (slope), and substituent constant σ_X . Eq.(5.9) results if there is a linear relationship between logarithmic rates, $\log(k_X)$, and logarithmic equilibrium constant, K_X of a reaction, related to a LFER. This is often the case for a wide class of reactions of aromatic compounds.

Calculated kinetic parameters for different mono-substituted molecules are shown in Table 5.2 (page 63). All the rates presented in the Table are larger than for the AB molecule; plotting these values one gets a V-shaped Hammett plot, $\log\left(\frac{k_X}{k_H}\right) =$

and acceptor functionalized ABs show positive slopes (positive LFER).

5.3.2.5 *Push-Pull Azobenzenes*

Push-pull ABs are of interest since a number of years, in particular also because of an unknown isomerization mechanism that might be operative in polar solvents. It was speculated that the isomerization mechanism changes from inversional in less polar solvents, to rotational in very polar environments [110]. Having an electron donor providing the charge for the phenyl ring (*push*), and an acceptor *pull*-ing the charges from the ring, the behavior of such molecules is untypical in all cases.

We studied several *push-pull* systems which are shown in Table 5.5. On the left hand side, different acceptors and donors have been attached in *para* positions of AB (the 4,4'-*push-pull* compounds), while on the right half also other positions were allowed. In the Table, we compare classical activation energies ΔE_{el}^\ddagger , and reaction energies ΔE_{ct} . The lowest barrier is calculated for 4NO₂-4'-NH₂-AB, so-called *Disperse Orange 3* (DO3), with $\Delta E_{el}^\ddagger = 0.77$ eV. Obviously, barriers are lower for both -NO₂ and -CN based compounds compared to single substituted ABs (see Table 5.2). The nitro group has the biggest influence on AB molecules and its position is of crucial importance for the energetics of such systems, see Fig. 5.4. The *cis*→*trans* energy differences, ΔE_{ct} are ~ 0.70 eV for 4,4'-*push-pull*-ABs and thus close to conventional ABs.

Let us now come to the right hand side of Table 5.5, where other positions of a donor -NO₂ on one, and an acceptor -NH₂ on the second ring, are considered. For three different systems, with -NO₂ in *ortho* position of the ring, *i.e.* 2-NO₂-2'-NH₂-AB, 2-NO₂-3'-NH₂-AB and 2-NO₂-4'-NH₂-AB, ΔE_{ct} is smaller than for AB and in the range of 0.47-0.53 eV. These compounds have the lowest ΔE_{el}^\ddagger , too. This shows that *ortho* substitution is even more efficient than the *para* for lowering the *cis*→*trans* activation energy. Overall, the amino group has a small barrier-lowering effect, which is more obvious for the *para* (4') substitution. Moreover, -NO₂ is very inefficient in *meta*, giving large values for ΔE_{el}^\ddagger .

Dipole moments of *push-pulls* are very large (larger for *trans* than for *cis* isomers),

substituents	ΔE_{ct}	ΔE_{el}^\ddagger	substituents	ΔE_{ct}	ΔE_{el}^\ddagger
4CN-4'OMe	0.69	0.87	2NO ₂ -2'NH ₂	0.48	0.68
4CN-4'NH ₂	0.69	0.85	2NO ₂ -3'NH ₂	0.47	0.70
4NO ₂ -4'OMe	0.68	0.79	2NO ₂ -4'NH ₂	0.53	0.63
4NO ₂ -4'NH ₂ (DO3)	0.68	0.77	3NO ₂ -2'NH ₂	0.63	1.01
			3NO ₂ -3'NH ₂	0.64	1.01
			3NO ₂ -4'NH ₂	0.71	0.94
			4NO ₂ -2'NH ₂	0.61	0.83
			4NO ₂ -3'NH ₂	0.62	0.83
			4NO ₂ -5'NH ₂	0.65	0.80
			4NO ₂ -6'NH ₂	0.97	0.68

Table 5.5: ΔE_{el}^\ddagger and ΔE_{ct} values for *push-pull* ABs. On the left, 4,4'-substitution and on the right, other possible substitution combinations are shown. Energies are given in eV.

particularly for 4,4' species. The largest computed $|\mu_{tot}|$ of 9.79 D has the *trans*-DO3 molecule, with its donor and acceptor functional groups positioned at the largest possible distance.

5.3.2.6 Solvent Effects: DO3 within the Polarizable Continuum Model

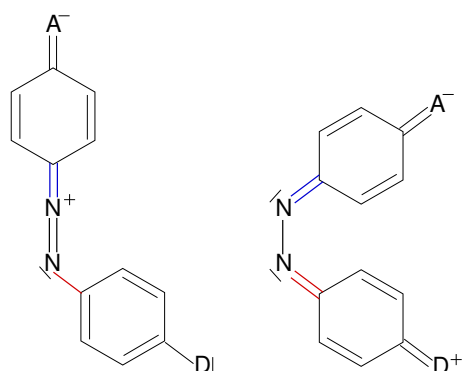


Figure 5.6: Mesomeric structures of *push-pull* ABs for stabilized inversional (left) and bipolar (rotational) TS (on the right).

In order to study solvent effects, DO3 has been fully reoptimized in various solvents within the PCM scheme. The TS was determined with the help of the QST3 method. In Fig. 5.6 we show mesomeric structures of a linear TS (left) which is found in the gas phase, and a possible bipolar TS (on the right), which may gain importance in polar environments. The latter would favor a rotational isomerization mechanism around the NN bond. In less polar solvents, DO3 follows an isomerization mechanism similar to the one in the gas phase. This is demonstrated in Table 5.6, where the *cis*→*trans* isomerization of DO3 in various solvents is studied. The range of solvents used is

wide, from $\varepsilon = 1.92$ for heptane, to $\varepsilon = 46.7$ for DMSO.

solvent	ε	$\frac{\varepsilon-1}{\varepsilon+1}$	ΔE_{el}^\ddagger	$k_{c \rightarrow t, 298.15\text{K}}$	ΔS^\ddagger	$A \times 10^{12}$	E_a	type
gas phase	1.000	0.000	0.77	5.2	1.15	7.06	0.73	inversion
heptane	1.920	0.315	0.72	28.2	1.41	7.20	0.68	inversion
cyclohexane	2.023	0.338	0.72	30.9	1.35	6.97	0.72	inversion
carbontetrachloride	2.228	0.380	0.72	42.5	1.95	7.33	0.67	inversion
benzene	2.247	0.384	0.73	75.9	6.34	12.3	0.67	inversion
ether	4.335	0.625	0.68	151.4	0.88	5.85	0.64	rotation
chlorobenzene	5.621	0.698	0.65	228.1	-4.84	3.92	0.61	rotation
aniline	6.890	0.746	0.64	379.9	-5.95	3.61	0.60	rotation
dichlormethane	8.930	0.798	0.61	632.7	-9.40	2.54	0.58	rotation
quinoline	9.030	0.801	0.62	584.1	-7.56	3.23	0.58	rotation
dichlorethane	10.360	0.824	0.61	888.9	-8.77	2.72	0.57	rotation
acetone	20.700	0.905	0.58	1326.1	-14.23	1.60	0.55	rotation
DMSO	46.700	0.958	0.55	2321.6	-17.37	1.10	0.52	rotation

Table 5.6: Energetic and kinetic data for DO3 in different environments within the PCM: Classical activation energies ΔE_{el}^\ddagger , $k_{c \rightarrow t}$ at 298.15 K, activation entropies, ΔS^\ddagger , Arrhenius prefactors, A , and Arrhenius activation energies, E_a . Energies are given in eV, rates and prefactors in s^{-1} , entropies in $\text{J/K} \cdot \text{mol}$.

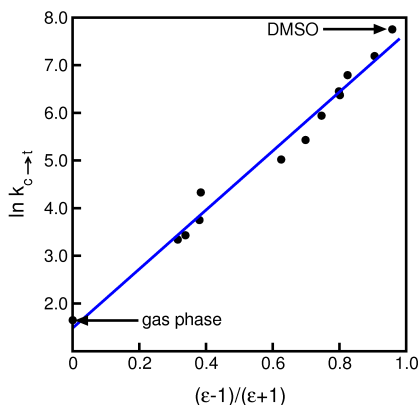


Figure 5.7: Kirkwood plot for DO3 in different PCM solvents. The line is a linear fit to the data.

values for large ε , which is consistent with experimental findings [100].

In less polar solvents, ΔE_{el}^\ddagger values are slightly reduced relative to the gas phase and the reaction mechanism is of the inversion type. In very polar solvents, such as acetone or DMSO, the classical barrier (ΔE_{el}^\ddagger) is significantly reduced relative to the gas phase, and the reaction proceeds through a rotational pathway. As a consequence, *push-pull* molecules show obviously a large rate dependence on the solvent polarity. One finds a linear dependence of the $\ln(k_{c \rightarrow t})$ values on $\frac{\varepsilon-1}{\varepsilon+1}$ as shown in Fig. 5.7, known as a *Kirkwood plot*. A linear dependence from $\frac{\varepsilon-1}{\varepsilon+1}$ is also found for Arrhenius activation energies, E_a , and activation entropies, ΔS^\ddagger . In particular, one finds negative ΔS^\ddagger

In Ref. [110] it was experimentally demonstrated for 4NO₂-4'NMe₂-ABs and related

push-pull species, that quantitatively $k_{c \rightarrow t}$ depends on ε roughly according to

$$\ln(k_{c \rightarrow t}) = a + b \left(\frac{\varepsilon - 1}{\varepsilon + 1} \right) \quad (5.10)$$

where a is the rate at $\varepsilon = 1$ and b is the slope. The same linear relation is found in Fig. 5.7. Eq.(5.10) follows from a model based on the calculation of free energies of molecular, spherical dipoles embedded in a dielectric continuum [111]. According to Refs. [110] and [111], the slope of the curve is

$$b = \frac{1}{4\pi\varepsilon_0} \frac{3}{8k_B T} \left(\frac{\mu_{\ddagger}^2}{R_{\ddagger}^3} - \frac{\mu_c^2}{R_c^3} \right). \quad (5.11)$$

Here, μ_{\ddagger} and μ_c are the permanent dipole moments of the TS and the *cis* form, respectively, and R_{\ddagger} and R_c are molecular radii. All dipole moments increase in polar solvents (see Fig. 5.8). The largest dipole moment, for *trans* species, of 15.46 D was found for *trans*-DO3 in DMSO, using the PCM. From Fig. 5.8 (left), one can see that also the dipole moment for the TS experiences strong changes with the dielectric constant reaching even more than 27 D for the DMSO solvent. This is due to the stronger stabilization of a bipolar TS in a polar environment. In contrast, the dipole moments of *cis* isomers experience less intense changes because of their compact geometry. If one uses "typical" values in Eq.(5.11), *i.e.*, $\mu_c \approx 9$ D, $\mu_{\ddagger} \approx 16$ D and takes $R_c \approx R_{\ddagger} \approx 6$ Å, one gets a slope of 7.5 for the prefactor to $\frac{\varepsilon-1}{\varepsilon+1}$. This is consistent with the slope of 6.2, actually found in Fig. 5.7. One has to notice that this estimate is only approximate since the dipole moment of the TS depends on the polarity of the solvent, and also the choice of the molecular radii is only approximate. However, the Kirkwood model explains nicely the kinetics for *push-pull* systems with respect to the polarity of the environment.

In Fig. 5.8, structural changes of the TSs as a function of the dielectric constant are summarized, too. In the central panel, it is seen that the angle α' doesn't undergo as a drastic change as the angle α , which changes from $\approx 180^\circ$ (for the inversion mechanism) to $\approx 130^\circ$ in DMSO (rotational mechanism). For the definition of angles, see Fig. 5.9. This indicates, once more, the transition from a inversional (gas phase) to a bipolar, rotational TS (acetone, $\varepsilon = 20.7$). The hypothesis of the dipolar resonance structure is also supported by analysis of computed bond distances. From Fig. 5.8 (right), one can see that the elongation of the r_{NN} bond

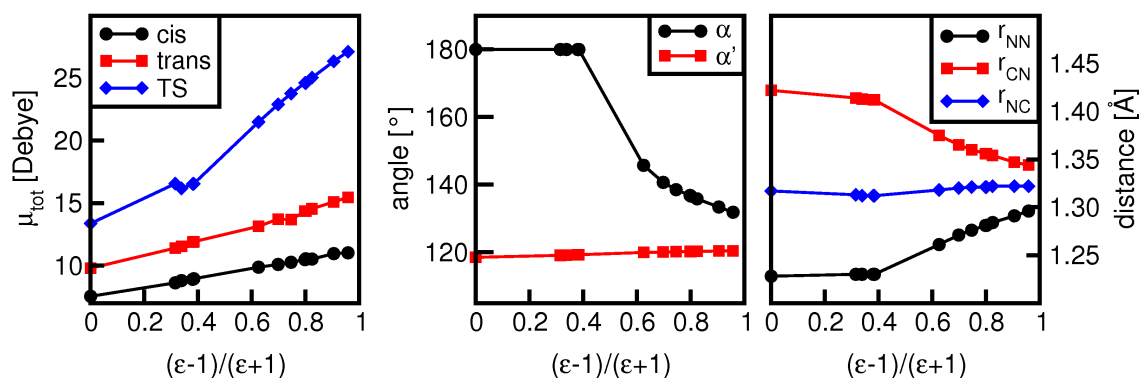


Figure 5.8: Change in the total dipole moment (left), angles of the TS (middle) and bond lengths of the TS (right) for DO3 molecule with respect to the relative solvent polarity. For the latter, the color coding fits to the representation of bond lengths in Fig. 5.6.

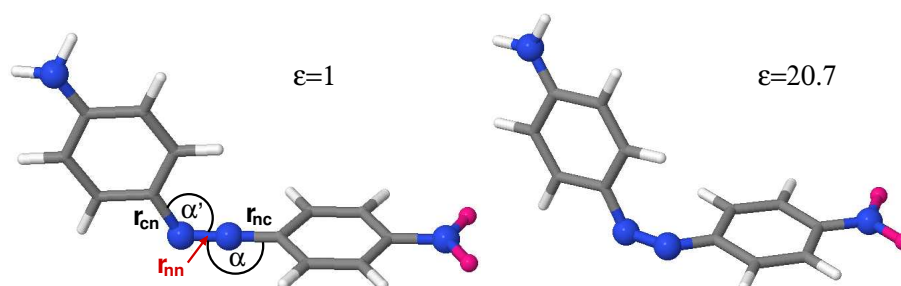


Figure 5.9: Transition state structures for DO3 in different environments: On the left hand side, the TS structure in the gas phase, and on the right hand side, optimized TS geometry in acetone.

goes from 1.228 Å in the gas phase to 1.296 Å in DMSO. One should keep in mind though that the elongation is far from what one would expect from a "true" single bond, as suggested from Fig. 5.6 (right).

5.3.3 Isomerization of TBA-like Species

Mono- and di-substituted TBA derivatives were constructed starting from the TBA by adding substituent in *para* positions: 4-methoxy-TBA (M-TBA), and 4,4'-dimethoxy-TBA (dim-TBA) [12]. Besides them, we also considered molecules where we replaced two *tert*-butyl groups with a -COOH, getting 3,5-di-*tert*-butyl-3',5'-dicarboxyl-AB (DBDCA) [112]. Another molecule is TBA', where we rearranged

positions for two out of four *tert*-butyl groups having 2,2',5,5'-tetra-*tert*-butyl-AB. These bulky molecules decouple the switching unit efficiently from a metal surface which is what makes them interesting for possible applications as molecular switches. The described systems were recently synthesized by Hecht *et al.* [113], and are listed in Table 5.7. Thermal isomerization of these molecules was investigated in solution. We apply Eyring TS theory to make contact with experimental data.

As before, the thermal isomerization can be described as a reaction running over an inversion TS as already defined. Thermodynamical data and rates were calculated at 303.15 K, which is the temperature that was considered experimentally in most cases. TBA was reoptimized completely within the PCM, for cyclohexane ($\epsilon = 2.023$). Concerning theoretical results (left half of the Table), we found for TBA in cyclohexane that the solvent slows down the *cis*→*trans* isomerization only slightly. The solvent effect is only moderate, yet in full agreement with recent findings [68]. The theoretical ΔH^\ddagger value is calculated from $\Delta H^\ddagger(T) = \Delta H^\ddagger(0) + \Delta C_V^\ddagger(T_0) \cdot T$. The experimental ΔH^\ddagger values were determined from a van't Hoff plot $\ln(k/T)$ vs. $1/T$.

The latter were determined from time-resolved UV/Vis spectra, see Fig. 3.2. The effect of the PCM field was tested also for the UV/Vis absorption spectra (see part 5.4).

For M-TBA (methoxy group in *para* position), the barrier is slightly reduced relative to the barrier of TBA which gave only a moderate enhancement of the rate constants. The molecule isomerizes at the side that doesn't carry the -OMe group. A second TS, where the inversion occurs on the N atom adjacent to the ring carrying the -OMe group has a higher activation energy and lower rate (see Appendix C). If another methoxy group is introduced, for diM-TBA, the barrier increases significantly and the rate is decreased by an order of magnitude when compared to TBA.

The strongest effect on kinetic rates was observed for the DBDCA molecule for which we observe a rate increase by a factor of nearly 70. Although being attached in *meta* positions, the two -COOH groups stabilize the TS via their -I effect. A smaller effect on the rate was noticed for the TBA' molecule which has the rate constant which is about 4 times larger than that of TBA. This is mostly due to enhanced Arrhenius prefactor. For TBA' the TS deviates slightly from linearity ($\alpha = 171^\circ$), most likely

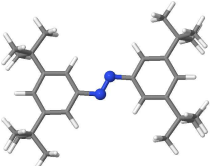
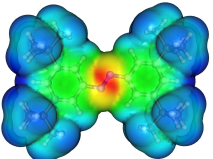
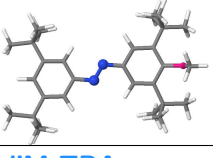
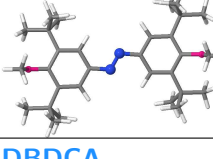
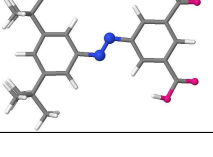
molecule	$k_{c \rightarrow t}$	ΔS^\ddagger	ΔH^\ddagger	k_{exp}	ΔS_{exp}^\ddagger	ΔH_{exp}^\ddagger
TBA 	theory, 303.15 K 3.96×10^{-5}	6.66	1.06	experiment (solvent), 303.15 K –	–	–
TBA + C₆H₁₂ 	9.48×10^{-6}	4.61	1.09	0.35×10^{-6}	-77.0 ± 18.0	0.91 ± 0.06
TBA' 	1.40×10^{-4}	16.22	1.04	4.94×10^{-6}	-50.6 ± 3.7	0.93 ± 0.01
M-TBA 	3.18×10^{-5}	0.84	1.05	0.58×10^{-6}	-37.8 ± 5.2	1.03 ± 0.02
diM-TBA 	3.09×10^{-6}	3.26	1.12	0.85×10^{-6}	-39.0 ± 3.5	1.01 ± 0.01
DBDCA 	2.67×10^{-3}	1.89	0.93	1.18×10^{-6}	-75.8 ± 13.2	0.89 ± 0.04

Table 5.7: Kinetic parameters for TBA and TBA derivatives (the abbreviations are given in the text) at 303.15 K. All experimental measurements were done in cyclohexane, except for DBDCA, which was measured in a 10:1 mixture of acetonitrile/MeOH. Calculations are done for the gas phase if not indicated otherwise. Energies are eV, rates in s^{-1} and entropies in J/K·mol.

due to sterical hindrances, which increases ΔS^\ddagger and thus the Arrhenius prefactor.

Finally, we need to compare computational results to experimental data (right half of the Table 5.7). With the exception of TBA and TBA', the activation enthalpies ΔH^\ddagger are in good agreement, *i.e.*, the experimental and theoretically derived Arrhenius slopes are very similar. Regarding activation entropies, ΔS^\ddagger , there is a big difference. These are small and positive according to theory, but large and negative according to experiment. Hence, Arrhenius prefactors are overestimated in theory, influencing absolute rates, which turned out to be too small in comparison to the experiment (by a factor of 3, for diM-TBA, up to a factor of 2000, for DBDCA). The large deviation for DBDCA can be assigned to the fact that the experiment was carried out in a CH₃CN/MeOH solvent mixture, and not in cyclohexane, which is well described by the PCM.

Apart from this, experimental and theoretical activation entropies are still deviating. Theory predicts a "less ordered" TS than the experiment. Possible sources of errors can be the PCM model, where the solvent molecules and their thermal motion are not explicitly included. Further, it may be that the harmonic approximation leads to the inaccurate calculation of activation entropies in large systems. However, experimental inaccuracies cannot be excluded neither.

5.4 UV/Vis Absorption Spectra

5.4.1 Influence of Donors and Acceptors

By optical excitations, in both directions, for ABs in solution and at surfaces, large yields of either *cis* or *trans* isomers are requested for. This implies that characteristic absorption bands (see Section 3.1), have to be well energetically separated in order to show good photochromic properties. For substituted ABs, a systematic study of these properties is needed. Thermal stability is of extreme importance for industrial purpose, too. Therefore, we will also search for ABs which are at the same time highly photochromic (having very distinct absorption properties for *cis* and *trans*), and thermally stable (having large *cis*→*trans* thermal activation barriers).

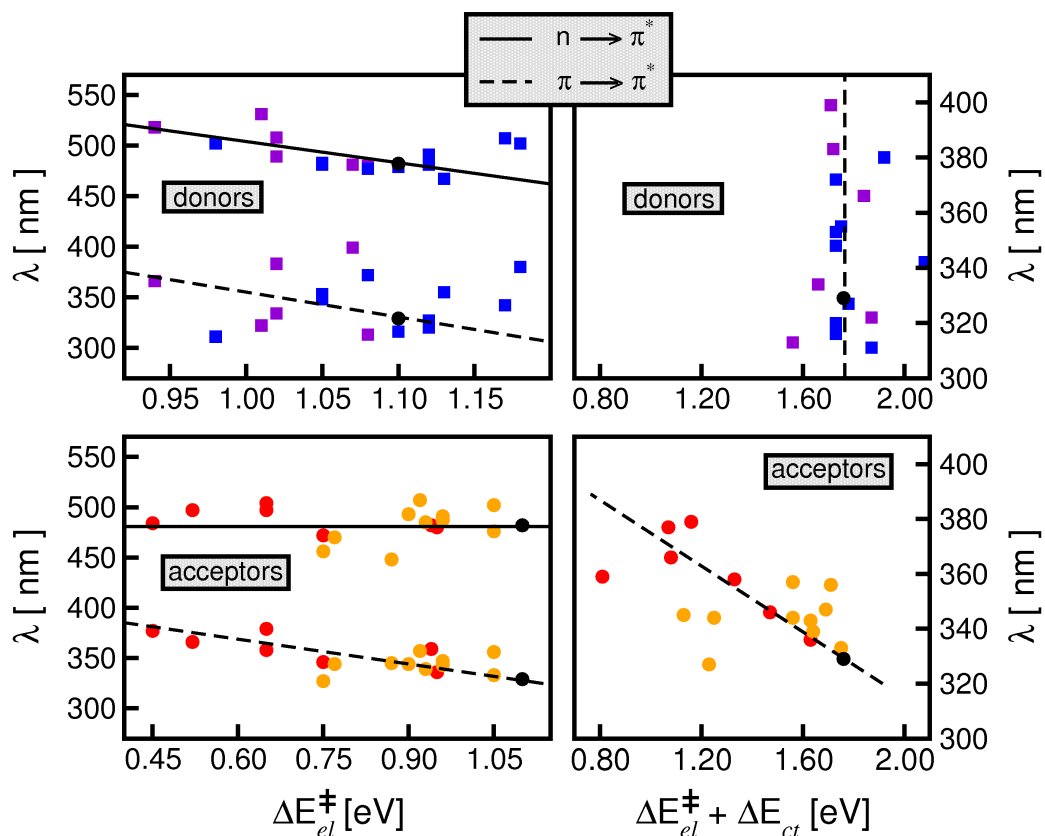


Figure 5.10: Left: $\pi \rightarrow \pi^*$ band maxima (lower curves), for *trans*, and the $n \rightarrow \pi^*$ band maxima (upper curves), for *cis*, for various substituted ABs plotted vs. activation energy ΔE_{el}^\ddagger for *cis* \rightarrow *trans* isomerization. Here, we didn't plot values for all the calculated derivatives but only selected ones. On the right hand side, the $\pi \rightarrow \pi^*$ transitions are additionally plotted as a function of the activation energy for *trans* \rightarrow *cis* isomerization. The color code is the same in Fig. 5.4. Black lines are given as a guide to the eye. Spectra were calculated at the TD-B3LYP/6-31G* level of theory on previously optimized *cis* and *trans* species.

Differences in UV/Vis spectra, due to substitutions, are noticeable in absorption band intensities and shifts of the band maxima. In order to study these, again, the B3LYP functional and the 6-31G* basis set were chosen. At first, the absorption spectra of donor or acceptor substituted ABs will be given. In Fig. 5.10, shifts of maxima of the characteristic absorption bands (the $n \rightarrow \pi^*$ transition for *cis*, at higher wavelengths and the $\pi \rightarrow \pi^*$ transition for *trans*, at lower wavelengths) are shown for various substituted ABs, as a function of the thermal activation energies, which were already presented and discussed. In the left panels, we plot absorption

maxima for donors and acceptors, *cis* and *trans*, vs. the classical *cis*→*trans* activation energy ΔE_{el}^\ddagger . On the right panels, absorption maxima of *trans* species ($\pi \rightarrow \pi^*$) are plotted vs. the classical *trans*→*cis* activation energies $\Delta E_{el}^\ddagger + \Delta E_{ct}$, in addition. Donor substitution affects both absorption bands about equally. Here, the energy difference between the *trans* isomer and the TS experiences almost no changes due to substitutions. Also, the energy range for ΔE_{el}^\ddagger is narrow because of the rather moderate influence of donors on reaction kinetics. Contrary to this, the electron acceptors show more or less a constant behavior for the $n \rightarrow \pi^*$ transition, *i.e.*, the absorption maximum doesn't depend on substitution, while the $\pi \rightarrow \pi^*$ absorption bands show a trend similar to the ones for the donors. Here, acceptors show good photochromic properties, since one of the bands is unaffected upon substitution while the other one can be "tuned".

All the acceptor-ABs have an ΔE_{el}^\ddagger lower than the non-substituted AB no matter whether the substitution takes place on a single or on both phenyls at the same time. Therefore, the thermal switching rates $k_{c \rightarrow t}$ are low which is not preferred for practical use. In contrast, donor substitution gives thermally more stable (*cis*) products, and *cis* and *trans* absorb at still sufficiently different wavelengths.

5.4.2 Influence of Solvent

In order to quantify the effect of the solvent within the PCM frame, UV/Vis spectra for *cis* and *trans* isomers using TD-DFT [42] were calculated, with B3LYP/6-311G* [31, 101, 114]. Optimized geometries for gas phase and PCM environment, calculated also on a B3LYP/6-311G* level, were used. The lowest twenty singlet excitations with excitation energies $E_i = hc/\lambda_i = hc\tilde{\nu}_i$ (λ_i and $\tilde{\nu}_i$ are excitation wavelengths and wavenumbers, respectively), and oscillator strengths f_i , were calculated. Using Gaussian broadening, we calculate molar extinction coefficients, with the an empirical broadening factor σ :

$$\epsilon(\tilde{\nu}_i) = \sum_i \frac{f_i}{\kappa} \frac{1}{\sigma \sqrt{2\pi}} e^{-\frac{1}{2}(\frac{\tilde{\nu}-\tilde{\nu}_i}{\sigma})^2}. \quad (5.12)$$

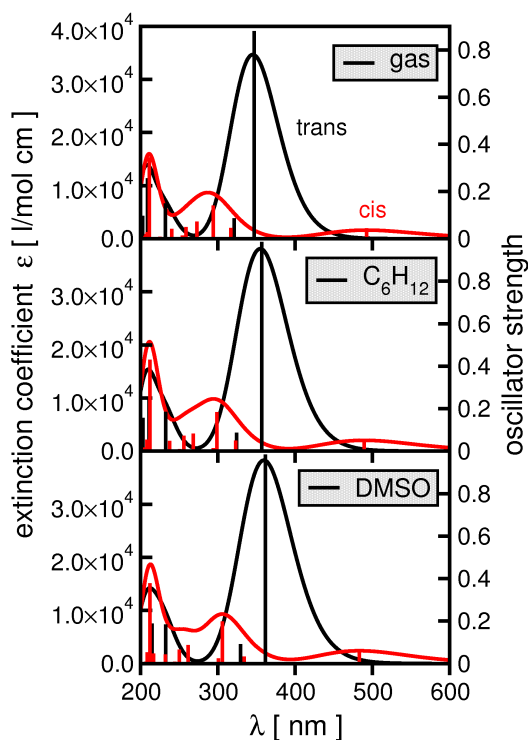


Figure 5.11: TD-B3LYP/6-311G* UV/Vis absorption spectra of the *trans* (black curves) and *cis* (red curves) TBA molecules. Upper panel is for the TBA in the gas phase, the middle one for the molecule in cyclohexane and the lowest panel describes spectra in a very polar environment, DMSO. Spectra are Gaussian broadened with $\sigma = 2500 \text{ cm}^{-1}$. Smooth curves correspond to extinction coefficients (left scale), while sticks represent oscillator strengths (right scales).

The exact expression for calculating κ^1 is:

$$\kappa = \frac{4m_e c^2 \varepsilon_0 \ln 10}{L e^2} = 4.318998 \times 10^{-10} \text{ mol/m.} \quad (5.13)$$

For TBA itself, in Fig. 5.11, the spectra are compared between the gas phase TBA, in a weakly polar solvent (cyclohexane, $\varepsilon = 2.016$) and in a more polar environment (DMSO, $\varepsilon = 46.8$). The PCM correction enters the spectra in two ways: (i) The geometry changes due to the reoptimization in a solvent and (ii) the PCM has an influence on excitation energies and transition dipole moments. For comparison, experimentally taken UV/Vis spectra of the TBA are shown in Fig. 3.2 (page 32).

For *trans*-TBA (and AB in general), the $n \rightarrow \pi^*$ transition is forbidden because of symmetry, while $\pi \rightarrow \pi^*$ is strongly allowed [69]. In the gas phase the $\pi \rightarrow \pi^*$ band appeared at 347 nm and in cyclohexane at 356 nm with even stronger

¹Consisting of fundamental constants: m_e the electron mass: $9.109382 \times 10^{-31} \text{ kg}$, ε_0 the vacuum permittivity $8.854187 \times 10^{-12} \text{ F/m}$, c the speed of light $2.997925 \times 10^8 \text{ m/s}$, L is Avogadro's number and e the electron charge of $1.602176 \times 10^{-19} \text{ C}$.

intensities. The LUMO, in this case, experiences stronger destabilization compared to HOMO-1 contributing to the band red shift. Experimental and theoretical values for absorption bands and their intensities are given in Table 5.8.

In the DMSO case, the band shifts even further to 361 nm. For *cis*-TBA, both transitions are allowed, albeit with weaker intensities. The $\pi \rightarrow \pi^*$ band appears at 294 nm for the gas phase and again, in solvent environment, red shifts to 298 nm, for cyclohexane and further to 304 nm in DMSO. In the case of the $n \rightarrow \pi^*$ transition, we have the value of 492 nm in the gas phase and 489 nm in the solvent, *i.e.*, this band experiences a blue shift. One of the possible explanations is that the LUMO destabilizes less in cyclohexane compared to the HOMO, which leads to the blue spectra shift and the intensity enhancement. The calculated gas phase spectra are in qualitative agreement (but with quantitative differences) when compared to experimental spectra. Valence excitations are red-shifted relative to the experiment by about 14 nm (for *cis*, $\pi \rightarrow \pi^*$) and about 50 nm (for *cis*, $n \rightarrow \pi^*$). Extinction coefficients are too large², but relative intensities are well reproduced.

transition	Gas		C ₆ H ₁₂		DMSO		Exp. (C ₆ H ₁₂)		
	<i>trans</i>	<i>cis</i>	<i>trans</i>	<i>cis</i>	<i>trans</i>	<i>cis</i>	<i>trans</i>	<i>cis</i>	
$\pi \rightarrow \pi^*$	λ [nm]	347	294	356	298	361	304	325	280
	<i>f</i>	0.8802	0.1411	0.9843	0.1837	0.9757	0.1968	v. strong	strong
$n \rightarrow \pi^*$	λ [nm]	486	492	486	489	479	479	450	440
	<i>f</i>	0.0000	0.0438	0.0000	0.0552	0.0000	0.0649	weak	medium

Table 5.8: Selected transitions of the TBA molecule in gas phase and in two different environments. Experimental transitions are labeled as very strong, strong, medium and weak signals [24].

In summary, solvent effects can be considered rather small for both non-polar and polar environments adopting a simple PCM scheme.

²Extinction coefficients depend very much on chosen broadening factors.

5.5 Bisazobenzenes

5.5.1 General

So far the effects of substituents on geometries, properties, reaction rates and absorption spectra of ABs were studied. We now discuss what happens if the substitution with azo-phenyl groups on plain AB in *meta* and *para* positions takes place. These newly built molecules will be called *bisazobenzenes* (or BABs shortly), see Fig. 5.12. Depending on the position of the second azo-group, different couplings occur, which is to be seen in particular in the absorption spectra. It is to be expected that upon substitution at the active *para* position of AB, the molecule experiences stronger coupling which would result in spectra that are very different from pure AB. In contrast, *meta* substitutions are supposed to couple less with the AB backbone and therefore not influence the spectra a great deal. Measured UV/Vis spectra and thermal $Z \rightarrow E$ isomerization for BABs are described in Ref. [113]. There, the two end-standing phenyl rings were additionally substituted in 3,5 and 3',5' positions, creating 3,3',5,5'-tetra-*tert*-butyl-bisazobenzenes (TT-BAB). The idea was not only to design a new candidate for the switch but to help molecules organizing at surfaces in ordered patterns, which was partially successful.

Optical isomerization to the *cis* form, of BABs adsorbed on gold, was not a success, though, probably because of strong intermolecular interactions. UV/Vis spectra were taken in solution, though, finding large dependence in photoreactivity upon *meta* or *para* substitutions (see below). Here, we will study the UV/Vis absorption spectra theoretically (Section 5.5.2) for TT-BABs. Since thermal isomerization in solution has also been studied experimentally we tried to explain possible reaction paths for this process (Section 5.5.3). Thermal isomerization runs from the $[Z, Z]$ form (all-*trans*), over the $[E, Z]$ specie, finally reaching the $[E, E]$ isomer. The path itself can be specified as a consecutive reaction, which is also experimentally supported [113]. Here, the thermal isomerization of non-substituted BABs will be discussed, mostly because of the lower computational cost. It has been shown before that the kinetics of pure AB and TBA molecules are quite similar because of the substitution with electronically inactive *tert*-butyl groups in *meta* positions. Hence, the thermal rates of BAB and TT-BAB molecules should be similar as well.

A coordinates sketch, which defines degrees of freedom necessary for further discussion, is presented in Fig. 5.12. In the case of unsymmetrically substituted ABs, two α angles exist, and for the situation of BABs, we find four α angles as it is shown in Fig. 5.12. We define these angles as the ones which are oriented to the inner side of the molecule (or N-N-C³), α_2 and α_3 in Fig. 5.12, as well as the angles oriented to the outer side of BAB (or C_e-N-N⁴), α_1 and α_4 in Fig. 5.12.

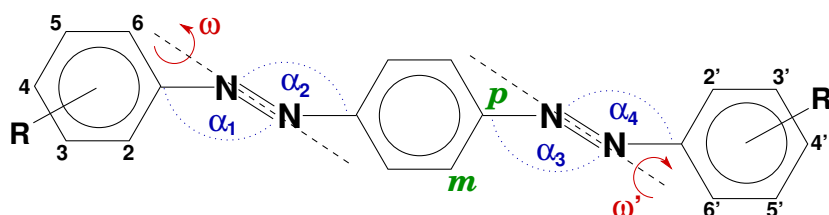


Figure 5.12: Scheme of BABs with numbering of the "external rings", inversion angles α , rotation dihedral angles ω and, in green, *meta* and *para* substitution centers.

The aim of computational study is to explain the different photoreactivity upon *meta* vs. *para* substitution, by calculating absorption spectra, and their thermal reactivity by applying Eyring TS theory.

5.5.2 UV/Vis Spectra and Photoreactivity of TT-BABs

Quantum chemical calculations of BABs and their derivatives carrying four *tert*-butyl groups (TT-BAB) will be presented. The analysis of TT-BAB is mostly studied for reference reasons and compatible comparison with experimental data. Under study are [*E*, *E*], [*E*, *Z*] and [*Z*, *Z*] isomers, for both *meta* and *para* substitution. The spectra are calculated in the same way as explained in Section 5.4.2, in the gas phase. Using Gaussian broadening, we calculated molar extinction coefficients given in Eq.(5.12), with σ chosen as 1300 cm^{-1} .

In Fig. 5.13 we compare calculated gas phase UV/Vis spectra of TT-BAB derivatives and compare them with spectra of the TBA molecule, calculated for *trans* and *cis* isomers (see also Fig. 5.11). In Fig. 5.13 a), in thin lines, TBA and mixtures be-

³C_c is the *central* carbon atom, belonging to the middle phenyl ring.

⁴C_e represents the two C atoms of BAB belonging to the *endstanding* phenyl rings.

tween the two TBA isomers have been presented, as they arise during time-resolved measurements of the thermal isomerization of the *cis* form (see Fig. 3.2, page 32).

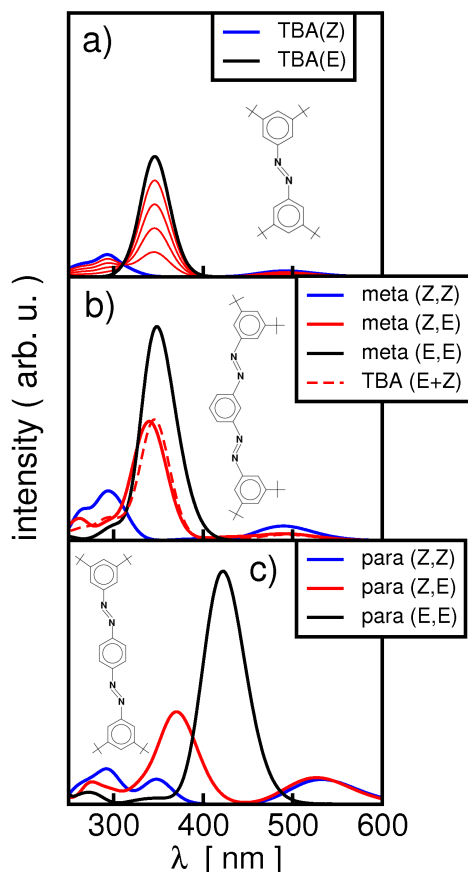


Figure 5.13: UV/Vis spectra calculated with B3LYP/6-311G*: a) TBA molecule, *E* and *Z* in thick lines; thinner lines are the following mixtures $0.2E+0.8Z$, $0.4E+0.6Z$, $0.6E+0.4Z$ and $0.8E+0.2Z$, from top to bottom. b) *meta* substituted TT-BABs in thick lines. The dashed line is the sum E -TBA+ Z -TBA \approx $[E, Z]$ -TT-BAB. c) *para* TT-BABs. All spectra are on the same scale. Molecular structures are given for easier understanding.

In this way one finds an isosbestic point at 315 nm, in qualitatively good agreement with the experimental spectra [113], with few quantitative differences. Theoretical spectra are generally shifted to the red, by about 20-30 nm, for the $\pi \rightarrow \pi^*$, and even more, around 40-60 nm, for the $n \rightarrow \pi^*$ absorption band, as stated in Section 5.4.2. The isosbestic point is shifted, as well, by about 40 nm, relative to the experiment [113].

Let us now consider BABs and first discuss *meta* substitution. In the experiment, after irradiation of *meta* $[E, E]$ -TT-BAB with light of $\lambda = 385$ nm, one obtains a photostationary state with 70% $[Z, Z]$ -, 21% $[E, Z]$ - and 12% $[E, E]$ -isomers, and an isosbestic point at 280 nm [113]. This indicates that these molecules react like TBA itself. In Fig. 5.13 b), calculated spectra of *meta* TT-BAB, for $[E, E]$, $[E, Z]$ and $[Z, Z]$ isomers are shown. The overall shape of the spectra fits reasonably well to the experimental ones [113]. In the case of *meta* substitution, one can notice that the spectra show kind of an additive nature. Namely, combining the spectra of the all-*trans* structure, $[E, E]$ -TT-BAB and the all-*cis* isomer $[Z, Z]$ -TT-BAB, one can almost exactly get the spectrum for the mixed isomer, *i.e.* $[E, Z]$ -TT-BAB. The $[E, Z]$ -TT-BAB spectrum is also obtained, in good approximation, from adding the isolated *Z*-TBA and *E*-TBA spectra of Fig. 5.13 a) (see the dashed line in Fig. 5.13 b)). This is valid for $[E, E]$ -TT-BAB and $[Z, Z]$ -

TT-BAB, as well, where the intensities resemble the additive behavior of *spectral components* of *E*-TBA and *Z*-TBA, respectively.

The additive behavior of spectra doesn't surprise, if one takes a look at frontier orbitals of BABs, presented in Table 5.9. One can see that the HOMO of the *meta* BABs have nodes at two or more C-atoms of the central phenyl ring, isolating the two π systems of the compound "dimer".

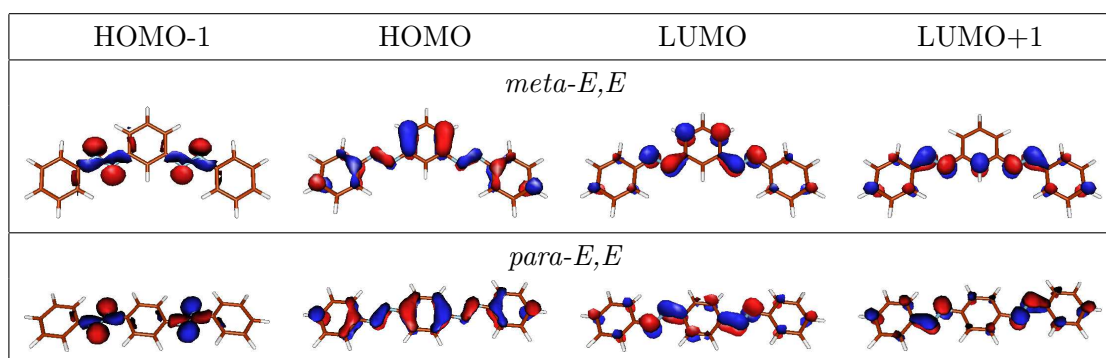


Table 5.9: Kohn-Sham frontier orbitals, calculated with B3LYP/6-31G*, for the [*E*, *E*] isomer of both *meta* and *para* non-alkylated BAB.

On the opposite, the π electrons of all-*trans* *para*-BABs are delocalized over all three benzene rings and the two azo-units. As a consequence, the spectral features of *para* TT-BAB are quite different from the previous case (see Fig. 5.13 c)). A strong red-shift of $\pi \rightarrow \pi^*$ appears in the range of 30 nm for the [*E*, *Z*]-TT-BAB to even 75 nm for the all-*trans* isomer [*E*, *E*]-TT-BAB. The same bathochromic shift, occurs in the experiment, too: By ≈ 15 nm for [*E*, *Z*]-TT-BAB and 40 nm for the [*E*, *E*]-TT-BAB molecules [113]. The $n \rightarrow \pi^*$ transition appears to be shifted in the experiment as well, in the range of 15-20 nm and slightly stronger in theory, by ≈ 30 nm. The smaller shift of the $n \rightarrow \pi^*$ absorption band is due to the fact that n orbitals, corresponding to the lone-pairs of the nitrogen moiety, are not very much affected by conjugation of the substituent in *para* positions. Because of the conjugation, which is much more pronounced for *para* than for *meta* species, one can explain the low photoreactivity of *para* molecules observed in experiment [113]. Because the $\pi \rightarrow \pi^*$ and $n \rightarrow \pi^*$ absorption bands now strongly overlap, excitation leads to an extremely low percentage of the [*Z*, *Z*] isomer in the photostationary state, when starting from [*E*, *E*]. One obtains 4% [*Z*, *Z*], 24% [*E*, *Z*] and 72% [*E*, *E*]

in the photostationary state, and no indication of an isosbestic point, which implies that these molecules behave differently compared to common ABs.

5.5.3 Thermal Ground State Isomerization

The differences between *meta* and *para* BABs become even more obvious when calculating rates for the thermal *cis*→*trans* isomerization, following the path $[Z, Z] \rightarrow [E, Z] \rightarrow [E, E]$. To save computational cost, all molecules were considered without taking bulky *tert*-butyl groups into account. We assume, as before, that the thermal reaction proceeds through a linear TS ($\alpha \approx 180^\circ$), as shown in Section 5.3. As explained in Fig 5.12, for BAB we have four angles α and accordingly, there are four TSs. All the TS converged fully using the QST3 method (B3LYP/6-31G*). Single imaginary frequencies of $\approx i420 \text{ cm}^{-1}$ in the characteristic switching mode, were found. From the TS, we calculated isomerization rates in the same way as in Section 5.2, using Eyring TS theory. These are summarized in Table 5.10 and demonstrated with schemes in Figs. 5.14 and 5.15.

	$[Z, Z] \rightarrow [E, Z]$		$[E, Z] \rightarrow [E, E]$	
BAB	k_1 [s ⁻¹]	k'_1 [s ⁻¹]	k_2 [s ⁻¹]	k'_2 [s ⁻¹]
<i>meta</i>	2.06×10^{-5}	1.73×10^{-4}	4.56×10^{-5}	7.59×10^{-5}
<i>para</i>	2.68×10^{-5}	1.93×10^{-3}	2.79×10^{-5}	1.24×10^{-2}

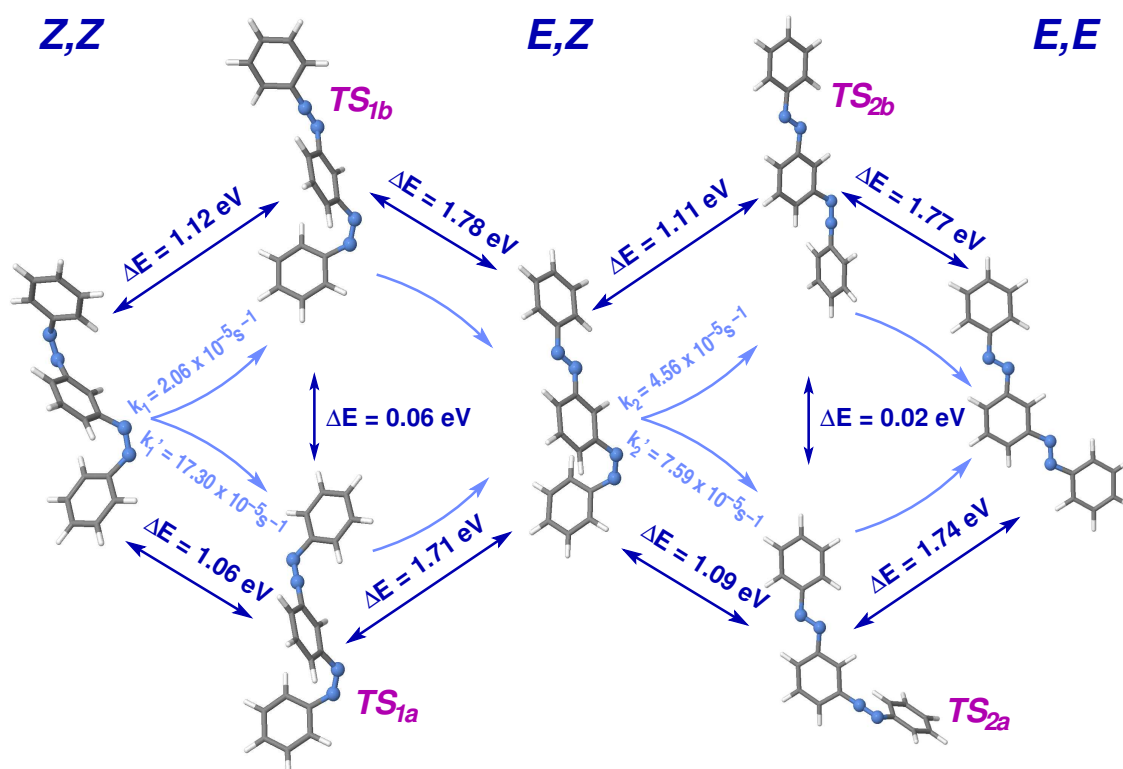
Table 5.10: Tabulated data for the two reaction steps $[Z, Z] \rightarrow [E, Z]$ and $[E, Z] \rightarrow [E, E]$ of *meta* and *para* substituted BABs. The rates were evaluated at $T = 298.15 \text{ K}$. The rates k_1 , k'_1 , k_2 and k'_2 are defined in Figs. 5.14 and 5.15.

For *meta*-BAB, the computed isomerization rates are quite similar to the ones of the parent AB molecule, see Table 5.2. This is also valid for activation energies. For instance, if the isomerization process $[Z, Z] \rightarrow [E, Z]$ proceeds through a TS_{1b} (see Fig. 5.14) with a linearized α_1 , *i.e.* linear C_e-N-N units (see Fig. 5.12), then $k_1 = 2 \times 10^{-5} \text{ s}^{-1}$ with a classical activation energy ΔE_{el}^\ddagger of 1.12 eV. The following reaction, $[E, Z] \rightarrow [E, E]$, is over linearized α_4 (TS_{2b}), with a rate $k_2 = 5 \times 10^{-5} \text{ s}^{-1}$ and $\Delta E_{el}^\ddagger = 1.11 \text{ eV}$. The isomerization can also proceed over linear α_2 and α_3 angles, *i.e.*, over linear N-N-C_e units (Fig. 5.12). One notices that kinetic parameters

change only moderately compared to the former case. We have $k'_1 = 17 \times 10^{-5} \text{ s}^{-1}$ and $k'_2 = 8 \times 10^{-5} \text{ s}^{-1}$, with activation energies of 1.06 and 1.09 eV, respectively.

Conjugation with azophenyl group is more pronounced for *para*-BABs. Here, thermal isomerization can proceed by several orders of magnitude faster. Fig. 5.15 displays the four different TSs for this case. Two of them are for the $[Z, Z] \rightarrow [E, Z]$ (TS_{1a}, characterized by linear α_2 and TS_{1b}, defined by linear α_1), and another two for the $[E, Z] \rightarrow [E, E]$ reaction (TS_{2a}, characterized by linear α_3 and TS_{2b}, defined by linear α_4). It is found that the reaction would run faster along the "lower" reaction path, see Fig. 5.15, over TS_{1a} and TS_{2a} (both characterized with the linear-center N-N-C_c), with rates $k'_1 = 2 \times 10^{-2} \text{ s}^{-1}$ and $k'_2 = 12 \times 10^{-3} \text{ s}^{-1}$, respectively, both at room temperature. The "upper" path through TS_{1b} and TS_{2b} shows slower rates which are similar to those of AB, being around $\approx 3 \times 10^{-5} \text{ s}^{-1}$.

In summary, the TSs are stabilized and the rates enhanced for *para*-BAB. This is particularly pronounced by isomerization over the linear-center, *i.e.* the central N-N-C_c units in *para*-BAB. This can be understood from the fact that a π -electron accepting group, such as azo-phenyl, when in *para* position of the central phenyl, stabilizes a linear TS.



meta-BAB

Figure 5.14: Schematic representation for *meta*-BAB for the thermal isomerization $[Z, Z] \rightarrow [E, Z] \rightarrow [E, E]$. For BABs, four different TSs can be defined which means that molecules can isomerize as follows: *TS*_{1b}-*TS*_{2b}, *TS*_{1b}-*TS*_{2a}, *TS*_{1a}-*TS*_{2b} and *TS*_{1a}-*TS*_{1b}. The upper path follows simultaneous change of ω together with the linearization of the outer angle α (C_e -N-N unit). In the lower part, the stepwise isomerization with linearization of the inner lying angle α (C_c -N-N side). Every isomerization step proceeds with a certain rate. Characteristic electronic energy differences, ΔE , between stationary states are presented as well. We note that *TS*_{1a} is 0.06 eV more stable in energy than *TS*_{1b}, and *TS*_{2a} is 0.02 eV more stable in energy than *TS*_{2b}.

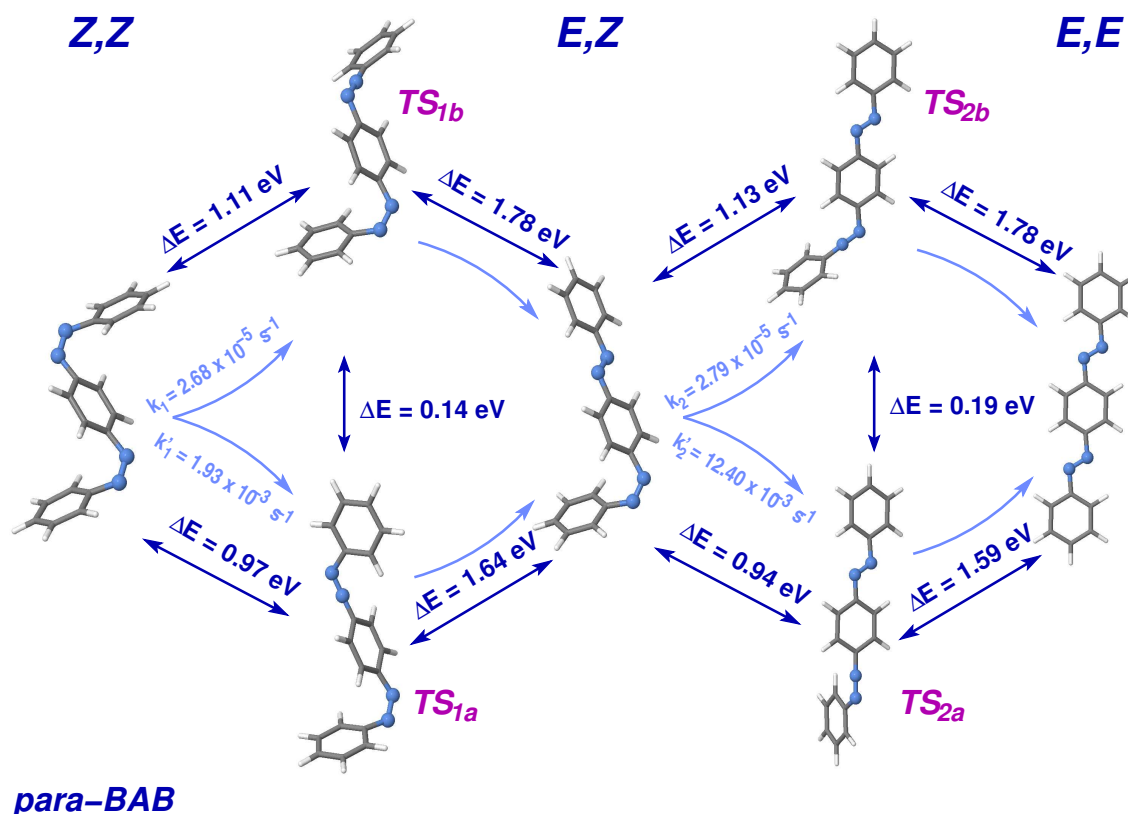


Figure 5.15: Scheme of *para*-BAB for the thermal isomerization $[Z, Z] \rightarrow [E, Z] \rightarrow [E, E]$. For BABs, four different TSs can be defined which means that molecules can isomerize as follows: TS_{1b} - TS_{2b} , TS_{1b} - TS_{2a} , TS_{1a} - TS_{2b} and TS_{1a} - TS_{1b} . As in Fig. 5.14, the upper part follows the isomerization over the outer positioned α angle (C_e -N-N side) and the lower part shows changes over the inner one (C_c -N-N). Contrary to the previous case, the bottom part represents kinetics that are nearly hundred times faster than the top ones (compared to *meta* also). We note, as for *meta*-BABs (Fig 5.14), that TS_{1a} is 0.14 eV more stable in energy than TS_{1b} , and TS_{2a} is 0.19 eV more stable in energy than TS_{2b} .

5.6 Isomerization of Imines

5.6.1 N-benzylideneaniline

Derivatives of N-benzylideneaniline, henceforth called NBA, will be studied mostly because of their ability to isomerize in the same way as ABs [84]. Replacing one of the N atoms by a CH group, a Schiff base with a HC=N unit is created instead of an azo moiety like in AB molecules. Of course, these systems are possible candidates for molecular switches, too.

In the lower part of Fig. 5.16 stationary points of the NBA molecule are given, calculated with B3LYP/6-31G*. The rotational angle ω and inversion angle α are defined as for the AB molecule (see Figs. 3.1 and 5.16).

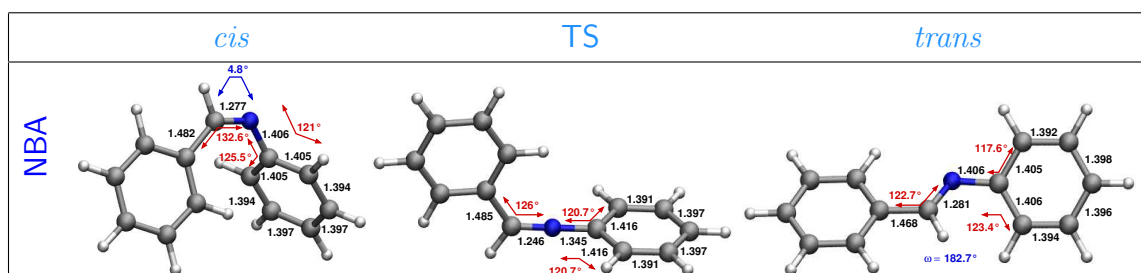


Figure 5.16: Geometries of NBA molecule for stationary points being discussed in this work. The *cis* form isomerizes thermally over the TS to the energetically more stable product, the *trans* isomer. Here, geometry parameters are presented: In blue, ω values, in red, angles α . Angles are given in degrees and bond distances in Å. All the presented data are obtained with B3LYP/6-31G*.

Also, similar to AB, the *trans* conformer is more stable than the *cis* one by 0.28 eV (B3LYP/6-31G*). The former has a $|\mu_{tot}| = 1.43$ D, which is due to the Schiff base in the molecular center, and the latter has a total dipole moment $|\mu_{tot}| = 2.60$ D. For NBA we also calculated a fully relaxed PES along ω and α , given in Fig. 5.17. The topology of the surface is exactly the same as that of ABs with two following characteristics: (i) The activation energy for the thermal isomerization is much lower than for AB with $\Delta E_{el}^\ddagger = 0.59$ eV, and (ii) the pure rotation along ω shows a large barrier of ≈ 1.6 eV with a peak at $\approx 90^\circ$. The same findings are reported in Ref. [105], proving that rotation is not an energetically suitable isomerization path in the ground electronic state S_0 . However, the classical activation barrier is lower

than the one of 0.71 eV found by Asano *et al.* [94] calculated using MP2/3-21G, thus being closer to the experimental estimate of 0.73 eV [115]. We note here that the TS for thermal isomerization of NBA is linear, similar to the one of AB (see Fig. 5.16 in the middle).

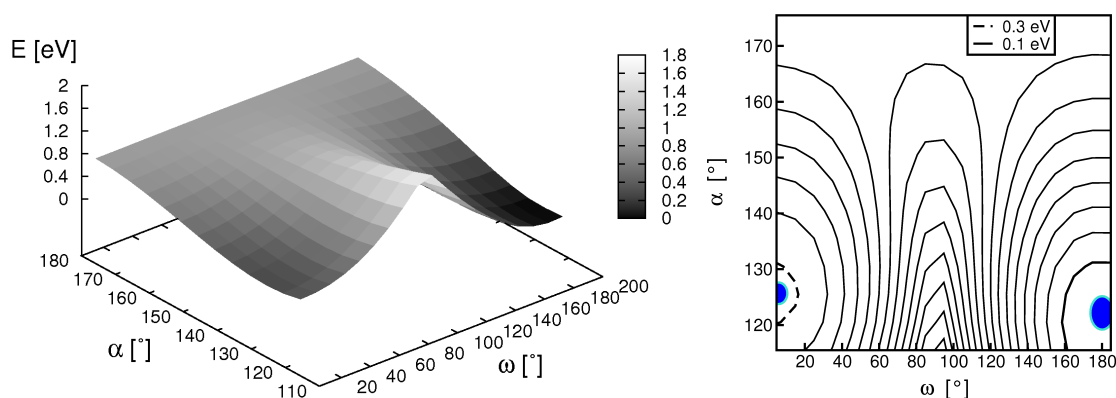


Figure 5.17: Fully relaxed PES of the NBA molecule, obtained with B3LYP/6-31G*. The rotational path, over ω , was calculated with a 10° step while a 5° step was chosen to cover the inversion path over the angle α ; 247 points were calculated in total. On the right hand side, contour plots separated by 0.10 eV starting from the *trans* minimum, marked with the blue spot at $\omega = 180^\circ$.

5.6.2 Thermal Isomerization of Imines

Concerning thermal isomerization of imines, it is known that the isomerization rates are much faster than the ones of AB. For deposition of these molecules on metal substrates, a system that contains bulky groups was synthesized analogous to the TBA, *i.e.*, an NBA with four *tert*-butyl groups in 3,3',5 and 5' positions, called TBI [116]. Additionally, NBA derivatives containing -CN and -CH₃ groups in *para* positions have been introduced, too.

These systems are similar to ABs in the sense that they all have a linear TS for the thermal ground state isomerization, however, with a different single imaginary frequency of $\approx i240 \text{ cm}^{-1}$. The linear CNC moiety is energetically more favorable than the linear CCN units which results in lower activation energies for thermal *cis*→*trans* isomerization, being almost two times smaller than for the corresponding AB molecules (see Table 5.11). The difference in pure electronic energies of the *cis*

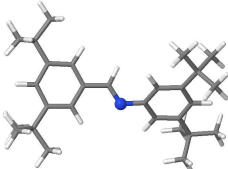
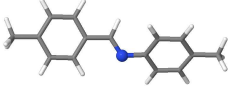
molecule	ΔE_{el}^\ddagger	ΔE_{ct}	$k_{c \rightarrow t, 298.15K}$	A	ΔS^\ddagger	$\Delta H_{298.15K}^\ddagger$
NBA 	0.59	0.28	5.43×10^3	4.81×10^{12}	-2.68	0.54
TBI 	0.61	0.28	9.14×10^3	1.44×10^{13}	6.54	0.55
DMNBA 	0.61	0.29	3.50×10^3	5.94×10^{12}	-1.05	0.55
CI 	0.50	0.28	9.58×10^4	3.83×10^{12}	-5.01	0.46

Table 5.11: Energetic and kinetic data for the ground state isomerization of the NBA molecule and its derivatives. Energies are given in eV, rates and prefactors in s^{-1} and activation entropies in $J/K \cdot mol$.

isomer and TS are about 0.60 eV lower than the ones previously discussed. Even though the *tert*-butyl group is a weak electron donor, its positioning in *meta* reduces the activation barrier as well. Calculated Arrhenius prefactors are comparable to those of AB derivatives. The overall kinetic rates are, as a consequence of smaller activation energies, larger than those of common ABs. The *para* substitution with -CN shows a large influence, accelerating the rates to nearly twenty times compared to the non-substituted molecule.

The energy difference between the TS and the *trans* isomer (the reaction energy ΔE_{ct} reduces as well) is also more than two times smaller than the one of AB. This implies that the thermal *trans* \rightarrow *cis* isomerization is also possible for imines. The rate is, for example, $k_{t \rightarrow c} = 7.28 \times 10^{-2} s^{-1}$ at room temperature, thus, even faster than the thermal *cis* \rightarrow *trans* isomerization of AB.

5.7 Summary

In this and previous Chapters 3 and 4, ABs as molecular switches were studied, mostly from a quantum chemical perspective. The focus was switching of molecules in the gas phase and in solution, however, also with implications for excited-state switching, resonance switching, static electric field effects and switching at surfaces.

Specifically, in Chapter 5, we presented an extensive study, covering over 90 AB derivatives that were studied with DFT methods, including PCM in order to compare recent experimental results with theoretical data in solvents. We described the kinetics of these systems in the framework of Eyring TS theory in the case of thermal ground state isomerization. In most cases the thermal isomerization runs over a linear TS. It has been proven, that a change of the reaction mechanism occurs for *push-pull* molecules in polar solvents from an inversion to a rotation pathway. Studying bulky molecules, the rates and activation barriers are comparable to experiments, but calculated Arrhenius prefactors are still somewhat too high. The entropies are large and positive, contrary to experimental findings. For these molecules it is possible that explicit treatment of solvent molecules needs to be taken into account. Conjugated ABs, so-called BABs, were also studied. The *meta* substitution of H by an azo-phenyl group doesn't influence AB a great deal and the new molecules show properties similar to mixtures of *trans* and *cis* species. In the case of *para* substitution, however, the chromophore is extended, coupling strongly to the backbone of the AB molecule. Hence, the *para*-BABs don't resemble ABs anymore and new spectroscopic and kinetic properties emerge. At last, we introduced imines, which switch much faster than ABs (in both directions), at least in the gas phase.

Chapter 6

1,5-Cyclooctadiene@Si(001)

6.1 General and Experimental Findings

So far only gas phase molecules of an AB backbone and its possible interaction with an environment have been discussed. Metal surfaces, on which these switches can be adsorbed, were not explicitly included and only discussed in a qualitative fashion. Organic functionalization of semiconductor surfaces is another promising path towards new technological applications and molecule-scale devices [117, 118, 119]. Wolkow [120] summarized the basic principles for functionalizing semiconductor surfaces and controlling adsorption of alkenes, polyenes and benzene on silicon surfaces, for designing new molecular switches.

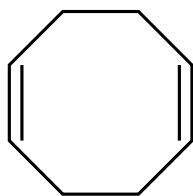


Figure 6.1: Structural formula of 1,5-cyclooctadiene.

One of the most demanding challenges for the future is getting ordered monolayers of molecules at surfaces in a controlled way that can be used for technological applications [121, 122]. A long-term goal is to couple conventional semiconductors linked to molecules with new functionalities. One of these properties would be to have a bistable molecule that can be switched from one form to another stable conformation by an external stimulus.

A molecule of interest in this work is 1,5-cyclooctadiene, a cyclic diene with the chemical formula C_8H_{12} (see Fig. 6.1). The commonly used abbreviation is COD and will be used from now on throughout the chapter. Motivated by experiments performed on silicon wafers, on which COD molecules have been evaporated in Ref. [20], we calculated the COD molecule on Si(001), using a cluster model approach. For this system, to determine the electronic structure, it has been shown that the cluster approach delivers results comparable to periodic DFT calculations [123, 124], confirming that adsorption is quite localized. At the same time, saving computational cost is an advantage of the cluster model. It should be emphasized, though, that comparison of periodic and cluster model optimizations is only valid when low-coverage adsorption is investigated [124].

Silicon belongs to the 4th group of the periodic table of elements, having four valence electrons. The diamond-like crystal lattice of Si is shown in Fig. 6.2. Cutting the crystal along the (001) surface plane, each of the surface atoms formally has two half occupied orbitals which then bond, over adjacent atoms, giving Si dimers. These can be tilted, creating in this way so-called D_{up} and D_{down} orbitals, which are formally occupied with two electrons (D_{up}) or empty (D_{down}), see Fig. 6.2 (right) [125, 126, 127, 128]. This surface reconstruction leads to the minimization of the total free energy of the system. In the case of the Si dimer the lowering of the energy for the system is about 2 eV [129]. The Si(001) surface can adopt a $p(2\times 1)$ reconstruction, as well as $c(4\times 2)$ and $p(2\times 2)$ reconstructions [130, 127, 131]. In our work, only the $p(2\times 1)$ reconstruction has been considered, which is shown in Fig. 6.3 (left) - the $c(4\times 2)$ surface is shown on the right.

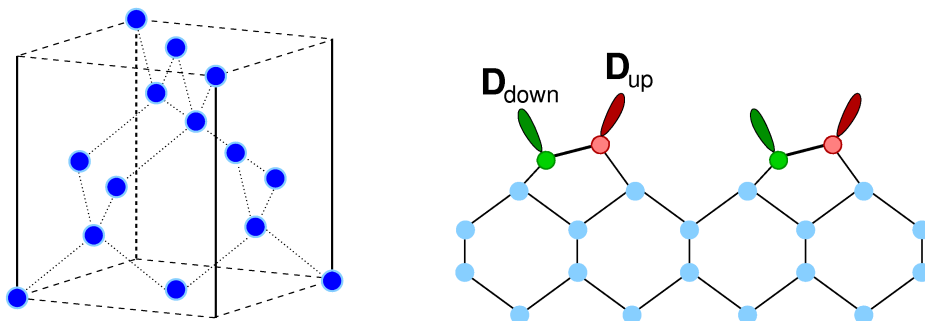


Figure 6.2: On the left hand side, the crystal lattice of silicon and, on the right, a scheme representing the dimer tilting surface, are shown.

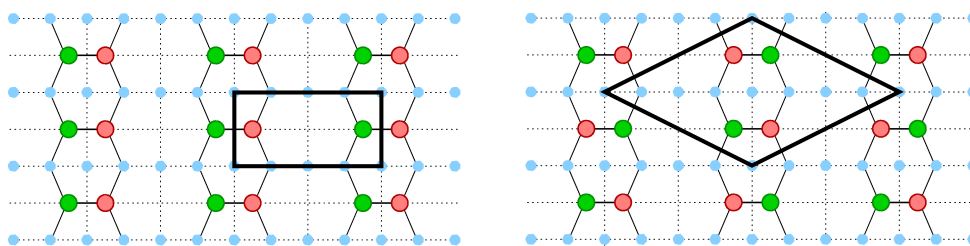


Figure 6.3: Si(001) surface: On the left hand side the $p(2\times 1)$ reconstruction and on the right, the $c(2\times 4)$ structure is shown. Red and green symbols denote Si atoms of Si dimers; the black lines enclose the respective elementary cell.

The adsorption of COD@Si(001) has been described as a reaction between a single dimer and one of the double bonds of the molecule [132]. During the process the π bond of the unsaturated hydrocarbon interacts with the dangling bonds of the Si dimer. Latest experiments acknowledge the existence of two kinds of COD adsorption structures at Si(001), namely a “*bridge*” and “*upright*” structure, see Fig. 6.4.

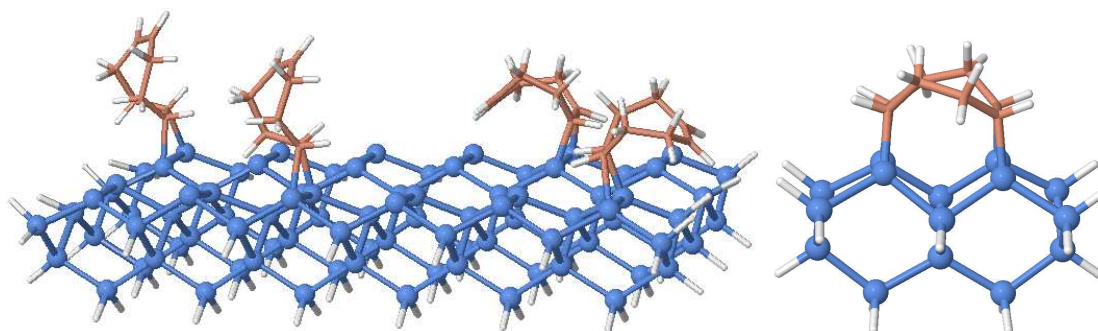


Figure 6.4: On the left, pictorial representation of various “*upright*” structures at Si(001) are shown, and on the right, we present the “*bridge*” adsorption of COD on a H-saturated Si_{15} cluster. See text below.

The most interesting result (for the “*bridge*” structure), is the reversible switching between two degenerate conformers observed in low-temperature STM (LT-STM) experiments [20]. The process was attributed to inelastic electron tunneling (IET), at low temperatures. At 5 K, the switching rate R was measured at positive and negative bias voltages (Fig. 6.5, left). This implies the possibility that both anion or cation resonance states can be involved in the switching process. It was also shown that the rate depends linearly on the mean tunneling current with a slope close to

1, which indicates that a single-electron excitation process triggers the switching. At higher temperatures, a crossover temperature behavior was found between IET-driven and thermally activated switching (Fig. 6.5, right) [25].

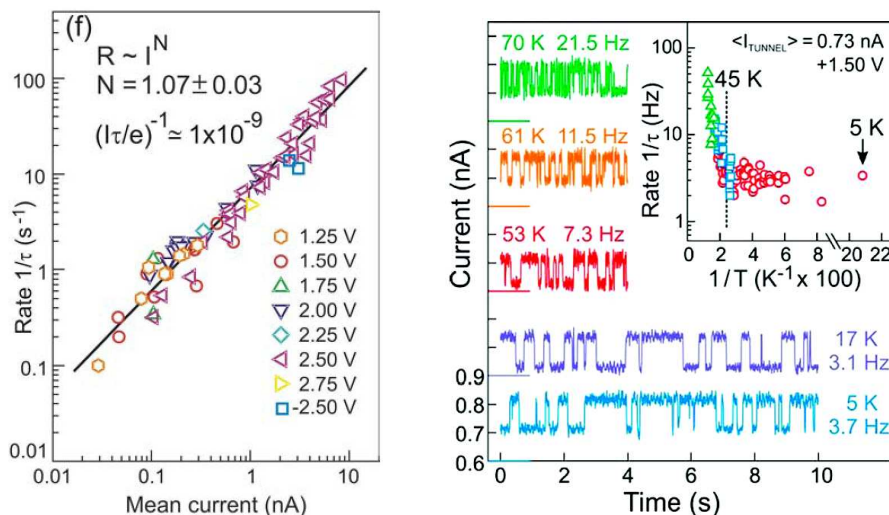


Figure 6.5: Low-temperature STM (LT-STM) experiments on COD@Si(001) [20, 25]: On the left hand side, the dependence of the switching rate on the mean tunneling current is shown (see text). On the right, the tunneling current vs. time, recorded at constant tip height of an STM is given. The "up-and-down" behavior indicates the switching between two stable conformers. The inset gives a logarithmic plot of the switching rate vs. reciprocal temperature, indicating a crossover behavior at $T = 45$ K. Color code and different symbols correspond to different experimental runs probing different molecules.

In upcoming sections, the STM-induced conformational switching of the molecule on Si(001) will be considered. We will first study the adsorption energetics and PES by quantum chemical calculations (Section 6.2), and then the switching dynamics by wave packet methods (Section 6.3).

6.2 Quantum Chemical Calculations

6.2.1 The Free COD Molecule

At first geometries and characteristics of the gas phase COD molecule will be considered. The *twisted boat* is found to be the most stable structure of the compound [133].

Varying dihedral angles between the numbered atoms $C_2C_3C_4C_5$, called d_1 in the following, and the second dihedral angle between atoms $C_6C_7C_8C_1$, denoted as d_2 , the reaction path for the isomerization was calculated using B3LYP/6-31G* (see Fig. 6.6). The path is shown for $d_1 = d_2$, *i.e.*, simultaneous motion of the two dihedrals. All other degrees of freedom were optimized.

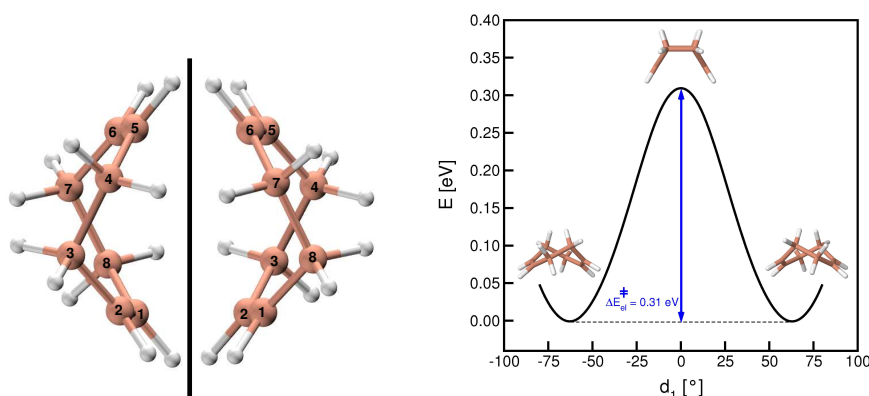


Figure 6.6: On the left hand side, non-superimposable mirror images for the two degenerate structures of the COD molecule are presented; on the right hand side the calculated reaction path for the COD isomerization is shown as a one-dimensional plot along the reaction coordinate d_1 ($= d_2$) (dihedral angle between atoms $C_2C_3C_4C_5$). The calculations were done with B3LYP/6-31G*.

The path runs from degenerated minima at $\approx \pm 60^\circ$ through a symmetrical TS at $\approx 0^\circ$. For the latter a single imaginary frequency of $i151.6 \text{ cm}^{-1}$ was found. The same structure of the TS was confirmed using the QST3 method, see Fig. 6.6. Geometrical data are collected in Table D.1 (Appendix D) and are in good agreement with other available data [133, 134]. Stationary points, minima and corresponding TS, were calculated with a bigger basis set, as well, which we show in Table 6.1. The activation barrier ΔE_{el}^\ddagger is 0.311 eV for the 6-31G* basis set and is lower by only $6 \cdot 10^{-3} \text{ eV}$ when applying the 6-311G** basis set.

Recent theoretical work, given in Ref. [133], delivers a barrier value of 0.258 eV. There, the structures were calculated with HF/6-31G*, and energies were subsequently corrected with single point MP2/6-31G* calculations.

Basis Set	Structure	Energy (E_h)	ΔE_{el}^\ddagger (eV)
6-31G*	min	-312.030388	
	TS	-312.018974	0.311
6-311G**	min	-312.114253	
	TS	-312.103386	0.296

Table 6.1: Energetic data for the switching of COD molecules; ΔE_{el}^\ddagger is the classical activation energy of the switching process.

6.2.2 Adsorption of COD on Si Dimer(s)

We now study the adsorption of COD on a single Si dimer. Previous theoretical work, based on periodic DFT calculations, shows that the *bridge* structure is the most stable adsorption geometry [123], see Fig. 6.4 (right). The results of Nacci *et al.* [20] reveal that, in fact, both *bridge* and *upright* structures occur at the surface in the case of the low coverage (10^{13} molecules /cm², or 3% of the Si dimer surface density), with the *bridge* structure as the dominant one.

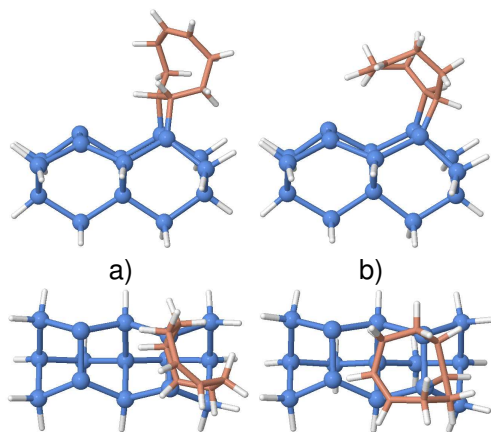


Figure 6.7: Optimized *upright* structures of the COD@Si(001): a) Similar geometry to the one calculated by Cho *et al.* [123] and b) Another possible, *bended* orientation for the COD molecule reacting with a single double bond with the substrate.

For *upright* adsorption, we performed DFT calculations using B3LYP/6-31G*, on a single dimer using a small cluster, with nine Si atoms (not shown), as well as a larger cluster with 15 silicon atoms. The non-surface Si atoms were saturated with H atoms. The larger cluster itself is shown in Fig. 6.7. Details about the geometry of the COD@Si₁₅ cluster and *upright* adsorption are reported in Appendix D. For the *upright* adsorption, we find two structures of which one is similar to the upright form calculated by Cho and co-workers by periodic DFT [123], and is shown in Fig. 6.7 a). The second *upright* structure, here called *bended*, looks somewhat similar to the *bridge* type (see below), however, retaining the second double bond intact (see Fig. 6.7 b)). Upright structure a) is

0.406 eV more stable than the b) form at the B3LYP/6-31G* level of theory. If one saturates the second dimer with hydrogen (all Si atoms are H-saturated), this difference raises to 0.487 eV, as shown in Appendix D (page 147). In this Appendix (Table D.2) also further structures are shown. Not all of these structures are expected for a periodic surface, but are partially due to the finite cluster model. For the smaller cluster with 9 Si atoms, which has only one Si-dimer, the energy difference between the two *upright* structures a) and b) is only 0.246 eV. Since the smaller cluster has no second highly reactive Si-dimer this difference can be easily understood. The two fully optimized minima of the *upright* form at Si(001) can provide an explanation for fluctuations that can be seen during an STM scan in experiment [20]. In fact, our calculations suggest that there are several stable structures, not only a single *upright* and a *bridge* structure, as previously suggested [123].

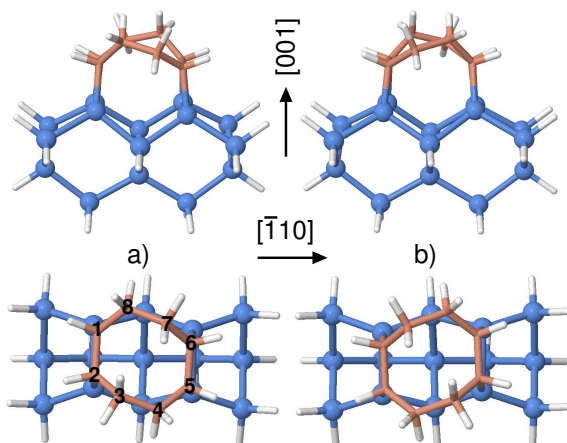


Figure 6.8: Stick-and-ball models of the side and top views of the "bridge" COD@Si(001) optimized cluster where a) and b) mark the enantiomers. Numbering of COD carbon atoms used for PES calculations on the lower left top view is also shown.

In the same work it was argued that the *bridge* configuration is ≈ 0.90 eV more stable than the *upright* structure. The stability of the latter structure is reduced because of the presence of a free π bond which is more energetic than the reacted one. Here, the *bridge* form was calculated on a H-saturated 15 atom Si cluster, shown in Fig. 6.8 and in Fig. 6.4 (right), with the same method as before. From Fig. 6.8 it is also seen that two degenerate conformations exist for COD on Si(001), a) and b), similar to the case found for free COD. In our calculations, the *bridge* form is ≈ 0.76 eV more stable than the lowest energy of the *upright* form (listed in Table D.2), and also shown in Fig. 6.7 a).

6.2.3 Two- and One-Dimensional Potential Energy Surfaces

In order to get information about the switching rates, it is necessary to calculate the PES for the process along relevant reaction coordinates, for the *bridge* form, which is given in Fig. 6.9. We chose the two degrees of freedom considered to be most important for the interconversion of enantiomers at the surface. These are the two dihedral angles defined between the numbered atoms C₂C₃C₄C₅ (also d_1), and the second dihedral angle, between atoms C₆C₇C₈C₁ (also d_2), *i.e.*, the same as we had for the free COD molecule, see Fig. 6.9 (right). The PES was calculated using the B3LYP functional and the 6-31G* basis set, with a 10° step for both coordinates, and the Si₁₅ cluster shown in Fig. 6.8. The lowest two layers on the

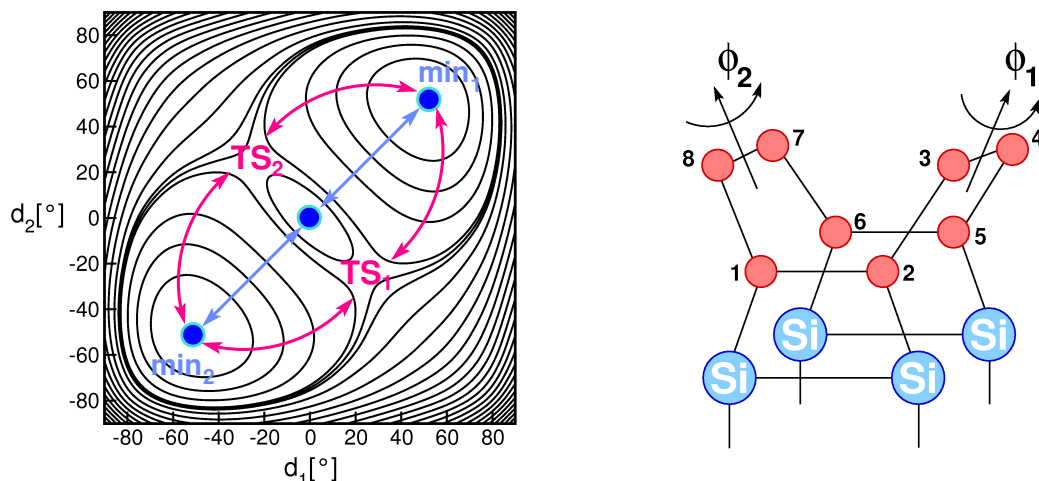


Figure 6.9: Left panel: contour plots of the calculated PES separated by 40 meV; the 1D path is marked in blue, connecting both minima over the 2nd order TS. In red, the arrows point towards the two degenerated TSs. The right panel shows the labeling of atoms used in this work (see text). Si atoms are given in blue and C atoms in orange.

cluster were fixed. Freezing upper atoms of the Si-cluster was impossible because of their rather unremarkable but relevant movement during the COD switching. Thus, we reoptimized all other coordinates (Si, H of the first surface layer, and COD atoms) for a given point (d_1 , d_2). All Si atoms are hydrogen saturated, *i.e.*, a system of 51 atoms in total was treated.

The PES has two minima belonging to two degenerate enantiomer structures: (*i*) The first one at dihedral angles d_1 and d_2 of $\approx 50^\circ$, and (*ii*) the second one with values of d_1 and d_2 of $\approx -50^\circ$. On the PES, two degenerate TSs are seen as well: (*i*)

The first one at $d_1 = 25^\circ$ and $d_2 = -25^\circ$ and (ii) the second one $d_1 = -25^\circ$ and $d_2 = 25^\circ$. The frequency analysis of these points delivers a single imaginary frequency of $i108 \text{ cm}^{-1}$.

Approximating the switching as a 1D process by introducing the restriction $d_1 = d_2$, the path leads over a local maximum at $d_1 = d_2 = 0^\circ$. While this geometry does not correspond to a true TS in the 2D model, the geometry is very symmetrical resembling the structure of the TS for the gas phase COD. For this point normal mode analysis showed two imaginary frequencies of $i83.6 \text{ cm}^{-1}$ and $i152.1 \text{ cm}^{-1}$, corresponding to a 2nd order TS. In a strictly 1D model, however, with $d_1 = d_2$ this point corresponds to a TS connecting the two equivalent enantiomers. The corresponding potential curve $V(d_1)$ and the characteristic geometries are shown in Fig. 6.13, left. The barrier between the minima and the TSs is smaller than in the gas phase, 170 meV. In Fig. 6.13, right, we show another 1D path with the choice $d_1 = -d_2$, which connects the two TSs and goes through the 2nd order TS. It is seen that the energy difference is just 9 meV between the first order saddle points and the 2nd order TS.

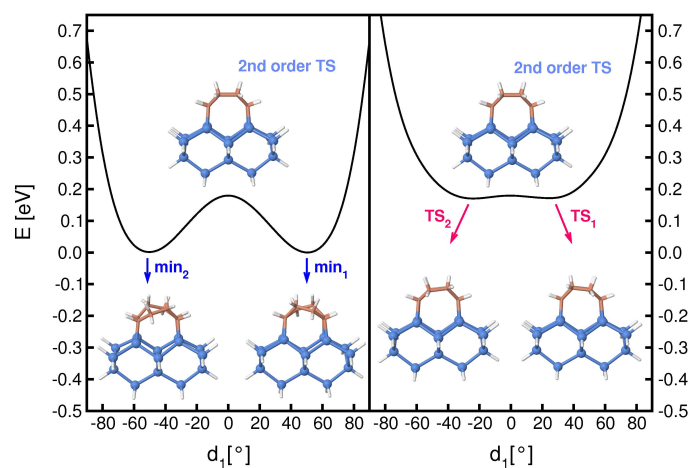


Figure 6.10: 1D cuts of the calculated PES $V(d_1, d_2)$ shown in Fig. 6.9. On the left we show the 1D reaction path indicated in blue in Fig. 6.9 (*i.e.*, along the line $d_1 = d_2$), and on the right we show a 1D path along the line $d_1 = -d_2$, connecting the 2 TS, TS_1 and TS_2 .

6.2.4 Thermal Isomerization of COD@Si(001)

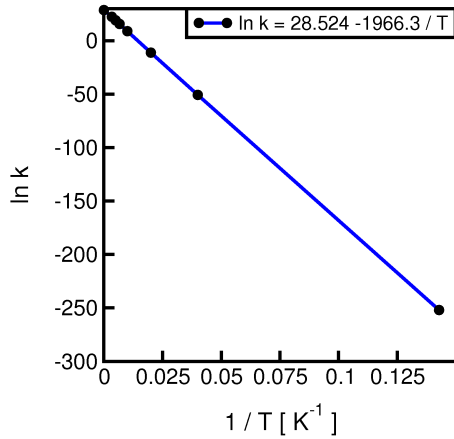


Figure 6.11: Arrhenius plot for thermal switching of COD@Si(001) (points) with a linear fit (blue line).

From known TSs and minima, thermal switching rates $k(T)$ can be calculated from Eyring TS theory (see Section 5.2). Here, we used an approach different to the one described in Eq.(5.4). Instead, thermochemical data were recalculated at every temperature, giving an activation free energy of $\Delta G^\ddagger = G^\ddagger - G^{min}$ (the energy difference between TS and the minimum). In Fig. 6.11, a linear dependence of the logarithm of the rate constant as a function of inverse temperature is found. Plotted rates are reported in Table 6.2.4. From the Arrhenius equation (page 60), one finds a prefactor of $A = 2.44 \times 10^{12} \text{ s}^{-1}$ for the process and an activation energy of $E_a = 169 \text{ meV}$, which fits to the electronic energy difference between TSs and minima. The rates are pretty high at room temperature, which is due to the very shallow energy barrier. At low temperatures, however, the rates are vanishingly small. In particular that is for temperatures around 5 K for which the LT-STM switching experiments have been carried out [20]. Therefore, in this temperature regime the switching cannot be thermal and must be due to other mechanisms, *e.g.* inelastic electron tunneling (IET) [20, 25].

T [K]	ΔG^\ddagger [kJ/mol]	ln k	k [s ⁻¹]
7	16.165	-252.04	3.47×10^{-110}
25	16.168	-50.80	8.64×10^{-23}
50	16.178	-11.24	1.31×10^{-5}
100	16.262	8.81	6.67×10^3
150	16.457	15.58	5.81×10^6
200	16.753	18.98	1.76×10^8
298.15	17.819	22.27	4.69×10^9

Table 6.2: Thermal switching rates and activation free energies for COD@Si(001), obtained from Eyring TS theory.

6.2.5 New Coordinates

For the purpose of dynamical simulations, the PES needs to be expressed in angles as reaction coordinates instead of dihedral angles. Namely, looking at the calculated surface, conformational changes are involving both coordinates. It is more convenient to describe the switching process with decoupled coordinates. For this purpose, we introduce two switching angles ϕ_1 and ϕ_2 as shown in Fig. 6.9 (right panel). It is found by geometrical arguments and numerical investigation (not shown here), that the angles ϕ_1 and ϕ_2 are approximately proportional to the dihedrals d_1 and d_2 , and can be expressed as

$$\phi_1 = \frac{d_1 \cdot \pi}{180^\circ \cdot 2.75}, \quad \phi_2 = \frac{d_2 \cdot \pi}{180^\circ \cdot 2.75}. \quad (6.1)$$

In Eq.(6.1), the ϕ_i are given in radians while the d_i are expressed in degrees. The second step is to symmetrize the surface by introducing two new coordinates, ϕ_p , connecting two minima, and ϕ_n , considering points perpendicular to ϕ_p , normal to the minima and joining degenerated TSs over the PES-maximum:

$$\phi_p = \frac{1}{2} (\phi_1 + \phi_2), \quad \phi_n = \phi_1 - \phi_2. \quad (6.2)$$

The 2D PES in the new coordinates ϕ_p and ϕ_n is shown in Fig 6.12. We note that the calculated surface is given in the range $[-90^\circ, 90^\circ]$, while the symmetrized surface, which covers a larger configuration space, is interpolated over calculated points and quadratically extrapolated [58].

6.2.6 Anionic and Cationic Surfaces

For the dynamical calculations below, it will be assumed that in the STM-induced switching either a "hole" or an "electron" is temporarily attached to the neutral ground state, forming a positive or a negative ion resonance. Therefore, "anionic" and "cationic" PES are needed, which will be estimated from Koopmans' theorem by removing an electron from the HOMO, and attaching an electron to the LUMO, respectively, *i.e.* $E_+ = E_{neutral} - \varepsilon_{HOMO}$ and $E_- = E_{neutral} + \varepsilon_{LUMO}$.

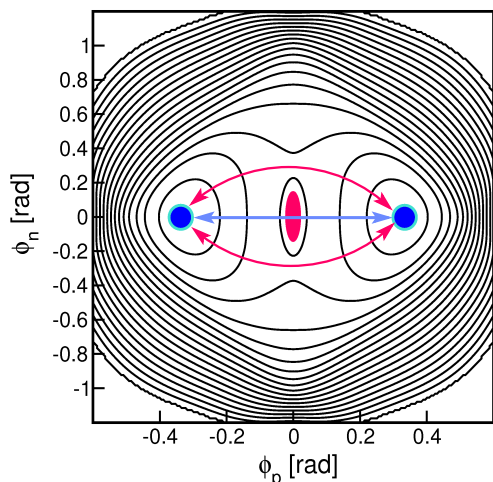


Figure 6.12: Contour plots, separated by 68 meV, of the symmetrized PES along two new reaction path coordinates, the two angles ϕ_n and ϕ_p . As in Fig. 6.9, the blue arrow connects minima and 2nd order TS, while the red arrows describe the paths over minima and first order saddle points.

For the neutral, cationic and ionic surfaces, expressed in ϕ_p and ϕ_n coordinates, a normal mode analysis can be carried out for all stationary points (*i.e.* minima, 2nd order TS and first order saddle points (TSs)), using the method described in Appendix E. All frequencies are given in Table 6.3.

PES	min [cm^{-1}]	max [cm^{-1}]	TS [cm^{-1}]
neutral	237.2	$i129.1$	161.9
	282.7	$i261.4$	$i199.1$
anion	287.9	$i123.4$	165.8
	322.5	$i246.2$	$i202.4$
cation	239.4	$i88.6$	159.0
	275.9	$i243.4$	$i184.3$

Table 6.3: Frequencies (in cm^{-1}) of the symmetrized PES for the neutral COD@Si(001), anionic and cationic surfaces. Analyzing the points of interest, normal mode analysis (described in Appendix E) delivers two characteristic frequencies. Minima have only real frequencies, the 2nd order TS has two imaginary frequencies, while the TS show a single imaginary frequency.

From the Table 6.3, we note the following:

- (i) For the minima, two similar frequencies around 200-300 cm^{-1} are found.
- (ii) The cationic frequencies are very similar to the neutral state frequencies, while the vibrations become significantly "harder" (by $\sim 50 \text{ cm}^{-1}$) in the anion state.
- (iii) The imaginary frequencies at TSs are in the range of $\sim i100-i250 \text{ cm}^{-1}$.

In passing we remark that these frequencies deviate a bit from the quantum chemical calculations of the full clusters, as described in Section 6.2.3.

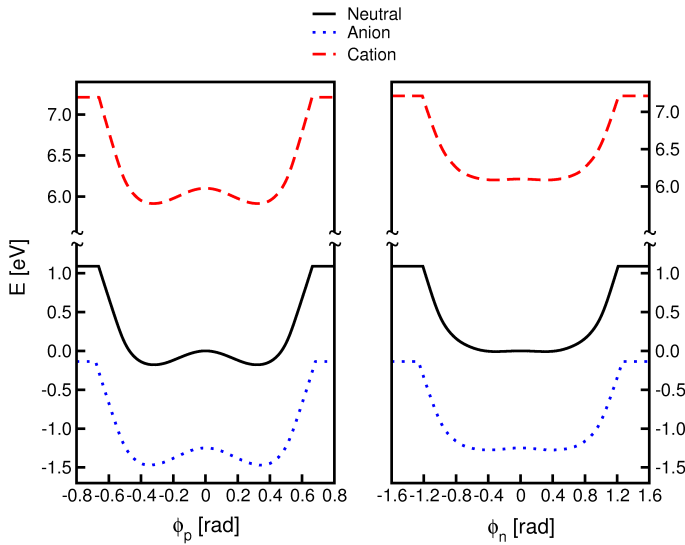


Figure 6.13: 1D cuts of neutral, cationic and anionic states of COD@Si(001) along ϕ_p and ϕ_n , respectively. These paths are plotted for PES with the following energy cutoffs of: 1.088 eV for neutral, -0.136 eV for cation and 7.211 eV for anion. Second order saddle point is set to 0 eV of the neutral PES.

1D cuts of different surfaces along ϕ_p at ($\phi_n = 0$) and ϕ_n at ($\phi_p = 0$) are shown in Fig. 6.13. The following changes, relative to the neutral PES, can be seen:

- (i) The potential of the anion is wider compared to the neutral species, with a minimum shift from 0.32 to ≈ 0.35 rad. The barrier rises to ≈ 220 meV.
- (ii) The cation potential is almost rigidly shifted and a minor increase of the barrier to ≈ 185 meV is found.

Both findings (i) and (ii) explain why the frequencies at the neutral and cation states are very similar, while those at the anion are somewhat different. Note that at a surface, the relative order of the different potential curves depends also on work functions and image charge contributions (see Section 3.4), which is neglected in Fig. 6.13. Note that in Fig. 6.13, potential energy cutoffs have been used (see caption).

Considering the path over ϕ_n , shifts of TSs and barriers can be discussed. The saddle points of the neutral species PES lie at ± 0.31 rad, which yields $\pm 24.4^\circ$ following the transformation rules of Eq.(6.2). Again, the anion PES is more wide, shifting the saddle points to ± 0.39 rad with a barrier of 25 meV, relative to 2nd order TS at $\phi_n = 0$ rad. The PES of the cation is similar to the neutral potential with saddle points at ± 0.32 rad ($\pm 25.2^\circ$) and an energy difference between the TSs and the 2nd order TS of 12 meV.

6.3 Switching Dynamics

6.3.1 Switching Hamiltonians for 2D and 1D Models

As previously said, the quantum dynamics of the system can be formulated using a switching Hamiltonian which has a simple form when written in the angular reaction coordinates, instead of the dihedral angles. One can see a graphical representation of the process in Fig. 6.14, illustrating the atom motion along a switching pathway.

In order to plot Fig. 6.14, Cartesian coordinates of atoms were extracted from the 1D path ($d_1 = d_2$) when $d_1 > 0^\circ$, see Fig. 6.9 (left). Details concerning the plot itself are described in the caption of Fig. 6.14. The atoms of the lower COD part (atoms C_1 , C_2 , C_5 and C_6 in Fig. 6.9, right) of the adsorbate are more or less stationary in comparison to the ones of the upper molecular part, which do the switching. At the same time, pairs of atoms C_3 - C_4 and C_7 - C_8 (marked in blue in Fig. 6.14) clearly show a movement which resembles rather the change of an angle than the dihedral angle: The angles ϕ_1 and ϕ_2 , given in Eq.(6.1) and pictured in Fig. 6.9 (right), define rotational motion between the pairs of atoms defined in blue.

From this analysis, it is reasonable to assume that the Hamiltonian \hat{H} has to describe the simultaneous rotational motion, of two $(CH_2)_2$ groups, preserving C_2 symmetry with respect to the molecular center. The rotational axes are dividing two pairs of CH_2 groups as given in Fig. 6.14, on the right. The moment of inertia for the rotation of each $(CH_2)_2$ units is¹:

$$I = 2m_{CH_2} \left(\frac{d_{CH_2-CH_2}}{2} \right)^2 = 109686.28 m_e a_0^2 \quad (6.3)$$

where $d_{CH_2-CH_2}$ stands for the C-C distance of 1.55 Å between the two CH_2 groups. The moments of inertia derived with respect to symmetrized reaction coordinates, ϕ_p and ϕ_n , have to be included in the switching Hamiltonian. The relations are derived in Appendix F. We find $I_p = 2I$ ($219372.57 m_e a_0^2$) and $I_n = 0.5I$ ($54843.14 m_e a_0^2$), finally getting the reduced-dimension (2D) model Hamiltonian for the switching

¹ $m_C = 12.011 amu$ and $m_H = 1.00794 amu$

process:

$$\hat{H} = -\frac{\hbar^2}{2I_p} \frac{\partial^2}{\partial \phi_p^2} - \frac{\hbar^2}{2I_n} \frac{\partial^2}{\partial \phi_n^2} + V(\phi_p, \phi_n). \quad (6.4)$$

By fixing ϕ_n to its equilibrium value ($\phi_n = 0$), a 1D-Hamiltonian can be defined as

$$\hat{H} = -\frac{\hbar^2}{2I_p} \frac{d^2}{d\phi_p^2} + V(\phi_p; \phi_n = 0). \quad (6.5)$$

Expressions (6.4) and (6.5) are derived in detail in Appendix F. The 1D and 2D Hamiltonians will be used for dynamics below.

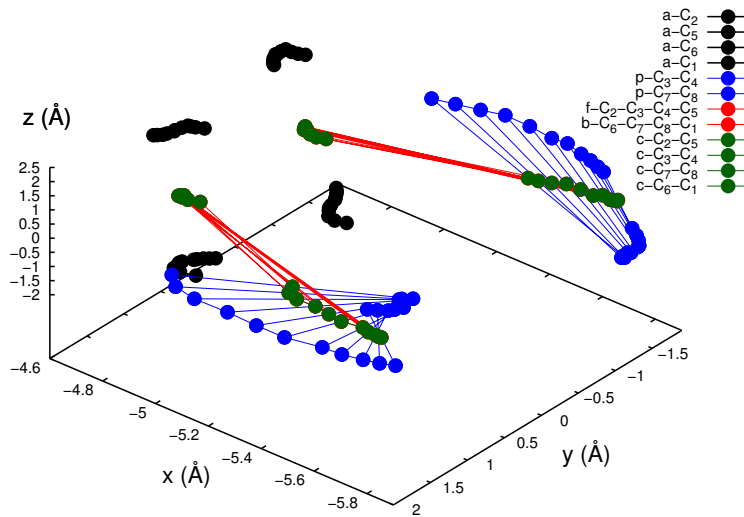


Figure 6.14: Pictorial representation of the switching process along a 1D path for $d_1 > 0^\circ$, in Cartesian coordinates of C-atoms of the COD molecule (numbering of atoms fits to Fig. 6.9, right). The coordinates were taken as the diagonal path scan (in this case $d_1 = d_2$) connecting the two minima and the 2nd order TS of the PES. In black, coordinates of the lower COD atoms (a-C₁, a-C₂, a-C₅, and a-C₆) directly connected to Si dimers are drawn, and in blue pairs of the coordinates of the upper part rotating atoms are connected. In red, the *front* (f-C₂-C₃-C₄-C₅) and the *back* (b-C₆-C₇-C₈-C₁) movement of the group of atoms is presented (plotted connecting coordinate averaged pairs given in green) overlaying with coordinate combinations of lower (c-C₂-C₅ and c-C₆-C₁) and upper (c-C₃-C₄ and c-C₇-C₈) atom combinations. The coordinate averaging is green color-coded and calculated as $(\frac{x_{C_2}+x_{C_5}}{2}, \frac{y_{C_2}+y_{C_5}}{2}, \frac{z_{C_2}+z_{C_5}}{2})$.

6.3.2 Vibrational Wave Functions

Switching dynamics is going to be described on symmetric double well potentials, as shown, for the 1D case, in Fig. 6.15, on the left. As mentioned before, minima of the well are energetically degenerate and separated by a barrier. For the 1D neutral surface, there are six doublets v below the barrier as shown in Fig. 6.15. All states are either of *gerade* (or *even*, (+)) or *ungerade* (or *odd*, (-)) parity. The vibrational energies of a given doublet, $E_{v\pm}$, are not degenerate. Here, E_{v+} and E_{v-} are energies of the eigenfunctions ψ_{v+} and ψ_{v-} , respectively, which are delocalized over both minima. The energy splitting, ΔE_v , depends on the height and width of the potential barrier and ΔE_v increases with increasing energy. One can calculate the so-called *tunneling time* as

$$\tau_v^{tun} = \hbar\pi / \Delta E_v \quad , \quad \Delta E_v = E_{v+} - E_{v-} . \quad (6.6)$$

The tunneling time in Eq.(6.6), τ_v^{tun} , represents the full period for tunneling of a localized wave packet, Eq.(6.8) below, from the left well to the right one and back. The lowest lying states have a τ_v^{tun} in a range of several μs .

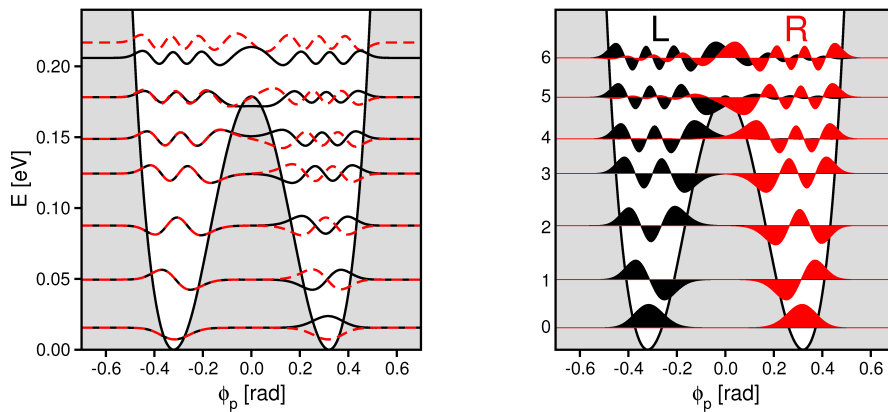


Figure 6.15: On the left hand side of the graph, scheme of six pairs of vibrational eigenstates below the barrier with an extra one above the barrier ($v = 0 \dots 6$). On the right hand side localized WFs in each of the potential wells.

From the two lowest eigenenergies, one can obtain the value for the fundamental *librational* frequency as:

$$\omega_{10} = (E_1^+ - E_0^+) / \hbar \quad (6.7)$$

which is, for instance, 35.4 meV, calculated for the 1D neutral potential. This corresponds to $\sim 286 \text{ cm}^{-1}$, which fits well to the (higher-frequency, harmonic) value of $\sim 283 \text{ cm}^{-1}$ given in Table 6.3 for the 2D case.

The eigenpairs were obtained by diagonalizing the switching Hamiltonian for the 1D case (2D case), given by Eq.(6.5) (Eq. (6.4)) using the *Fourier Grid Hamiltonian* (FGH) [135] method in a dense grid representation with $V(\phi_p, \phi_n = 0)$ ($V(\phi_p, \phi_n)$). Eigenvalues calculated in this way are used as the starting basis for quantum dynamical treatment, *i.e.*, solution of the time-dependent nuclear Schrödinger equation. For the 1D case we used a 256 point grid for $\phi_p \in [-0.8, 0.8]$ (0.0063 rad is the grid spacing in ϕ_p) for neutral, cationic and anionic potentials, with $0.04 E_h$ (1.088 eV), $-0.005 E_h$ (-0.136 eV) and $0.265 E_h$ (7.211 eV) as energy cutoffs, respectively (see Fig. 6.13). The cutoffs correspond to ≈ 6 times the height of the switching barrier. For the 2D model, we used 200 points in ϕ_p (0.008 rad for the grid spacing) \times 200 points in ϕ_n (0.016 rad for the grid spacing). We used the same energy cutoffs as in the 1D case.

As initial states and also for analysis, we will use localized WFs, rather than delocalized wave functions ψ_{v+} and ψ_{v-} . We use $|\psi_{vL}\rangle$ characterizing the left-localized well and similarly, $|\psi_{vR}\rangle$ for right-localized WFs. These are constructed by positive and negative superposition of pairs of vibrational eigenstates $|\psi_{v\pm}\rangle$ of the system [136]:

$$|\psi_{vL}\rangle = \frac{1}{\sqrt{2}} (|\psi_{v+}\rangle + |\psi_{v-}\rangle) , \quad |\psi_{vR}\rangle = \frac{1}{\sqrt{2}} (|\psi_{v+}\rangle - |\psi_{v-}\rangle) \quad (6.8)$$

6.3.3 Wave Packet Propagation: 1D Case

In this section, we will study the isomerization dynamics in COD@Si(001) using wave packet methods. The initial attachment of a hole or an electron in an STM-experiment at positive and negative sample bias, will be modeled by an initial, sudden excitation from the neutral ground state to ionized states. The finite lifetime, τ_{el} will be described by the Gadzuk jumping wave packet method, Section 2.2.2. Both 1D and 2D problems will be studied. Note that in the jumping wave packet approach, the relative energetic position of the different potential is unimportant.

In the 1D case, we will investigate the wave packet propagation for both types of resonances, negative and positive, by using the 1D double well potentials as presented in Fig. 6.13 and described in Section 6.2.6. We are using 2-state models in the eigenstate representation. That is, we propagate either in the neutral or an ionic (anion or cation) state, and the actual wave packet is expressed as in the eigenstate basis of the corresponding state, *i.e.*

$$|\psi\rangle = \sum_n |\psi_n^i\rangle \langle \psi_n^i | \psi \rangle \quad (6.9)$$

where ψ_n^i is the n -th vibrational eigenfunction of state i . For propagation, WPs were formed out of the 256 lowest vibrational states of the corresponding state. We also need to stress that neither finite temperature nor vibrational relaxation was taken into account here.

Starting the wave packet propagation from the left well, *i.e.*, $\psi(0) = \psi_{0L}$ of the neutral state, the population in the right well, or the switching probability, is calculated as

$$P_R(t) = \int_0^\pi d\phi_p \psi^*(\phi_p; t) \psi(\phi_p; t) \quad (6.10)$$

in the 1D case. At the same time, population in the starting (left) well is:

$$P_L(t) = 1 - P_R(t). \quad (6.11)$$

In Eq.(6.10), the population is defined for one quantum trajectory, for a certain residence time τ_R . In practice, one calculates a number of trajectories corresponding to different residence times τ_R in the ionic state according to the Gadzuk scheme, which need to be averaged for a certain electronic lifetime τ_{el} , using expression (2.69), *i.e.*

$$\langle \hat{P}_R \rangle = \frac{\int_0^\infty e^{-\tau_R/\tau_{el}} P_R(\tau_R) d\tau_R}{\int_0^\infty e^{-\tau_R/\tau_{el}} d\tau_R}. \quad (6.12)$$

Here, we will interpret $\langle P_R \rangle$ as the switching probability per excitation event.

Let us consider the switching via the anion resonance first, *i.e.* we have a transition from the neutral state (g) to the anion state (a), followed by electronic relaxation. In

Fig. 6.16 we show the integrand $P_R(t_p; \tau_R)e^{-\tau_R/\tau_{el}}$ for different times, t_p , as a function of the residence time, τ_R , in the anion state. For the calculation, a τ_R -grid with $\Delta\tau_R = 1$ fs was chosen, and “long” excited state lifetime of $\tau_{el} = 100$ fs. It is seen that in this case residence times up to ~ 500 fs are needed in order to make the integrand vanish. For shorter lifetimes τ_{el} , shorter maximal residence times τ_R can be used.

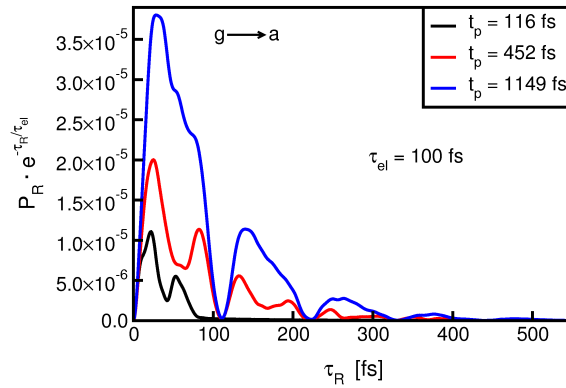


Figure 6.16: Dependence of $P_R \cdot e(-\tau_R/\tau_{el})$ on τ_R for the electronic lifetime of $\tau_{el} = 100$ fs.

In Fig. 6.17, left, we show the integrated switching probability $\langle P_R \rangle$ as a function of propagation time t_p , for different excited state lifetimes τ_{el} . We note that $\langle P_R \rangle$ shows oscillating behavior, reflecting the left \leftrightarrow right motion of the wave packet after return from the anion state, to the ground state. In reality, vibrational relaxation would be effective typically after ~ 1 ps [137, 138], which is neglected here. Vibrational relaxation would lead to a levelling off of the $\langle P_R \rangle$ curves after

around that time. In order to get a meaningful measure for the switching probability, we choose $t_p = 1$ ps in the following, and, for comparison, also a longer propagation time $t_p = 5$ ps to evaluate “the” switching probability.

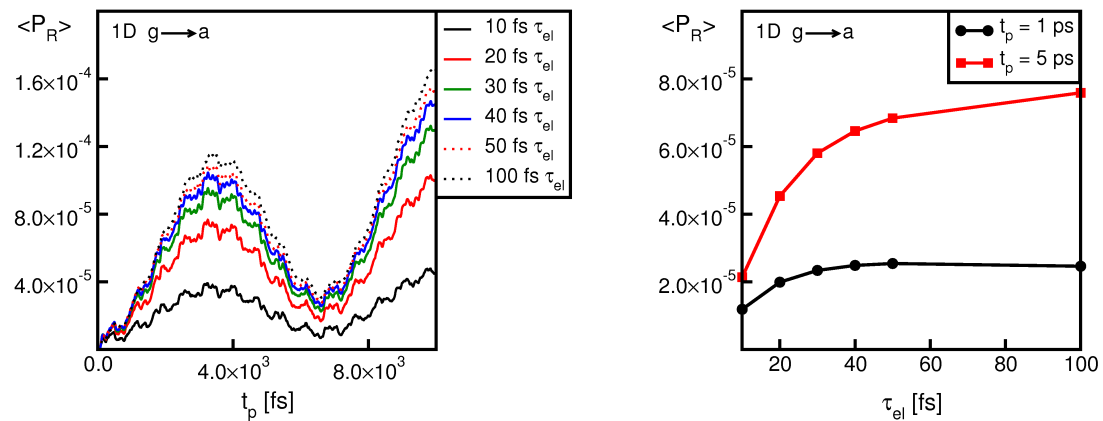


Figure 6.17: Calculated averaged switching probability after excitation from the ground state to the anion, $g \rightarrow a$, for different τ_{el} , are given on the left. Extracting the values of $\langle P_R \rangle$ at 1 ps and 5 ps (t_p), we are getting the graph $\langle P_R \rangle$ vs. τ_{el} in the right.

In Fig. 6.17, right, we show the switching probability $\langle P_R \rangle$ as a function of τ_{el} , at these two times. It is seen that for "reasonable" excited state lifetimes of τ_{el} in the order of a few tens of fs for $t_p = 1$ ps (as a measure for the vibrational relaxation time), the switching probability per excitation event is in the order of 2×10^{-5} and not dramatically τ_{el} -dependent. For $t_p = 5$ ps, the switching probability is somewhat - but again not dramatically - higher. The experimental switching rate per electron according to Ref. [20] is $\approx 10^{-9}$. Assuming that the excitation probability per electron is in the order of $10^{-3} - 10^{-4}$, which is reasonable [139], the calculated switching probability is in the right order of magnitude.

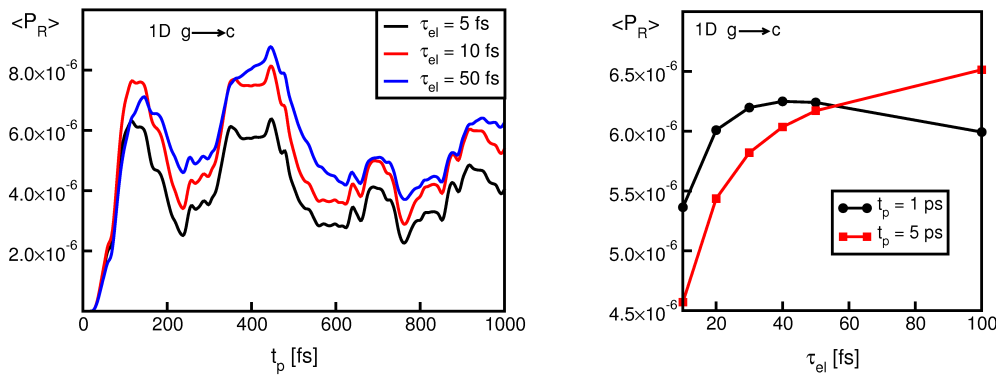


Figure 6.18: On the left, averaged switching probability after excitation from the ground state to the cation, $g \rightarrow c$, for different τ_{el} . On the right, $\langle P_R \rangle$ vs. τ_{el} for the comparison of $t_p = 1$ ps and $t_p = 5$ ps, respectively.

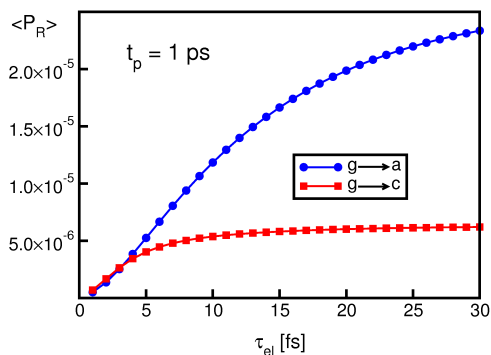


Figure 6.19: Comparison of switching probabilities for the $g \rightarrow a$ and $g \rightarrow c$ cases. Values are averaged for τ_{el} in the range of 1-30 fs.

Similarly, we show in Fig. 6.18, left, the averaged switching probability $\langle P_R \rangle$ for the case of a cation resonance mediated mechanism, with initial excitation of ψ_{0L} from the neutral ground state (g) to the cation state (c), as a function of propagation time t_p . Also here an oscillatory behavior is found. When plotting the switching probability for the cation case at $t_p = 1$ ps and $t_p = 5$ ps as a function of the electronic lifetime τ_{el} (Fig. 6.18, right), it is also found that $\langle P_R \rangle$ does not drastically change with

τ_{el} . In the cation case, no big differences are observed between $t_p = 1$ ps and $t_p = 5$ ps.

For the cationic mechanism, the switching probability is generally a bit smaller than for the anion case (Fig. 6.19), because the excited wave packet is less displaced in the cation state than in the anion state, due to the very similar topologies of cation and neutral PES.

6.3.4 Wave Packet Propagation: 2D Case

Switching probabilities calculated by propagating WP on our 2D PESs will be discussed here. We used symmetrized potentials for neutral, cationic and anionic states. The wave packet for the propagation was composed out of the 2000 lowest states for each potential. Moreover, 400 trajectories were computed, which was sufficient to average the data using the Gadzuk formula (2.2.2).

In Fig. 6.20, we are comparing, for $g \rightarrow a$ case, spatial densities for a single trajectory, when $\tau_R = 52$ fs. At first (at $t_p = 0$), the WP is localized in the left well, which, after excitation and spending 52 fs in the excited state, is being dumped back to the ground state and left to oscillate until a propagation time $t_p = 1$ ps. Note that by the time a small fraction of the WP is located in the right well.

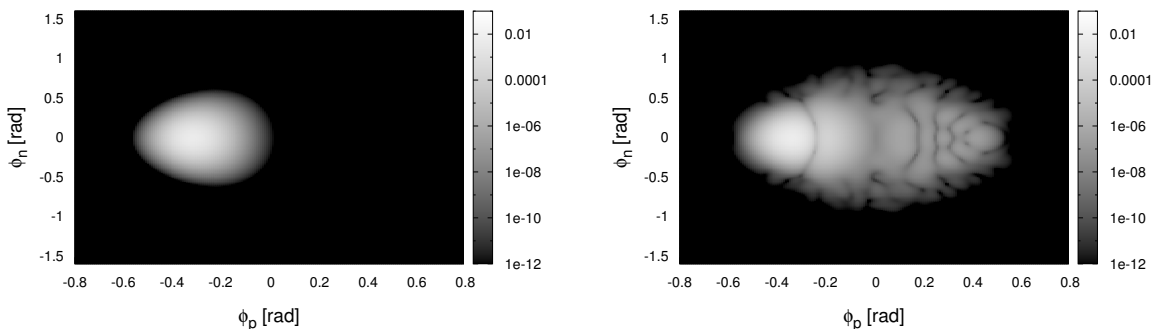


Figure 6.20: Representation of the spatial density $|\psi(\phi_n, \phi_p)|^2$ for the $g \rightarrow a$ 2D propagation for a single trajectory of $\tau_R = 52$ fs. On the left hand side, localized populations in the left well can be seen ($t_p = 0$ ps). On the right hand side, we see the snapshot of the WP at $t_p = 1$ ps.

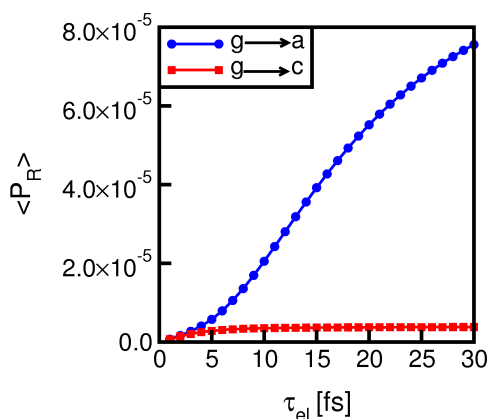


Figure 6.21: Calculated switching probabilities for the 2D case, for both resonances, $g \rightarrow a$ and $g \rightarrow c$ averaged over 400 trajectories for several τ_{el} . As before, values for $\langle P_R \rangle$ are taken at $t_p = 1$ ps.

reaction involving the cation resonance appears to be slower in 2D. Switching over the anion resonance seems to be more efficient particularly at longer times. The latter mechanism allows the WP to spread in the region of the TS as well (see Fig. 6.20), which is lower in energy than the maximum barrier. However, the values for $\langle P_R \rangle$ are on the same order of magnitude. Thus, the 1D approximation turns out to be already qualitatively correct.

6.4 Summary

Functionalization of semiconductor surfaces with switching molecules can be extensively used for molecule-scaled devices [117]. Quantum chemical investigation is, for these systems, “easily feasible” compared to systems with bulky molecules being physisorbed at metal surfaces. We presented a detailed, quantum chemical and quantum dynamical study for the COD molecule at Si(001). Within the cluster model used here, we showed that the *upright* forms of the molecule are energetically less stable than the *bridge* structure. The latter one exists in two degenerated forms at the surface, separated by a shallow energy barrier. The switching behavior of such systems was studied experimentally using an STM at low temperatures [20].

In Fig. 6.21 we compare averaged $\langle P_R \rangle$ values for both cation and anion resonances, as a function of the excited state lifetime τ_{el} . The values are extracted for the characteristic propagation time $t_p = 1$ ps. One sees that the anion resonance is more efficient over the whole range, 1-30 fs, for τ_{el} . The cation resonance is more or less constant for all chosen excited state lifetimes, being in the order of $\approx 10^{-6}$.

Finally, one should point out the differences occurring between our 2D model and its 1D approximation. The reac-

The mechanism of this reaction is unknown, but ion-resonance mediated mechanisms have been suggested. Using a jumping wave packet approach, we have shown that both anionic and cationic resonances may be operative in the process, since both of them yield switching probabilities roughly comparable to experiment. Of course, also other mechanisms may contribute to the switching, *e.g.*, the dipole-coupling mechanism as suggested in Ref. [25]. Further theoretical and experimental investigations are needed to unravel quantitatively the different contributions to STM-induced of COD@Si(001).

Since in COD@Si(001) both minima of the *bridge* structure are energetically and in many other respects equivalent, the "switching" is not accompanied by any change of properties. In order to use this molecule for practical purpose, substitution of COD by functional groups could be a way for modifying the electronic structure of the molecule, trying to make one of the minima energetically more stable. In this case, also a change of properties is expected upon switching.

Chapter 7

Conclusion and Outlook

In conclusion, we have investigated various switching molecules, emphasizing three different aspects: (i) We studied the electronic structure and (ii) the thermal isomerization of azobenzene and its derivatives in the gas phase and in solution, and (iii) we modeled resonant, STM-induced switching of 1,5-cyclooctadiene on a Si(001) cluster, at low temperatures. The main purpose of this work was to combine knowledge obtained from experiments and from theory to explain switching mechanisms at a surface and in different environments.

Photochemical or STM-induced isomerization processes, in particular on metals, *e.g.*, a *trans*→*cis* switch, have been suggested to be substrate mediated, assuming that the reaction occurs via positive or negative short-lived ion resonances. It has been shown that such premise is justified mostly due to the energetically low reaction barriers of ionic species, at least over inversional and rotational, α and ω , degrees of freedom. For the phenyl ring rotation in DMC along a dihedral angle β , we demonstrated that in addition to the formation of an anion resonance an influence of static electric fields has to be included in order to rationalize switching experiments for this system.

Thermal *cis*→*trans* isomerization was studied, as a ground state process over a linear transition state, using Eyring's transition state theory. We showed that this approximation gives reliable results for activation energies and rates, compared to experimental findings. Isomerization barriers were brought in a connection to

molecular substitution where we showed that electron acceptors lower the activation barriers, particularly efficient when placed at the same ring, in *ortho* and *para* positions. Electron donors were found to be not that efficient in lowering activation energies. Substitution affects also absorption spectra by shifting characteristic absorption band maxima of both *cis*- and *trans*-azobenzenes. Mimicking the solvent environment by using a polarizable continuum model, thermal isomerization has been studied for the DO3 molecule. We found that the presence of a polar solvent changes the isomerization mechanism, going over the linear transition state, in non-polar, to a rotational transition state, in more polar solvents. The presence of a polar solvent is found to be unimportant for UV/Vis absorption spectra and *cis* and *trans* geometries.

At last, we studied possible reaction mechanisms for the STM isomerization of COD@Si(001). Quantum chemical analysis of the systems by a cluster model was followed by a quantum dynamical study using wave packet methods. We have shown, that at low temperatures, inelastic electron (hole) tunneling leading to short-lived anionic or cationic resonances, may play a decisive role.

Quo vadis? Although this work contributed to the understanding of isomerization paths of molecular switches, there are still many unresolved questions. Generalizing the mechanisms on metal surfaces is not straightforward mostly because the adsorbed molecules experience conformational changes, induced by external stimuli, only on specific substrates. The role of a metal surface is obviously very important and its explicit theoretical treatment would be a great challenge. This issue becomes even more complicated due to the fact that photochromic molecules can be physisorbed rather than chemisorbed at surfaces, at least for the cases which were addressed in this work. Functionalization with species that are covalently attached to the substrate might be a solution, but, keeping in mind that excited state lifetimes at surfaces are very short, switching could be easily quenched. In that manner charge transfer processes between the chromophore and a metal or a semiconductor would be interesting to investigate. Since molecular electronics acquire assemblies of switching species, another important issue would be to study an influence of neighboring molecules on isomerization kinetics.

Bibliography

- [1] Balzani, V.; Credi, A.; Venturi, M. *Molecular devices and machines. Concepts and perspectives for the nanoworld. 2nd Ed.*; Wiley-VCH, 2008.
- [2] Feringa, B. *Molecular Switches*; Wiley-VCH: Weinheim, second ed., 2001.
- [3] Hirshberg, Y. *J. Am. Chem. Soc.* **1956**, *78*, 2304–2312.
- [4] Rando, R. R. *Angew. Chem. Int. Ed.* **1990**, *29*, 461–480.
- [5] Hahn, S.; Stock, G. *J. Phys. Chem. B* **2000**, *104*, 1146–1149.
- [6] Hahn, S.; Stock, G. *Chem. Phys.* **2000**, *259*, 297–312.
- [7] Rau, H. *Photochromism: Molecules and Systems*; Elsevier: Amsterdam, 1990.
- [8] Hampp, N. *Chem. Rev.* **2000**, *100*, 1755–1776.
- [9] Ikeda, T.; Tsutsumi, O. *Science* **1995**, *268*, 1873–1875.
- [10] Shorter, J. *The chemistry of the hydrazo, azo and azoxy groups*; Interscience publication, 1997.
- [11] Alemani, M.; Peters, M. V.; Hecht, S.; Rieder, K.-H.; Moresco, F.; Grill, L. *J. Am. Chem. Soc.* **2006**, *128*, 14446–14447.
- [12] Dri, C.; Peters, M. V.; Schwarz, J.; Hecht, S.; Grill, L. *Nature Nano.* **2008**, *3*, 649–653.
- [13] Comstock, M. J.; Levy, N.; Kirakosian, A.; Cho, J.; Lauterwasser, F.; Harvey, J. H.; Strubbe, D. A.; Fréchet, J. M. J.; Trauner, D.; Louie, S. G.; Crommie, M. F. *Phys. Rev. Lett.* **2007**, *99*, 038301–4.

- [14] Wolf, M.; Tegeder, P. *Surf. Sci.* **2009**, *603*, 1506–1517.
- [15] Choi, B.-Y.; Kahng, S.-J.; Kim, S.; Kim, H.; Kim, H. W.; Song, Y. J.; Ihm, J.; Kuk, Y. *Phys. Rev. Lett.* **2006**, *96*, 156106–4.
- [16] Tegeder, P.; Hagen, S.; Leyssner, F.; Peters, M. V.; Hecht, S.; Klamroth, T.; Saalfrank, P.; Wolf, M. *Appl. Phys. A* **2007**, *88*, 465–472.
- [17] Hagen, S.; Leyssner, F.; Nandi, D.; Wolf, M.; Tegeder, P. *Chem. Phys. Lett.* **2007**, *444*, 85–90.
- [18] Hagen, S.; Kate, P.; Peters, M. V.; Hecht, S.; Wolf, M.; Tegeder, P. *Appl. Phys. A* **2008**, *93*, 253–260.
- [19] Henningsen, N.; Franke, K. J.; Fernández-Torrente, I.; Schulze, G.; Priewisch, B.; Rück-Braun, K.; Dokić, J.; Klamroth, T.; Saalfrank, P.; Pascual, J. I. *J. Phys. Chem. C* **2007**, *111*, 14843–14848.
- [20] Nacci, C.; Lagoute, J.; Liu, X.; Fölsch, S. *Phys. Rev. B* **2008**, *77*, 121405(R)–4.
- [21] Grill, L. *J. Phys.: Condens. Matter* **2008**, *20*, 053001–19.
- [22] Alemani, M.; Selvanathan, S.; Ample, F.; Peters, M. V.; Rieder, K.-H.; Moresco, F.; Joachim, C.; Hecht, S.; Grill, L. *J. Phys. Chem. C* **2008**, *112*, 10509–10514.
- [23] Tegeder, P.; Hagen, S.; Leyssner, F.; Peters, M.; Hecht, S.; Klamroth, T.; Saalfrank, P.; Wolf, M. *Appl. Phys. A* **2007**, *88*, 465–472.
- [24] Dokić, J.; Gothe, M.; Wirth, J.; Peters, M. V.; Schwarz, J.; Hecht, S.; Saalfrank, P. *J. Phys. Chem. A* **2009**, *113*, 6763–6773.
- [25] Nacci, C.; Fölsch, S.; Zenichowski, K.; Dokić, J.; Klamroth, T.; Saalfrank, P. *Nano Lett.* **2009**, *9*, 2996–3000.
- [26] Frisch, M. J.; Trucks, G. W.; Schlegel, H. B.; Scuseria, G. E.; Robb, M. A.; Cheeseman, J. R.; Montgomery, Jr., J. A.; Vreven, T.; Kudin, K. N.; Burant, J. C.; Millam, J. M.; Iyengar, S. S.; Tomasi, J.; Barone, V.; Mennucci, B.; Cossi, M.; Scalmani, G.; Rega, N.; Petersson, G. A.; Nakatsuji, H.; Hada, M.; Ehara, M.; Toyota, K.; Fukuda, R.; Hasegawa, J.; Ishida, M.; Nakajima, T.; Honda, Y.; Kitao, O.; Nakai, H.; Klene, M.; Li, X.; Knox, J. E.; Hratchian,

- H. P.; Cross, J. B.; Bakken, V.; Adamo, C.; Jaramillo, J.; Gomperts, R.; Stratmann, R. E.; Yazyev, O.; Austin, A. J.; Cammi, R.; Pomelli, C.; Ochterski, J. W.; Ayala, P. Y.; Morokuma, K.; Voth, G. A.; Salvador, P.; Dannenberg, J. J.; Zakrzewski, V. G.; Dapprich, S.; Daniels, A. D.; Strain, M. C.; Farkas, O.; Malick, D. K.; Rabuck, A. D.; Raghavachari, K.; Foresman, J. B.; Ortiz, J. V.; Cui, Q.; Baboul, A. G.; Clifford, S.; Cioslowski, J.; Stefanov, B. B.; Liu, G.; Liashenko, A.; Piskorz, P.; Komaromi, I.; Martin, R. L.; Fox, D. J.; Keith, T.; Al-Laham, M. A.; Peng, C. Y.; Nanayakkara, A.; Challacombe, M.; Gill, P. M. W.; Johnson, B.; Chen, W.; Wong, M. W.; Gonzalez, C.; .; Pople, J. A. Gaussian 03, Revision C.02; Wallingford CT, Gaussian, Inc., **2004**.
- [27] Born, M.; Oppenheimer, J. R. *Ann. Phys.* **1927**, *389*, 457–484.
- [28] Szabo, A.; Ostlund, N. *Modern Quantum Chemistry*; Dover Publications, Inc., 1996.
- [29] Roothaan, C. C. J. *Rev. Mod. Phys.* **1951**, *23*, 69–89.
- [30] Hall, G. G. *Proc. Roy. Soc. (London)* **1951**, *A205*, 541.
- [31] Krishnan, R.; Binkley, J. S.; Seeger, R.; Pople, J. A. *J. Chem. Phys.* **1980**, *72*, 650–654.
- [32] Frisch, M. J.; Pople, J. A.; Binkley, J. S. *J. Chem. Phys.* **1984**, *80*, 3265–3269.
- [33] Francel, M. M.; Pietro, W. J.; Hehre, W. J.; Binkley, J. S.; Gordon, M. S.; DeFrees, D. J.; Pople, J. A. *J. Chem. Phys.* **1982**, *77*, 3654–3665.
- [34] Jensen, F. *Introduction to computational chemistry*; John Wiley & Sons Ltd, 2007.
- [35] Cramer, C. *Essentials of computational chemistry*; John Wiley & Sons Ltd, 2002.
- [36] Hohenberg, P.; Kohn, W. *Phys. Rev.* **1964**, *136*, B864–B871.
- [37] Kohn, W.; Sham, L. J. *Phys. Rev.* **1965**, *140*, A1133–A1138.
- [38] Parr, R.; Yang, W. *Density-functional theory of atoms and molecules*; Oxford University Press, 1989.

- [39] Becke, A. D. *Phys. Rev. A* **1988**, *38*, 3098–3100.
- [40] Stephens, P. J.; Devlin, F. J.; Chabalowski, C. F.; Frisch, M. J. *J. Phys. Chem.* **1994**, *98*, 11623–11627.
- [41] Handy, N.; Cohen, A. *Mol. Phys.* **2001**, *99*, 403–412.
- [42] Casida, M. E.; Jamorski, C.; Casida, K. C.; Salahub, D. R. *J. Chem. Phys.* **1998**, *108*, 4439–4449.
- [43] Stratmann, R. E.; Scuseria, G. E.; Frisch, J. M. *J. Chem. Phys.* **1998**, *109*, 8218–8224.
- [44] Dreuw, A.; Head-Gordon, M. *J. Am. Chem. Soc.* **2004**, *126*, 4007–4016.
- [45] Tomasi, J.; Mennucci, B.; Cammi, R. *Chem. Rev.* **2005**, *105*, 2999–3094.
- [46] Onsager, L. *J. Am. Chem. Soc.* **1936**, *58*, 1486–1493.
- [47] Miertuš, S.; Scrocco, E.; Tomasi, J. *Chem. Phys.* **1981**, *55*, 117.
- [48] Tomasi, J.; Persico, M. *Chem. Rev.* **1994**, *94*, 2027–2094.
- [49] Cancès, E.; Mennucci, B.; Tomasi, J. *J. Chem. Phys.* **1997**, *107*, 3032–3041.
- [50] Mennucci, B.; Cancès, E.; Tomasi, J. *J. Chem. Phys. B* **1997**, *101*, 10506–10517.
- [51] Tomasi, J.; Mennucci, B.; Cancès, E. *J. Mol. Struct. (Theochem)* **1999**, *464*, 211–226.
- [52] Eyring, H. *Chem. Rev.* **1935**, *17*, 65–77.
- [53] Evans, M. G.; Polanyi, M. *Trans. Faraday Soc.* **1935**, *31*, 875–894.
- [54] Steinfeld, J.; Francisco, J.; Hase, W. *Chemical kinetics and dynamics*, 2nd Ed.; Prentice Hall, Inc., 1999.
- [55] Henkelman, G.; Jóhannesson, G.; Jónsson, H. *Methods for Finding Saddle Points and Minimum Energy Paths*, Progress on Theoretical Chemistry and Physics; Kluwer Academic Publishers, 2000.
- [56] Schlegel, H. B. *J. Comp. Chem.* **2003**, *24*, 1514–1517.

- [57] Fukui, K. *Acc. Chem. Res.* **1981**, *14*, 363–368.
- [58] Flannery, B. P.; Press, W. H.; Teukolsky, S. A.; Vetterling, W. T. *Numerical Recipes in C++. The Art of Scientific Computing*; Cambridge University Press, second ed., 2002.
- [59] Peng, C.; Schlegel, H. B. *Israel J. Chem.* **1993**, *33*, 449–454.
- [60] Peng, C.; Ayala, P.; Schlegel, H.; Frisch, M. *J. Comp. Chem.* **1996**, *17*, 49.
- [61] Ayala, P. Y.; Schlegel, H. B. *J. Chem. Phys.* **1997**, *107*, 375–384.
- [62] Gadzuk, J. W.; Richter, L. J.; Buntin, S. A.; King, D. S.; Cavanagh, R. R. *Surf. Sci.* **1990**, *235*, 317–333.
- [63] Gadzuk, J. W. *Surf. Sci.* **1995**, *342*, 345–358.
- [64] Saalfrank, P.; Boendgen, G.; Finger, K.; Pesce, L. *Chem. Phys.* **2000**, *251*, 51–69.
- [65] Saalfrank, P.; Boendgen, G.; Corriol, C.; Nakjima, T. *Faraday Discuss.* **2000**, *117*, 65–83.
- [66] Vazhappilly, T.; Beyvers, S.; Klamroth, T.; Luppi, M.; Saalfrank, P. *Chem. Phys.* **2007**, *338*, 299–311.
- [67] Saalfrank, P. *Chem. Phys.* **1996**, *211*, 265–276.
- [68] Briquet, L.; Vercauteren, D. P.; Perpète, E. A.; Jacquemin, D. *Chem. Phys. Lett.* **2006**, *417*, 190–195.
- [69] Füchsel, G.; Klamroth, T.; Dokić, J.; Saalfrank, P. *J. Phys. Chem. B* **2006**, *110*, 16337–16345.
- [70] Schultz, T.; Quenneville, J.; Levine, B.; Toniolo, A.; Martinez, T. J.; Lochbrunner, S.; Schmitt, M.; Shaffer, J. P.; Zgierski, M. Z.; Stolow, A. *J. Am. Chem. Soc.* **2003**, *125*, 8098–8099.
- [71] Toniolo, A.; Ciminelli, C.; Persico, M.; Martinez, T. J. *J. Chem. Phys.* **2005**, *123*, 234308–10.

- [72] Briquet, L.; Vercauteren, D. P.; André, J.-M.; Perpète, E. A.; Jacquemin, D. *Chem. Phys. Lett.* **2007**, *435*, 257–262.
- [73] Diau, E. W.-G. *J. Phys. Chem. A* **2004**, *108*, 950–956.
- [74] Cattaneo, P.; Persico, M. *Phys. Chem. Chem. Phys.* **1999**, *1*, 4739–4743.
- [75] Satzger, H.; Root, C.; Braun, M. *J. Phys. Chem. A* **2004**, *108*, 6265–6271.
- [76] Gagliardi, L.; Orlandi, G.; Bernardi, F.; Cembran, A.; Garavelli, M. *Theor. Chem. Acc.* **2004**, *111*, 363–372.
- [77] Fliegl, H.; Köhn, A.; Hättig, C.; Ahlrichs, R. *J. Am. Chem. Soc.* **2003**, *125*, 9821–9827.
- [78] Bouwstra, J. A.; Schouten, A.; Kroon, J. *Acta Crystallogr. C* **1983**, *40*, 428–431.
- [79] Mostad, A.; Rømming, C. *Acta Chem. Scand.* **1971**, *25*, 3561–3568.
- [80] Andersson, J.-A.; Petterson, R.; Tegner, L. *J. Photochem.* **1982**, *20*, 17–32.
- [81] Jaffé, H. H.; Yeh, S.; Gardner, R. W. *J. Mol. Spec.* **1958**, *2*, 120–136.
- [82] Ishikawa, T.; Noro, T.; Shoda, T. *J. Chem. Phys.* **2001**, *115*, 7503–7512.
- [83] Tiago, M. L.; Ismail-Beigi, S.; Louie, S. G. *J. Chem. Phys.* **2005**, *122*, 094311–7.
- [84] Talaty, E. R.; Fargo, J. C. *Chem. Comm.* **1967**, *2*, 65–66.
- [85] Óvári, L.; Schwarz, J.; Peters, M.; Hecht, S.; Wolf, M.; Tegeder, P. *Int. J. Mass Spectrom.* **2008**, *277*, 223–228.
- [86] Hagen, S.; Kate, P.; Leyssner, F.; Nandi, D.; Wolf, M.; Tegeder, P. *J. Chem. Phys.* **2008**, *129*, 164102–8.
- [87] Gritsenko, O. V.; Baerends, E. J. *J. Chem. Phys.* **2002**, *117*, 9154–9159.
- [88] Henningsen, N.; Franke, K. J.; Schulze, G.; Fernández-Torrente, I.; Priewisch, B.; Rück-Braun, K.; Pascual, J. I. *Chem. Phys. Chem.* **2008**, *9*, 71–73.

- [89] Alemani, M. *Low temperature STM investigation of molecular manipulation, decoupling, and switching* PhD thesis, Freie Universität Berlin, **2006**.
- [90] Tsuji, T.; Takashima, H.; Takeuchi, H.; Egawa, T.; Konaka, S. *J. Mol. Struct.* **2000**, *554*, 203–210.
- [91] Tsuji, T.; Takashima, H.; Takeuchi, H.; Egawa, T.; Konaka, S. *J. Chem. Phys. A* **2001**, *105*, 9347–9353.
- [92] Saalfrank, P. *J. Chem. Phys.* **2000**, *113*, 3780–3791.
- [93] Hofmann, H.-J.; Cimiraglia, R.; Tomasi, J. *J. Mol. Struct. (Theochem)* **1987**, *152*, 19–33.
- [94] Asano, T.; Furuta, H.; Hofmann, H.-J.; Cimiraglia, R.; Tsuno, Y.; Fujio, M. *J. Org. Chem.* **1993**, *58*, 4418–4423.
- [95] Cimiraglia, R.; Asano, T.; Hofmann, H.-J. *Gazz. Chim. Ital.* **1996**, *126*, 679–684.
- [96] Wildes, P. D.; Pacifici, J. G.; Irick Jr., G.; Whitten, D. G. *J. Am. Chem. Soc.* **1971**, *93*, 2004–2008.
- [97] Sueyoshi, T.; Nishimura, N.; Yamamoto, S.; Hasegawa, S. *Chem. Lett.* **1974**, *3*, 1131–1134.
- [98] Asano, T.; Okada, T. *J. Org. Chem.* **1984**, *49*, 4387–4391.
- [99] Kucharski, S.; Janik, R.; Motschmann, H.; Radüge, C. *New J. Chem.* **1999**, *23*, 765–771.
- [100] Nishimura, N.; Sueyoshi, T.; Yamanaka, H.; Imai, E.; Yamamoto, S.; Hasegawa, S. *Bull. Chem. Soc. Jpn.* **1976**, *49*, 1381–1387.
- [101] Becke, A. D. *J. Chem. Phys.* **1993**, *98*, 5648–5652.
- [102] Ditchfield, R.; Hehre, W. J.; Pople, J. A. *J. Chem. Phys.* **1971**, *54*, 724–728.
- [103] Hehre, W. J.; Ditchfield, R.; Pople, J. A. *J. Chem. Phys.* **1972**, *56*, 2257–2261.
- [104] Hariharan, P. C.; Pople, J. A. *Theor. Chem. Acc.* **1973**, *28*, 213–222.

- [105] Gaenko, A. V.; Devarajan, A.; Gagliardi, L.; Lindh, R.; Orlandi, G. *Theor. Chem. Acc.* **2007**, *118*, 271–279.
- [106] Respondek, I.; Bressel, L.; Saalfrank, P.; Kämpf, H.; Grohmann, A. *Chem. Phys.* **2008**, *347*, 514–522.
- [107] Zarwell, S.; Rück-Braun, K. *Tetrahedron Lett.* **2008**, *49*, 4020–4025.
- [108] Mustroph, H.; Epperlein, J. *J. f. prakt. Chemie* **1980**, *322*, 49–54.
- [109] Hammett, L. P. *Chem. Rev.* **1935**, *17*, 125–136.
- [110] Nishimura, N.; Kosako, S.; Sueishi, Y. *Bull. Chem. Soc. Jpn.* **1984**, *57*, 1617–1625.
- [111] Laidler, K.; Landskroener, P. *Trans. Faraday Soc.* **1956**, *52*, 200–210.
- [112] Selvanathan, S.; Peters, M. V.; Schwarz, J.; Hecht, S.; Grill, L. *Appl. Phys. A* **2008**, *93*, 247–252.
- [113] Peters, M. V. *Photoschaltbare Photokatalysatoren* PhD thesis, Humboldt Universität Berlin, **2008**.
- [114] McLean, A. D.; Chandler, G. S. *J. Chem. Phys.* **1980**, *72*, 5639–5648.
- [115] Geibel, K.; Grellmann, K.; Staudinger, B.; Wendt, H. *Ber. Bunsenges. Phys. Chem.* **1972**, *76*, 1246.
- [116] Luo, Y.; Haag, R. *private communication*.
- [117] Martin, M.; Lastapis, M.; Riedel, D.; Dujardin, G.; Mamatkulov, M.; Stauffer, L.; Sonnet, P. *Phys. Rev. Lett.* **2006**, *97*, 216103–4.
- [118] Riedel, D.; Cranney, M.; Martin, M.; Guillory, R.; Dujardin, G.; Dubois, M.; Sonnet, P. *J. Am. Chem. Soc.* **2009**, *131*, 5414–5423.
- [119] Riedel, D.; Bocquet, M.-L.; Lesnard, H.; Lastapis, M.; Lorente, N.; Sonnet, P.; Dujardin, G. *J. Am. Chem. Soc.* **2009**, *131*, 7344–7352.
- [120] Wolkow, R. A. *Ann. Rev. Phys. Chem.* **1999**, *50*, 413–441.
- [121] Hamers, R. J.; Hovis, J. S.; Lee, S.; Liu, H.; Shan, J. *Phys. Chem. B* **1997**, *101*, 1489–1492.

- [122] Hovis, J. S.; Hamers, R. J. *J. Phys. Chem. B* **1997**, *101*, 9581–9585.
- [123] Cho, J.-H.; Oh, D.-H.; Kleinman, L. *Phys. Rev. B* **2001**, *64*, 241306–4.
- [124] Festa, G.; Cossi, M.; Barone, V.; Cantele, G.; Ninno, D.; Iadonisi, G. *J. Chem. Phys.* **2005**, *122*, 184714–8.
- [125] Wolkow, R. A. *Phys. Rev. Lett.* **1992**, *68*, 2636–2639.
- [126] Ono, M.; Kamoshida, A.; Matsuura, N.; Ishikawa, E.; Eguchi, T.; Hasegawa, Y. *Phys. Rev. B* **2003**, *67*, 201306(R)–4.
- [127] Perdigão, L.; Deresmes, D.; Grandidier, B.; Dubois, M.; Delerue, C.; Allan, G.; Stiévenard, D. *Phys. Rev. Lett.* **2004**, *92*, 216101–4.
- [128] Weinelt, M.; Kutschera, M.; Schmidt, R.; Orth, C.; Fauster, T.; Rohlfing, M. *Appl. Phys. A* **2005**, *80*, 995–1003.
- [129] Hagen, S. Adsorption molekularer schalter und elektronendynamik an si(100)- und si(100)-h-oberflächen Master's thesis, Freie Universität Berlin, **2005**.
- [130] Hata, K.; Shibata, Y.; Shigekawa, H. *Phys. Rev. B* **2001**, *64*, 235310–6.
- [131] Kittel, C. *Einführung in die Festkörperphysik*; Oldenburg Verlag München Wien, 14 ed., 2006.
- [132] Hamers, R. J.; Coulter, S. K.; Ellison, M. D.; Hovis, J. S.; Padowitz, D. F.; Schwartz, M. P.; Greenlief, C. M.; Russel Jr., J. N. *Acc. Chem. Res.* **2000**, *33*, 617–624.
- [133] Yavari, I.; Kabiri-Fard, H.; Moradi, S. *J. Iran. Chem. Soc.* **2004**, *1*, 71–78.
- [134] Rocha, W. R.; De Almeida, W. B. *J. Comp. Chem.* **1997**, *18*, 254–259.
- [135] Clay Marston, C.; Balint-Kurti, G. G. *J. Chem. Phys.* **1989**, *91*, 3571–3576.
- [136] Hund, F. *Z. Phys.* **1927**, *43*, 805–826.
- [137] Andrianov, I.; Saalfrank, P. *Chem. Phys. Lett.* **2001**, *350*, 191–197.
- [138] Andrianov, I.; Saalfrank, P. *J. Chem. Phys.* **2006**, *124*, 034710–10.
- [139] Stokbro, K.; Quaade, U. J.; Lin, R.; Thirstrup, C.; Grey, F. *Faraday Discuss.* **2000**, *117*, 231–240.

Appendices

Appendix A

DFT Functional Test

Various DFT methods will be tested for the case of both *cis*- and *trans*-TBA molecules. For the purpose of better understanding and interpretation of experimental results, relative positions of the orbital levels have been computed for previously optimized molecules, with a variety of basis sets. We also

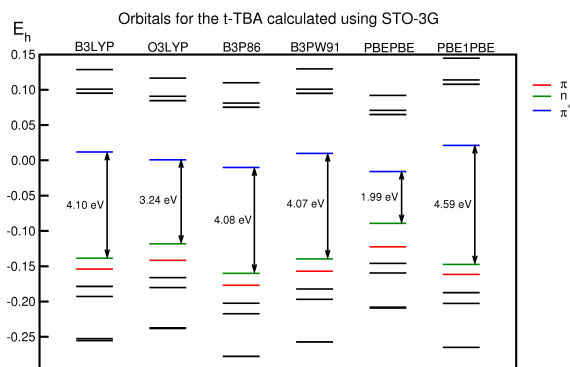


Figure A.1: Energy shift of molecular levels for the *trans*-TBA due to various DFT-functionals and STO-3G basis set.

calculated absorption spectra on a TD-DFT [42] level of theory. We note that the change of the molecular orbital order (HOMO and LUMO), as well as the energetic difference between the two, doesn't influence the qualitative appearance of the spectra. For every spectra calculation the molecules have been reoptimized with respect to the chosen DFT functional and basis set.

On figures A.1, A.2 and A.3 the molecular orbitals are presented for all studied functionals depending on basis sets (STO-3G, 6-31G*, and 6-311G*). We notice that the ordering of the HOMO and the HOMO-1 for *trans*-TBA, which are either n or π orbitals, depend on the chosen functional and basis set. If one is interested in HOMO-LUMO gaps only, which determine the reactivity and the valence excitation

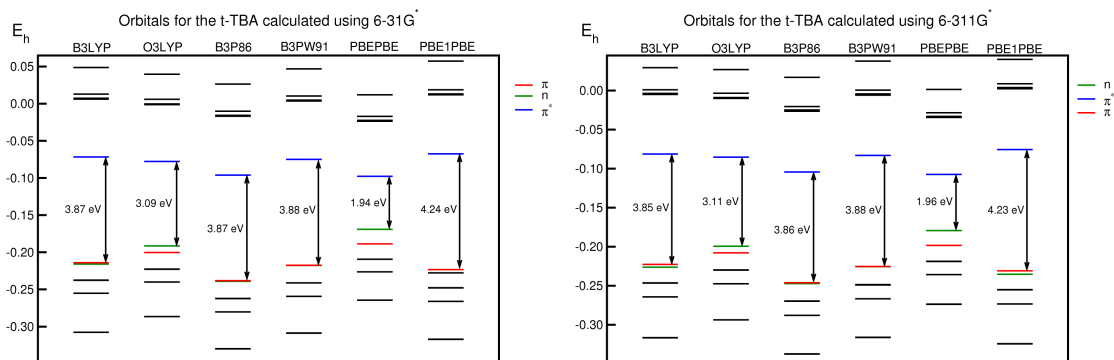


Figure A.2: Molecular orbital levels of the *trans*-TBA calculated with 6-31G*, on the left, and 6-311G* at the right hand side.

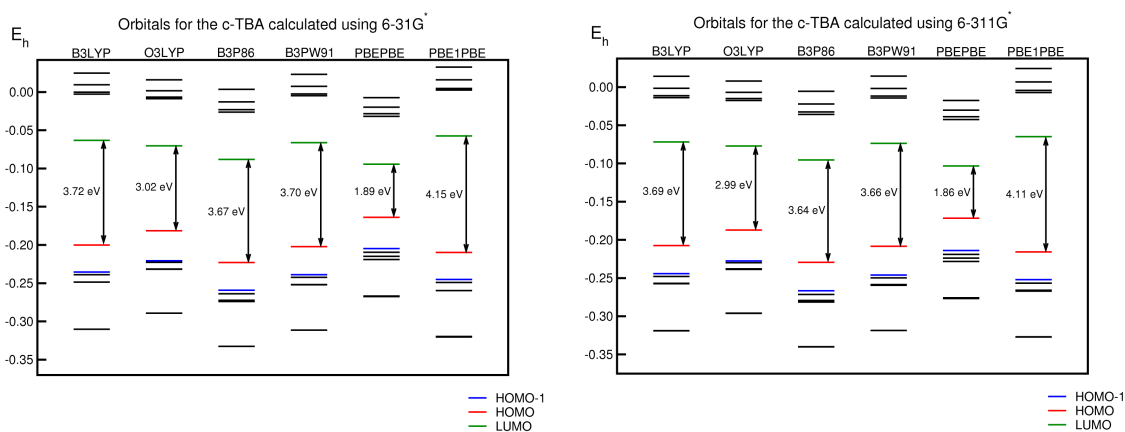


Figure A.3: Molecular orbital levels of the *cis*-TBA. Other details as given in Fig. A.2.

spectra, one can conclude that the application of the 6-31G* basis set seems to be quite sufficient, compared to the larger 6-311G* basis. The difference in energy gap is just 0.02 eV (for the B3LYP case). Both HOMO and HOMO-1 stabilize for the larger basis set, generating a slightly larger energy gap between the HOMO and the HOMO-1 for *trans*-TBA. Similar observations are made for *cis*-TBA, see Fig. A.3.

For DFT method testing, either the substitution of the exchange part took place (B3LYP vs. O3LYP) or the role of the correlation part was tested (B3P86 vs. B3PW91). Finally, non-hybrid vs. hybrid functionals were compared for PBEPBE vs. PBE1PBE (also known in literature as PBE0). However, PBE and PBE0 turned out to be completely inappropriate for estimating orbital energies. PBE

underestimates the gap significantly, while the PBE0 overestimates the gap. This causes larger absorption band shifts which are also to be seen in the O3LYP case. This conclusion is valid for both, *trans* and *cis* species of the TBA molecule. For completeness, the frontier orbitals of *trans*-TBA as obtained from B3LYP/6-31G* are shown in Table A.1.

The inappropriateness of the pure density functionals, in particular, also carries over to computed UV/Vis spectra, which are shown in Fig. A.4. In overall we can conclude that functionals including PBE are not appropriate for the systematical analysis of AB type molecules, reproducing the spectra in a substantially wrong way. For the O3LYP functional, a slight red shift of the $\pi \rightarrow \pi^*$ transition of the *trans* molecule is seen, which is even stronger for the PBE case, while PBE0, on the other hand, presumes slighter blue shift of the mentioned transition. B3P86 and B3PW91 are in the range of B3LYP. For the case of *cis*-TBA spectra similarities are obvious while using various functionals. Slight shifts occur and almost no influence in intensities for the $n \rightarrow \pi^*$ transition. Again, for the case of PBE/PBE, the $n \rightarrow \pi^*$ band is strongly red shifted, describing the spectra in a qualitatively wrong way.

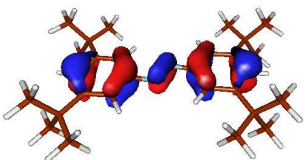
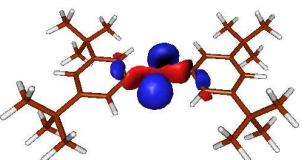
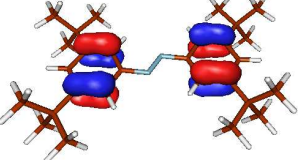
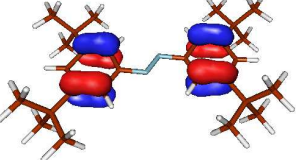
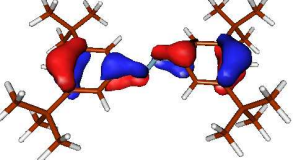
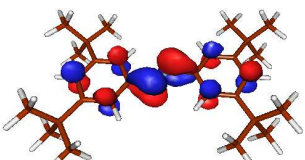
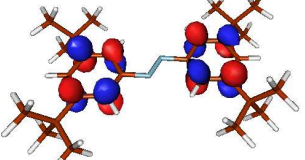
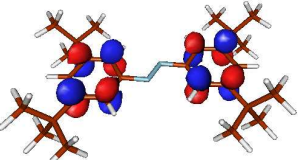
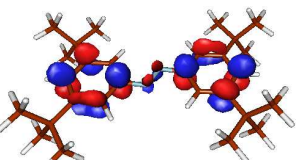
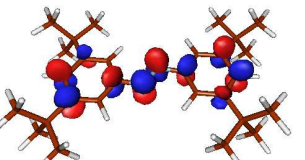
HOMO	HOMO-1	HOMO-2	HOMO-3	HOMO-4
 -5.8205 eV	 -5.8760 eV	 -6.4589 eV	 -6.4652 eV	 -6.9449 eV
LUMO	LUMO+1	LUMO+2	LUMO+3	LUMO+4
 -1.9521 eV	 0.1703 eV	 0.2019 eV	 0.3499 eV	 1.3279 eV

Table A.1: Frontier Kohn-Sham orbitals and orbital energies for the *trans*-TBA molecule calculated using B3LYP/6-31G*.

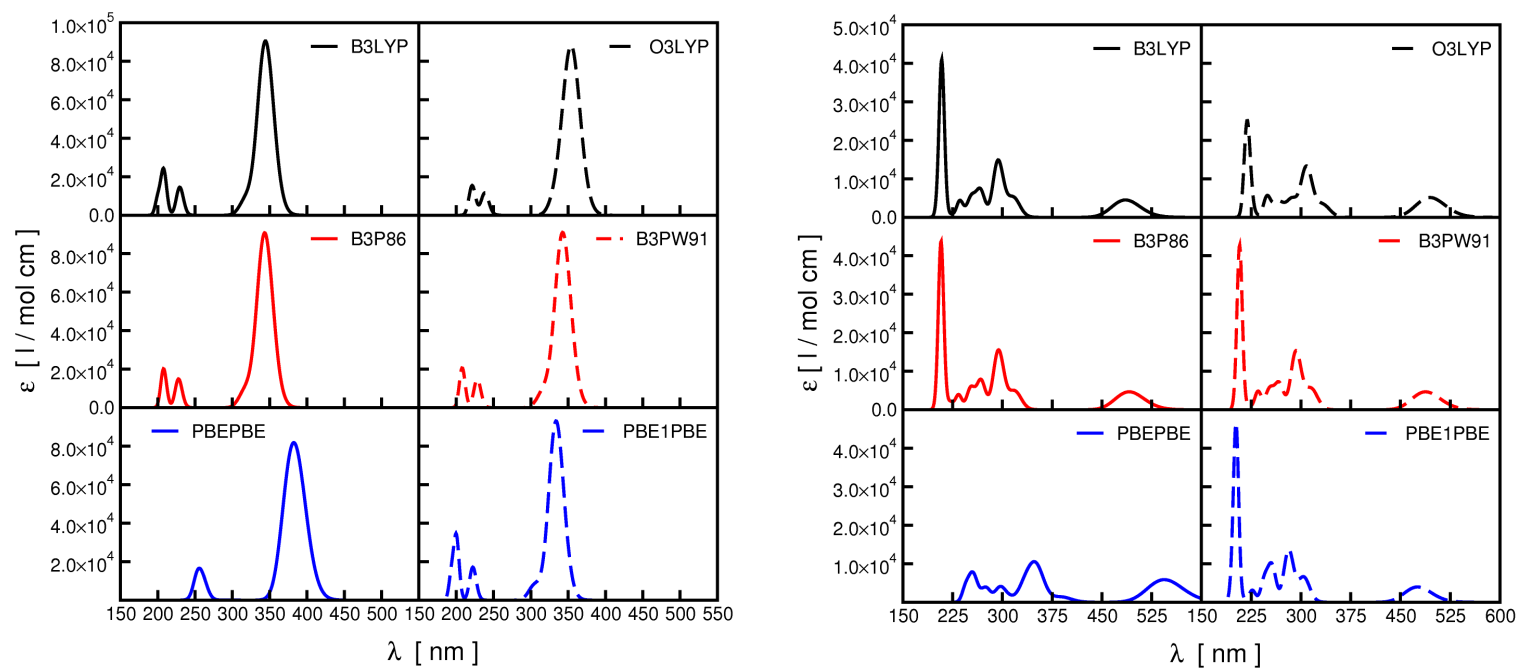


Figure A.4: Absorption spectra of the *trans*-TBA, on the left and *cis*-TBA, on the right hand side. These are calculated using linear response TD-DFT [42] employing different functionals and calculated with the 6-31G* basis set. For better comparison, spectra are plotted in the same axes range. As Gaussian broadening factor $\sigma = 900 \text{ cm}^{-1}$ has been chosen for all the spectra. In black, substitution of the exchange part has been done, in red change of the correlation part plays a role, while in blue, non-hybrid vs. hybrid functional is compared.

Appendix B

Transition Dipole Moments and Absorption Spectra

Basic considerations on the UV/Vis absorption spectra calculation will be explained in some more detail. The results on spectra calculations are given for non-substituted *cis*- and *trans*-azobenzene molecules in the gas phase. For all spectra TD-DFT was employed together with the B3LYP functional and the 6-31G* basis set. Other functionals have been tested as well, see Appendix A. Every absorption band is characterized by its position and oscillator strength.



Figure B.1: Orientation of the molecule in space and its symmetry determine values for individual components of the transition dipole moments in the given coordinate system. These are then used to calculate the transition dipole moment μ_{fi} for the absorption band (transition) of interest given with Eq.(B.1). Its total value is independent on the choice of the coordinate system. Here, the choice of coordinate system fits to symmetry operations of the C_{2h} and C_2 groups, for *trans*- and *cis*-AB, respectively.

The oscillator strength for a transition from state i to state f is connected to the total transition dipole moment μ_{fi} by:

$$f_{if} = \frac{2}{3} \frac{m_e \omega_{fi}}{\hbar e^2} |\mu_{fi}|^2 \quad (\text{B.1})$$

where f_{if} is the oscillator strength which is calculated here by TD-DFT, m_e the mass of an electron, $\omega_{fi} = (E_f - E_i)/\hbar$ is the angular frequency for the given transition, e is the electron charge and μ_{fi} is the value of the overall transition dipole moment, defined as

$$|\mu_{fi}|^2 = \sqrt{|\mu_x^2 + \mu_y^2 + \mu_z^2|}^2. \quad (\text{B.2})$$

State	μ_x (ea_0)	μ_y (ea_0)	μ_z (ea_0)	f_{if}	E (eV)	λ (nm)
<i>trans</i>						
1	0.0000	0.0000	0.0000	0.0000	2.5552	485
2	-2.3619	-1.6716	0.0000	0.7736	3.7713	329
3	0.0000	0.0000	0.0000	0.0000	4.1074	302
4	-0.2064	-0.7016	0.0000	0.0538	4.1087	302
5	0.0000	0.0000	0.0000	0.0000	4.8302	257
6	0.0000	0.0000	0.0000	0.0000	5.1247	242
7	0.0000	0.0000	0.0110	0.0000	5.1522	241
8	0.0000	0.0000	-0.0694	0.0006	5.3859	230
9	0.0000	0.0000	0.0000	0.0000	5.5231	224
10	0.2061	0.9599	0.0000	0.1305	5.5259	224
<i>cis</i>						
1	-0.2593	0.7305	0.0000	0.0379	2.5724	482
2	0.2799	-0.7777	0.0000	0.0689	4.1133	301
3	0.0000	0.0000	-0.2738	0.0077	4.2037	295
4	0.0721	-0.9356	0.0000	0.0945	4.3801	283
5	0.0000	0.0000	-0.1665	0.0030	4.4453	279
6	-0.3142	-0.7280	0.0000	0.0716	4.6477	267
7	0.0000	0.0000	0.4563	0.0250	4.9072	253
8	0.0000	0.0000	0.5836	0.0426	5.1039	243
9	0.0530	-0.6291	0.0000	0.0527	5.4018	230
10	0.1240	0.3360	0.0000	0.0180	5.7241	217

Table B.1: Results for the absorption spectra of the *cis*- and *trans*-AB obtained on the TD-B3LYP level of theory and the 6-31G* basis set. Beside the data for transition dipole moments, values for the oscillator strengths f_{if} , transition energies E and corresponding wavelengths λ are given for each transition, out of the ground state.

Transition dipole moments of the *cis*- and *trans*-AB are given in Table B.1. We note that the components of the total transition dipole moment μ_{fi} depend on the spatial

orientation of the molecule, *i.e.* the choice of the coordinate system. Here, we chose the coordinate system given in Fig. B.1. Of course, total transition dipole moment and oscillator strengths are independent of the choice of the coordinate system.

From Table B.1 it can be seen, for example, that the lowest allowed transition for *trans*-AB is at $\lambda = 329$ nm with an oscillator strength of 0.7736. This is the $\pi \rightarrow \pi^*$ transition. The $n \rightarrow \pi^*$ transition is at lower energy ($\lambda = 485$ nm) but is dipole-forbidden ($f_{if} = 0$). In contrast, all transitions for *cis*-AB are at least weakly allowed. The observed selection rules can be explained with the help of group theory. An allowed transition must fulfill the condition

$$\Gamma_i \otimes \begin{pmatrix} x \\ y \\ z \end{pmatrix} \otimes \Gamma_f \sim \Gamma_{symm}. \quad (\text{B.3})$$

Here, Γ_i and Γ_f are the irreducible representations of the initial and final states, and Γ_{symm} is the totally symmetric irreducible representation of the respective point group. The *trans*- and *cis*- AB, have C_{2h} and C_2 point groups, respectively. Corresponding character tables are shown in B.2. From Table B.2 (left),

C_{2h}	E	C_2	i	σ_h			C_2	E	C_2		
A_g	1	1	1	1	R_z	x^2, y^2, z^2, xy	A	1	1	z, R_z	x^2, y^2, z^2, xy
B_g	1	-1	1	-1	R_x, R_y	xz, yz	B	1	-1	x, y, R_x, R_y	xz, yz
A_u	1	1	-1	-1	z						
B_u	1	-1	-1	1	x, y						

Table B.2: On the left, character table for the C_{2h} group (*e.g.*, for *trans*-AB). On the right, character table for the C_2 group (*e.g.*, for *cis*-AB).

a $\pi \rightarrow \pi^*$ transition of *trans*-AB is allowed and (x, y) -polarized. Namely, a π -orbital has A_u symmetry in the C_{2h} point group, while π^* has B_g symmetry, thus $\Gamma_i \otimes \Gamma_f = A_u \otimes B_g = B_u \sim (x, y)$. In contrast, $n \rightarrow \pi^*$ transition is forbidden because $n \sim A_g$, hence $\Gamma_i \otimes \Gamma_f = A_g \otimes B_g = B_g$, which doesn't correspond to any component x, y, z . For *cis*-AB, the initial or final states are either A and B , thus their direct product is either A and B , resulting in allowed, z - or (x, y) -polarized transitions.

Appendix C

Thermal M-TBA Isomerization

Calculation of *cis*→*trans* isomerization rates, on a TBA derivative with an extra -OMe group in *para* position (M-TBA), will be demonstrated. This molecule can isomerize over two different paths, each over the corresponding TS, as shown in Fig. C.1.

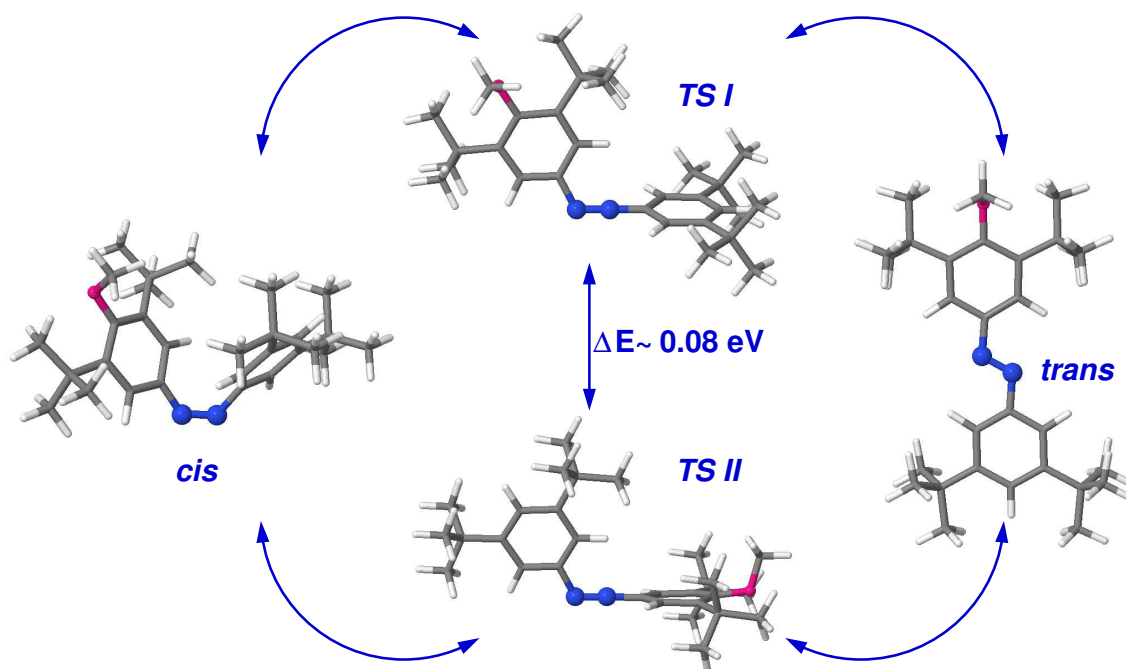


Figure C.1: Isomerization scheme for M-TBA: The reaction can proceed over two TSs with 0.08 eV energy difference between them (TS I is more stable in energy than TS II).

Classical activation energies (ΔE_{el}^\ddagger) and reaction energies (ΔE_{ct}), as well as the values for the permanent dipole moments of *cis*, *trans* and TS species are given in Table C.1.

path	ΔE_{el}^\ddagger [eV]	ΔE_{ct} [eV]	$ \mu_{tot}^{cis} $ [D]	$ \mu_{tot}^{TS} $ [D]	$ \mu_{tot}^{trans} $ [D]
I	1.09	0.66	3.97	3.42	1.05
II	1.17	0.65	3.97	4.11	1.05

Table C.1: Represented are electronic energy differences between the *cis*-M-TBA/or *trans*-M-TBA molecules and a TS I or TS II as well as total dipole moments for all the species.

Further, thermochemical data for two isomerization paths, over TS I and TS II, are given in Table C.3. At first, we calculated the data at the room temperature and then simply recalculated these values for all other temperatures (listed in Table C.3) with the help of Eq.(5.4), as explained in Chapter 5. The values from Table C.3, were used for Arrhenius plots $\ln k_{c \rightarrow t}$ vs. $1/T$. Linear fits give values of Arrhenius prefactors, A , and Arrhenius activation energies, E_a , as shown in Table C.2.

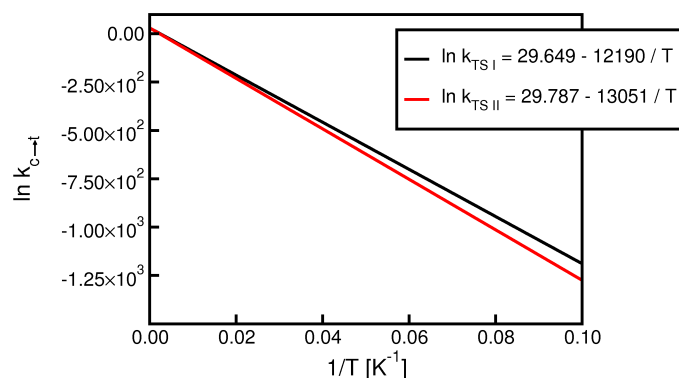


Figure C.2: Arrhenius plots $\ln k_{c \rightarrow t}$ vs. $1/T$ for M-TBA, over two isomerization paths with TS I (black) or TS II (red). The parameters given in the legend box are results for a linear fit of the set of points given in Table C.3.

path	$\ln A$	A [s^{-1}]	E_a [eV]	$\ln k$	$k_{(303.15K)}$ [s^{-1}]
I	29.649	7.52×10^{12}	1.05	-10.56	2.59×10^{-5}
II	29.787	8.64×10^{12}	1.12	-13.26	1.74×10^{-6}

Table C.2: Kinetic data from the linear fit presented in Fig. C.2. The activation energy E_a is calculated from the Arrhenius fit, thus reaction rates at 303.15 K slightly differ from those presented in Table C.3, which were calculated from the Eyring expression.

	$T(\text{K})$	$\frac{1}{T}(\text{K}^{-1})$	$\ln\left(\frac{k_B \cdot T}{h}\right)$	$\Delta S^\ddagger\left(\frac{\text{J}}{\text{mol} \cdot \text{K}}\right)$	$\Delta C_V^\ddagger\left(\frac{\text{J}}{\text{mol} \cdot \text{K}}\right)$	$\Delta H(0)^\ddagger\left(\frac{\text{J}}{\text{mol}}\right)$	$\Delta G^\ddagger\left(\frac{\text{J}}{\text{mol}}\right)$	$\frac{\Delta G^\ddagger}{RT}$	$\ln k$	$k(\text{s}^{-1})$
TS I	10	0.1000	26.0621	0.8415	-1.2100	101021.35	101000.84	1214.83	-1188.77	0
	30	0.0333	27.1607	0.8415	-1.2100	101021.35	100959.81	404.78	-377.62	$1.00 \cdot 10^{-164}$
	50	0.0200	27.6715	0.8415	-1.2100	101021.35	100918.78	242.77	-215.10	$3.83 \cdot 10^{-94}$
	100	0.0100	28.3647	0.8415	-1.2100	101021.35	100816.20	121.26	-92.90	$4.51 \cdot 10^{-41}$
	150	0.0067	28.7702	0.8415	-1.2100	101021.35	100713.63	80.76	-51.99	$2.64 \cdot 10^{-23}$
	200	0.0050	29.0578	0.8415	-1.2100	101021.35	100611.05	60.51	-31.45	$2.20 \cdot 10^{-14}$
	250	0.0040	29.2810	0.8415	-1.2100	101021.35	100508.48	48.36	-19.08	$5.17 \cdot 10^{-9}$
	298.15	0.0034	29.4571	0.8415	-1.2100	101021.35	100409.70	40.51	-11.05	$1.59 \cdot 10^{-5}$
	303.15	0.0033	29.4737	0.8415	-1.2100	101021.35	100399.44	49.83	-10.36	$3.18 \cdot 10^{-5}$
	313	0.0032	29.5057	0.8415	-1.2100	101021.35	100379.23	38.57	-9.07	$1.15 \cdot 10^{-4}$
	333	0.0030	29.5677	0.8415	-1.2100	101021.35	100338.20	36.24	-6.67	$1.27 \cdot 10^{-3}$
	350	0.0029	29.6175	0.8415	-1.2100	101021.35	100303.33	34.47	-4.85	$7.83 \cdot 10^{-3}$
TS II	10	0.1000	26.0621	1.4151	-1.6956	108173.21	108142.10	1300.72	-1274.66	0
	30	0.0333	27.1607	1.4151	-1.6956	108173.21	108079.89	433.32	-406.16	$4.04 \cdot 10^{-177}$
	50	0.0200	27.6715	1.4151	-1.6956	108173.21	108017.68	259.85	-232.17	$1.48 \cdot 10^{-101}$
	100	0.0100	28.3647	1.4151	-1.6956	108173.21	107862.14	129.74	-101.37	$9.45 \cdot 10^{-45}$
	150	0.0067	28.7702	1.4151	-1.6956	108173.21	107706.61	86.37	-57.60	$9.65 \cdot 10^{-26}$
	200	0.0050	29.0578	1.4151	-1.6956	108173.21	107551.07	64.68	-35.62	$3.39 \cdot 10^{-16}$
	250	0.0040	29.2810	1.4151	-1.6956	108173.21	107395.54	51.67	-22.39	$1.89 \cdot 10^{-10}$
	298.15	0.0034	29.4571	1.4151	-1.6956	108173.21	107245.75	43.26	-13.81	$1.01 \cdot 10^{-6}$
	303.15	0.0033	29.4737	1.4151	-1.6956	108173.21	107230.20	42.55	-13.07	$2.11 \cdot 10^{-6}$
	313	0.0032	29.5057	1.4151	-1.6956	108173.21	107199.56	41.19	-11.69	$8.38 \cdot 10^{-6}$
	333	0.0030	29.5677	1.4151	-1.6956	108173.21	107137.35	38.70	-9.13	$1.08 \cdot 10^{-4}$
	350	0.0029	29.6175	1.4151	-1.6956	108173.21	107084.47	36.80	-7.18	$7.62 \cdot 10^{-4}$

Table C.3: In the upper part, thermochemical and kinetic isomerization data are given for the isomerization of M-TBA over TS I. In the lower section, the same is shown for the thermal isomerization over TS II.

Appendix D

COD Geometries

We are introducing structural parameters of the free COD molecule (see Section 6.2.1), and COD adsorbed on Si(001) clusters in *bridge* and *upright* structures (see Section 6.2.2). As an example, *bridge* adsorbed COD enantiomers are shown in Fig. D.1, where we see that during the switching process the adsorbed molecule interconverts from one to the other form. The given numbering of C atoms is consistent with the free COD and the adsorbed molecules. Data for bond lengths, angles and dihedral angles are listed, for corresponding molecules, in Table D.1.

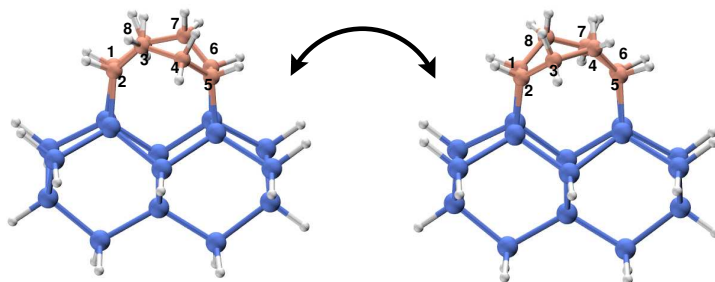


Figure D.1: Numbering of atoms for the *bridge* adsorbed COD molecule on a H-saturated Si₁₅ cluster. The same numbering holds for two distinct *upright* (Table D.2) adsorbed molecules, form a) and b) in Table D.1. For the *bridge* structure, geometry orientation of both minima and a TS is given as well in Table D.1.

	COD		COD@Si(001)		<i>bridge</i> COD@Si(001)		
	min	TS	Form a	Form b	min ₁ @Si	min ₂ @Si	TS@Si
r_{12}	1.34	1.34	1.34	1.34	1.60	1.60	1.60
r_{23}	1.51	1.51	1.51	1.51	1.54	1.57	1.54
r_{34}	1.54	1.58	1.56	1.56	1.55	1.55	1.56
r_{45}	1.51	1.51	1.54	1.54	1.57	1.54	1.55
r_{56}	1.34	1.34	1.58	1.60	1.60	1.60	1.60
r_{67}	1.51	1.51	1.54	1.54	1.54	1.57	1.55
r_{78}	1.54	1.58	1.54	1.54	1.55	1.55	1.56
r_{81}	1.51	1.51	1.51	1.51	1.57	1.54	1.54
\angle_{812}	130.8	124.6	129.9	127.8	122.9	118.7	117.2
\angle_{123}	129.2	124.6	126.7	125.3	118.7	122.9	117.2
\angle_{234}	114.0	116.1	115.1	115.4	122.7	125.1	126.0
\angle_{345}	118.2	116.0	117.1	119.0	125.1	122.7	126.9
\angle_{456}	130.8	124.4	117.8	120.6	122.9	118.7	124.8
\angle_{567}	129.2	124.4	120.1	119.1	118.7	122.9	124.8
\angle_{678}	114.0	116.0	115.3	108.8	122.7	125.1	126.9
\angle_{781}	118.2	116.1	120.1	118.6	125.1	122.7	126.0
d_{1234}	-81.8	-69.9	-81.3	-86.2	-92.1	-23.8	-78.1
d_{2345}	61.8	-0.5	35.7	32.9	51.7	-51.8	25.4
d_{3456}	13.8	70.7	60.8	54.1	23.9	92.2	45.2
d_{4567}	-0.4	0.0	-38.4	-20.1	10.5	-10.5	0.1
d_{5678}	-81.8	-70.7	-66.4	-75.9	-92.1	-23.8	-45.6
d_{6781}	61.8	0.5	60.3	46.5	51.7	-51.8	-24.9
d_{7812}	13.8	69.9	22.2	37.4	23.9	92.2	77.8
d_{8123}	-0.4	0.0	-0.9	-0.1	10.5	-10.5	0.0

Table D.1: Data for bond lengths (given in Å), angles and dihedral angles (in degrees) for the free COD molecule, and *upright* and *bridge* adsorbed molecules. The indices are used corresponding to the numbering in Fig. D.1. The first two columns describe geometrical parameters of the non-adsorbed gas phase COD of both minima and a TS, respectively. The following two columns describe *upright* a) and b) forms in agreement with the notation shown on page 100, and the last three refer to geometries of *bridge*-like adsorbed molecules, as before, for both minima and TS, respectively.

Using cluster models has its limitations which is the best to see for orientations of the *upright* COD molecule at Si(001). Namely, the two a) and b) forms are calculated with respect to relative orientations of the whole COD molecule and the non-saturated dimer (left panel of Table D.2). We found that a) is the most stable form at the cluster, which is also found by Cho and co-workers [123] using periodic DFT calculations. Energies for all other geometries are calculated relative to the energy of a). *Upright* structures were calculated for the case where the free dimer was also saturated (right panel of Table D.2). Now, orientation c) is the most stable one, and energies c'), d), and d') are calculated relative to it.

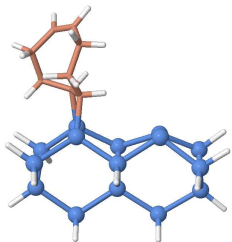
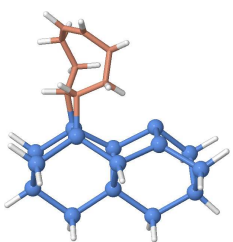
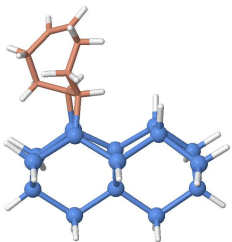
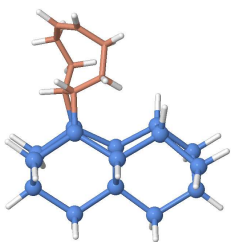
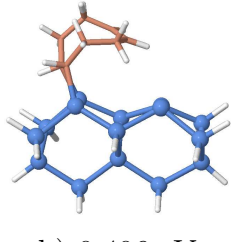
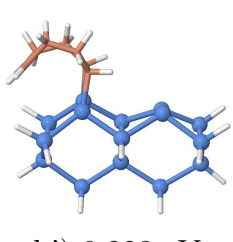
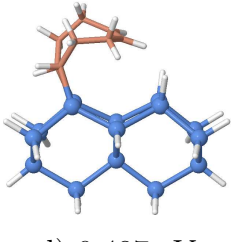
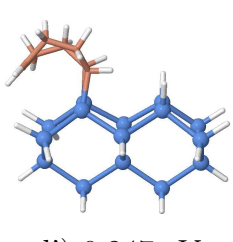
Optimized COD on Single Si Dimers			
non-saturated dimer		saturated dimer	
 a) 0.0 eV	 a') 0.029 eV	 c) 0.0 eV	 c') 0.062 eV
 b) 0.406 eV	 b') 0.223 eV	 d) 0.487 eV	 d') 0.247 eV

Table D.2: Geometries and relative energies of fully optimized *upright* structures. Structure a) is similar to the one of Cho *et al.* [123] and indeed the most stable one. On the left side the dangling bonds of the Si-dimer are free while these are saturated for clusters presented on the right hand side of the table. Due to saturation the whole system is stabilized which is the reason for larger ΔE compared to non-saturated ones. Here it is also demonstrated that cluster models show their limitations, causing energy differences for structures which would be equivalent in the periodic case, due to relative position of the molecule on the cluster.

Appendix E

Normal Mode Analysis for COD@Si(001)

After the symmetrization of the two-dimensional PES $V(\phi_p, \phi_n)$ (which is calculated for COD@Si(001) and presented in Section 6.2.3), it is necessary to perform normal mode analysis for the stationary points, *i.e.*, minima, 2nd order TS and TSs of the surface, and compare these to values provided with quantum chemical calculations. Since the switching of the COD can be imagined as the movement of two masses m_0 and m_1 , the Hessian matrix is then

$$\mathbf{H} = \begin{pmatrix} \frac{k_{11}}{m_0} & \frac{k_{12}}{\sqrt{m_0 m_1}} \\ \frac{k_{21}}{\sqrt{m_0 m_1}} & \frac{k_{22}}{m_1} \end{pmatrix}. \quad (\text{E.1})$$

One can extract the eigenvalues solving the following polynomial (taking into account the fact that $k_{12} = k_{21}$):

$$\begin{vmatrix} \frac{k_{11}}{m_0} - \Lambda & \frac{k_{12}}{\sqrt{m_0 m_1}} \\ \frac{k_{21}}{\sqrt{m_0 m_1}} & \frac{k_{22}}{m_1} - \Lambda \end{vmatrix} = \left(\frac{k_{11}}{m_0} - \Lambda \right) \left(\frac{k_{22}}{m_1} - \Lambda \right) - \frac{k_{12}^2}{m_0 m_1} = 0. \quad (\text{E.2})$$

After solving the quadratic equation we are getting eigenvalues Λ_1 and Λ_2 . Angular frequencies are then obtained as square roots of these eigenvalues, *i.e.*, $\omega_1 = \sqrt{\Lambda_1}$ and $\omega_2 = \sqrt{\Lambda_2}$. We must also note that for our calculations instead of the reduced mass we used data for the moment of inertia, introduced before, see Section 6.3.1.

If one defines force constants, k , as second order derivatives, they can be calculated with central differences as [58]:

$$k_{xx} = \frac{\partial^2 V}{\partial x^2} = \frac{V(x + 2\Delta x, y) - 2V(x, y) + V(x - 2\Delta x, y)}{4\Delta x^2} \quad (\text{E.3})$$

and

$$k_{yy} = \frac{\partial^2 V}{\partial y^2} = \frac{V(x, y + 2\Delta y) - 2V(x, y) + V(x, y - 2\Delta y)}{4\Delta y^2}. \quad (\text{E.4})$$

Mixed terms are calculated as

$$\begin{aligned} k_{xy} &= \frac{\partial^2 V}{\partial x \partial y} = k_{yx} = \frac{\partial^2 V}{\partial y \partial x} \\ &= \frac{V(x + \Delta x, y + \Delta y) - V(x + \Delta x, y - \Delta y) - (x - \Delta x, y + \Delta y) + V(x - \Delta x, y - \Delta y)}{4\Delta x \Delta y}. \end{aligned} \quad (\text{E.5})$$

$V(x, y)$ is the stationary point of interest on the PES, *i.e.*, minimum, 2nd order TS or TS.

Appendix F

Hamiltonian Derivation for COD@Si(001)

Here we derive the Hamiltonian which is given in Section 6.3.1, for COD@Si(001). One is starting from the Lagrangian, depending on angles¹:

$$L(\phi_1, \phi_2, \dot{\phi}_1, \dot{\phi}_2) = T - V = \frac{1}{2}I\dot{\phi}_1^2 + \frac{1}{2}I\dot{\phi}_2^2 - V(\phi_1, \phi_2). \quad (\text{F.1})$$

Applying generalized coordinates defined in Eqs. (6.1) and (6.2)

$$\phi_1 = \phi_p + \frac{1}{2}\phi_n, \quad \phi_2 = \phi_p - \frac{1}{2}\phi_n \quad (\text{F.2})$$

we get the following expression:

$$L(\phi_p, \phi_n, \dot{\phi}_p, \dot{\phi}_n) = \frac{1}{2}I\left(\dot{\phi}_p + \frac{\dot{\phi}_n}{2}\right)^2 + \frac{1}{2}I\left(\dot{\phi}_p - \frac{\dot{\phi}_n}{2}\right)^2 - V(\phi_p, \phi_n) \quad (\text{F.3})$$

i.e., the Lagrangian depends on the generalized coordinates only:

$$L(\phi_p, \phi_n, \dot{\phi}_p, \dot{\phi}_n) = I\dot{\phi}_p^2 + \frac{1}{4}I\dot{\phi}_n^2 - V(\phi_p, \phi_n). \quad (\text{F.4})$$

This leads to the classical Hamilton function²:

$$H(\phi_p, \phi_n, l_p, l_n) = \frac{l_p^2}{2I_p} + \frac{l_n^2}{2I_n} - L = T + V(\phi_p, \phi_n) \quad (\text{F.5})$$

¹Generally, for a system of n particles, $L(\vec{r}_1, \dots, \vec{r}_N, \dot{\vec{r}}_1, \dots, \dot{\vec{r}}_N) = T - V = \frac{1}{2} \sum_{i=1}^N m_i \dot{\vec{r}}_i^2 -$

$V(\vec{r}_1, \dots, \vec{r}_N)$
² $H = \sum_{i=1}^N \frac{\vec{p}_i^2}{2m_i} - L$

Angular momenta are calculated as

$$l_p = \frac{\partial L}{\partial \dot{\phi}_p} = 2I\dot{\phi}_p, \quad l_n = \frac{\partial L}{\partial \dot{\phi}_n} = \frac{1}{2}I\dot{\phi}_n. \quad (\text{F.6})$$

By analogy between Eq.(F.1) and (F.5), we get the following relations: $I_p = 2I$ and $I_n = 0.5 \cdot I$. If one uses the quantum operators for angular momenta

$$\hat{l}_p = \frac{\hbar}{i} \frac{d}{d\phi_p}, \quad \hat{l}_n = \frac{\hbar}{i} \frac{d}{d\phi_n} \quad (\text{F.7})$$

we are finally getting the expression for Hamilton operator in 2D:

$$\hat{H} = -\frac{\hbar^2}{2I_p} \frac{\partial^2}{\partial \phi_p^2} - \frac{\hbar^2}{2I_n} \frac{\partial^2}{\partial \phi_n^2} + V(\phi_p, \phi_n). \quad (\text{F.8})$$

Accordingly, reducing the problem to 1D, the Hamilton operator is:

$$\hat{H} = -\frac{\hbar^2}{2I_p} \frac{d^2}{d\phi_p^2} + V(\phi_p; \phi_n = 0). \quad (\text{F.9})$$

Appendix G

Fourier Grid Hamiltonian

The time-independent Schrödinger equation for nuclear motion is given as:

$$\hat{H}|\phi_v\rangle = (\hat{T} + \hat{V})|\phi_v\rangle = E_v|\phi_v\rangle. \quad (\text{G.1})$$

In order to solve it, one can apply a numerical method called *Fourier Grid Hamiltonian* (FGH) [135] in order to get eigenfunctions $|\phi_v\rangle$ and eigenenergies E_v . The method starts from the fact that the kinetic energy operator \hat{T} is diagonal in momentum space and the potential energy operator \hat{V} is diagonal in position space. Fourier transformation is used to convert from the position to momentum space and vice versa³. In Ref. [135] this problem was illustrated motion of a single particle with mass m in one-dimension (x):

$$\hat{H} = \hat{T} + \hat{V}(\hat{x}) = \frac{\hat{p}^2}{2m} + \hat{V}(\hat{x}). \quad (\text{G.2})$$

The basis vectors $|x\rangle$ are eigenfunctions of the position operator \hat{x} :

$$\hat{x}|x\rangle = x|x\rangle. \quad (\text{G.3})$$

The eigenvectors form an orthonormal basis, *i.e.*:

$$\langle x|x'\rangle = \delta(x - x') \quad , \quad \hat{I}_x = \int_{-\infty}^{\infty} dx|x\rangle\langle x|. \quad (\text{G.4})$$

As mentioned, the potential is diagonal in position space:

$$\langle x|V(\hat{x})|x\rangle = V(x)\delta(x - x'). \quad (\text{G.5})$$

³Fourier transformation: $Y(\omega) = \frac{1}{\sqrt{2\pi}} \int y(t)e^{-i\omega t} dt$ and inverse Fourier transformation: $y(t) = \frac{1}{\sqrt{2\pi}} \int Y(\omega)e^{i\omega t} d\omega$

In momentum space the basis vectors are eigenvectors of the momentum operator \hat{p} :

$$\hat{p}|k\rangle = k\hbar|k\rangle. \quad (\text{G.6})$$

Hence, the kinetic energy operator \hat{T} is diagonal in momentum space:

$$\langle k'|\hat{T}|k\rangle = T_k\delta(k-k') = \frac{\hbar^2 k^2}{2m}\delta(k-k'). \quad (\text{G.7})$$

These vectors form an orthogonal basis, analogous to Eq.(G.4). The basis vectors of position and momentum space are related by:

$$\langle k|x\rangle = \frac{1}{\sqrt{2\pi}}e^{-ikx}. \quad (\text{G.8})$$

Taking all these conditions into account, we can write an expression for a matrix element of the Hamilton operator:

$$\begin{aligned} \langle x|\hat{H}|x'\rangle &= \langle x|\hat{T}|x'\rangle + V(x)\delta(x-x') \\ &= \langle x|\left\{\int_{-\infty}^{\infty}|k'\rangle\langle k'|dk'\right\}\hat{T}\left\{\int_{-\infty}^{\infty}|k\rangle\langle k|dk\right\}|x'\rangle + V(x)\delta(x-x') \\ &= \int_{-\infty}^{\infty}\langle x|k\rangle T_k\langle k|x'\rangle dk + V(x)\delta(x-x') \\ &= \frac{1}{2\pi}\int_{-\infty}^{\infty}e^{ik(x-x')}T_k dk + V(x)\delta(x-x'). \end{aligned} \quad (\text{G.9})$$

The following step is to replace the continuous function x with a set of discrete grid points x_i . For a grid with N points we use an equidistant spacing interval Δx :

$$x_i = i\Delta \quad , \quad i = 1, \dots, N. \quad (\text{G.10})$$

The eigenvectors of the discrete basis satisfy:

$$\Delta x\langle x_i|x_j\rangle = \delta_{ij} \quad , \quad \hat{I}_x = \sum_{i=1}^N|x_i\rangle\Delta x\langle x_i|. \quad (\text{G.11})$$

Now, using the discrete basis in position space, matrix elements $\langle x_i|\hat{H}|x_j\rangle$ are given by:

$$H_{ij} = \frac{1}{\Delta x}\left\{\sum_{l=-N/2}^{N/2}\frac{e^{il2\pi(i-j)/N}}{N}\cdot T_l + V(x_i)\delta_{ij}\right\} \quad (\text{G.12})$$

with

$$T_l = \frac{\hbar^2}{2m}\cdot(l\Delta k)^2 \quad , \quad \Delta k = \frac{2\pi}{N\Delta x}. \quad (\text{G.13})$$

Diagonalization of the complete Hermitian matrix H_{ij} delivers eigenfunctions and eigenvectors of the Hamilton operator, *i.e.*, $|\phi_v\rangle$ and E_v as in Eq.(G.1).

Acknowledgment

At first, I want to thank my supervisor Prof. Dr. Peter Saalfrank for giving me the opportunity to work on such an interesting topic in his group. I would also like to thank him for his friendly, responsible and kind personality, for supporting me and this work.

Further, I want to thank PD Dr. Tillmann Klamroth for guiding me during the whole time with his competence and very friendly appearance. I learned a lot from you. Prof. Dr. Mathias Nest I would like to thank as well because he has always been very friendly and correct to me.

Jean-Christophe Tremblay gets the special gratitude for being brave in reading the very first version of this thesis. Besides, you are a super colleague and it is a pleasure to know you and share the office with you. Sergio López López and Karl Zenichowski get the thanks too, for being wonderful co-workers.

I also thank my former student Marcel Gothe who made his diploma thesis in the group.

I want to thank Kerstin Faustmann, Thomas Ritschel and Galina Jurchenko for their readiness to help me at any time. Jan Götze I thank you for your very open and friendly nature, and Dr. Vetter and Dr. Zuhrt for helping me with my first calculations. Dominik Kröner, Pascal Krause and Ivan Andrianov get the gratitude for helping me during my first steps in the group.

Also, I want to thank the whole group for pleasant and friendly working atmosphere. I had really a great time here.

Finally, I want to thank my parents, the rest of the family and Gernot, for being with me and loving me also in the most stressful situations.

Erklärung

Hiermit versichere ich, dass ich die vorliegende Arbeit mit den angegebenen Hilfsmitteln selbständig angefertigt habe.

Potsdam, im November 2009